UNIVERSITY OF SÃO PAULO
INSTITUTO DE FÍSICA DE SÃO CARLOS

Charlie Oscar Oncebay Segura

Diamond studies for applications in quantum technologies

São Carlos

2019

Charlie Oscar Oncebay Segura

Diamond studies for applications in quantum technologies

Thesis presented to the Graduate Program in Physics at the Instituto de Física de São Carlos, Universidade de São Paulo, to obtain the degree of Doctor in Science.

Concentration area: Applied Physics

Advisor: Prof. Dr. Sérgio Ricardo Muniz

Corrected version

(Original version available on the Program Unit)

São Carlos

2019

Oncebay Segura, Charlie Oscar
Diamond studies for applications in quantum technologies / Charlie Oscar Oncebay Segura; advisor Sérgio Ricardo Muniz - revised version -- São Carlos 2019.
115 p.

Thesis (Doctorate - Graduate Program in Física Aplicada) -- Instituto de Física de São Carlos, Universidade de São Paulo - Brasil , 2019.

1. Magnetometry. 2. Nitrogen-Vacancy in diamond. 3. ODMR. I. Ricardo Muniz, Sérgio , advisor. II. Title.

To my grandparents Aniceto and Clara, and to loving memory of my grandparents Marcelino and Teresa this humble work is a sign of my love to you.

ACKNOWLEDGEMENTS

The realization of this thesis was only possible due to the collaboration of several people, to which I desire to express my gratitude.

First, I would like thank my advisor Prof. Dr. Sérgio Muniz, for his support from day one to this project and my scientific career. His encouragement always gave me the confidence and energy to finish this project. He also allowed me a lot of flexibility and freedom so that I can become an independent researcher. I am thankful for his kindness, patience, friendship, and support throughout these years.

I wish to thank Prof. Dr. Francisco Guimarães for the help with analysis the photoluminescence of the NV center and sharing his knowledge on using the confocal microscope. The discussions were of extreme relevance.

My gratitude to the Photonics Group, especially Prof. Dr. Cleber Renato Mendoça and Dr. Juliana Mara Pinto de Almeida, for the valuable discussion about nonlinear optics.

Thanks to Prof. Dr. Eduardo de Azevedo and Prof. Dr. Claudio José Magon by helping me with my questions about the Electron Paramagnetic Resonance. I highly appreciate the help and collaboration of Prof. Dr. Rene Nome Silva (UNICAMP), B.Eng. Haroldo Arakaki, B.Eng. João Marcelo, Prof. Dr. Sebastião Pratavieira, and Prof. Dr. Luiz Antonio.

I really appreciate the opportunity of working in the University of New Mexico, through the partnership with Prof. Dr. Victor Acosta, by which I could expand my knowledge on diamond defects. Thank you to whole Acosta's group for the help and hospitality. In particular, I thank Yaser Silani and Forrest Hubert for the friendship.

My sincere thanks to my friends for valuable discussions and for sharing experiences: Thalyta Martins, Dennys Mallqui, Itala Laurente, Edson Garambel, Nataly Ayre, Carlos Gamarra, Mikeas Lima. In particular, I would like to thank Jaqueline Palmieri and Emerson Santos (Pele) for their friendship and help, I am eternally grateful. For sure, the great time I had in Albuquerque was because sure my friends Carlos Carrion Bonilla and Maria Del Carmen Barragan was kind enough to show me the city and to make sure that I felt comfortable away from home.

A special thanks to my parents Oscar and Zully for all the love and support that you have given me. To my lovely wife, Fiorella and my daughter Lia Valentina thank you for always being there and for giving me the best reason to leave the lab and come home.

Finally, I am grateful to Coordination for Improvement of Higher Education Personnel (CAPES) for financial support.

"The only way to do great work
is to love what you do."
Steve Jobs

ABSTRACT

ONCEBAY SEGURA, C. **Diamond studies for applications in quantum technologies**. 2019. 115p. Thesis (Doctor in Science) - Instituto de Física de São Carlos, Universidade de São Paulo, São Carlos, 2019.

Among several hundred impurities and defects that can occur in diamond, the nitrogen-vacancy (NV) center is one of the most interesting for quantum technologies at room temperature. Several properties make it an excellent platform for many applications, from nanosensor to quantum information processing.

This thesis presents the first explorations of NV-based technologies in our laboratory, investigating three sets of studies aimed at learning the know-how of this field of research and developing the necessary infrastructure to explore them in future quantum technologies. The first set of studies focus on magnetometry and how to improve NV-based magnetic sensing. We show that, using engineered ensembles of NV centers in ultrapure synthetic diamonds, one can build a relatively simple apparatus to do magnetic imaging of relatively large areas while determining the full vector field with high spatial resolution and very good sensitivity. We also show that these measurements can be used to reconstruct the current density distribution of nearby sources, opening exciting possibilities to study two-dimensional materials.

Another set of studies involve spin coherence of an ensemble of NV centers. For that, we developed a method based on a CCD camera and an imaging protocol that allows implementing pulse sequences like Rabi, Ramsey and Hahn echo, performing Electron Spin Resonance (ESR) spectroscopy over extended areas. Using this method we extract parameters from our sample, including measurements for T_1, T_2 and T_2^*. The method was also used to observe Electron Spin Echo Envelope Modulation (ESEEM), due to hyperfine interaction with nearby ^{15}N nucleus, resulting in improved frequency sensitivity.

The third set of studies explore how to use femtosecond lasers to produce NV centers in diamond and investigated the nonlinear index of refraction (n_2) of the diamond (type IIa) in a broad spectral region, from the infrared (1500 nm) to the ultraviolet (260 nm).

Keywords: Magnetometry, Nitrogen-Vacancy in diamond, ODMR.

RESUMO

ONCEBAY SEGURA, C. **Estudos no diamante para aplicações em Tecnologias Quânticas**.2019. 115p. Thesis (Doctor in Science) - Instituto de Física de São Carlos, Universidade de São Paulo, São Carlos, 2019.

Entre várias centenas de impurezas e defeitos que podem ocorrer no diamante, o centro Nitrogênio-Vacância (NV) é um dos mais interessantes para tecnologias quânticas em temperatura ambiente. Diversas propriedades fazem dele uma excelente plataforma para muitas aplicações, desde nanosensores até o processamento de informações quânticas.

Esta tese apresenta a primeira exploração de tecnologias baseadas em NV no nosso laboratório, investigando três conjuntos de estudos com objetivo de aprender o *know-how* desta área de pesquisa e desenvolver a infra-estrutura necessária para explorá-los em futuras tecnologias quânticas. O primeiro conjunto de estudos enfoca a magnetometria e como melhorar o sensores magnético baseado em centros NV. Mostramos que um aparato relativamente simples pode ser usado para produzir imagens magnéticas do campo vetorial, usando *ensembles* de centros NV em diamantes sintéticos ultrapuros. Também mostramos que essas medidas podem ser usadas para reconstruir a distribuição de densidade de corrente de fontes próximas, abrindo possibilidades interessantes para o estudo de materiais bidimensionais.

Outro conjunto de estudos envolve a coerência de spin de um *ensemble* de centros NV. Para isso, desenvolvemos um método baseado em uma câmera CCD e um protocolo de imagem que permite implementar sequências de pulsos como Rabi, Ramsey e eco Hahn, realizando espectroscopia de ressonância de spin eletrônico (ESR) sobre áreas estendidas. Usando esse método, extraímos parâmetros de nossa amostra, incluindo medidas para T_1, T_2 e T_2^*. O método também foi usado para observar o efeito ESEEM (Envelope de Modulação de Eco de Spin Eletrônico), devido à interação hiperfina com o núcleo próximo de ^{15}N, resultando numa melhor sensibilidade de freqüência.

Finalmente, o terceiro conjunto de estudos explorou como usar lasers de femtossegundos para produzir centros NV em diamante e investigou o índice de refração não-linear (n_2) do diamante (tipo IIa) em uma ampla região espectral, desde o infravermelho (1500 nm) até o ultravioleta (260 nm).

Palavras-chave: Magnetometria. Centro Nitrogênio-Vacância. ODMR.

LIST OF FIGURES

Figure 1 – Diamond type classification. 27

Figure 2 – a) In single-crystal type Ib diamond this environment is dominated by substitutional nitrogen defects (P1 centers). b) NV center atomic structure in diamond. We changed the color the carbon atoms to distinguish the nv center. 28

Figure 3 – Diamond unit cell with NV defect. The NV center possesses the C_{3v} symmetry and has a major symmetry axis that is defined by the direction joining the nitrogen and vacancy (quantization axis). 29

Figure 4 – Left: Energy level diagram showing the known optical transitions. The triplet ground state ^3A is split in a $m_s = 0$ and $m_s = \pm 1$ sublevel by 2.87 GHz. Right: The NV center is excited with green laser (532 nm) and decays emitting fluorescence with a ZPL at 637 nm. 30

Figure 5 – The energy level scheme of the NV centre including zero-field splitting, electron Zeeman interaction and hyperfine interaction with the nitrogen nuclear spin of ^{14}N or ^{15}N. 34

Figure 6 – a) Schematic representation of the shift of the ODMR resonance lines as a function of the applied magnetic field along the NV axis. b) NV defect structure at applied magnetic field B_z. c) ODMR spectra in a field $B_z = 0$, show two dips associated with the lattice strain. d) ODMR spectra in field $B_z \neq 0$, the two dips correspond to transitions $m_s = 0 \leftrightarrow m_s = \pm 1$ of an NV. 35

Figure 7 – ODMR frequencies f_n, for the spin states $m_s = \pm 1$, as a function of the magnetic field $\vec{B}$ is applied with an angle θ with respect to the NV axis. The lines are obtained the equation 2.22, using $D_1 = 2.87$ GHz, $g_e\beta = 28.8$ GHz/T and $E_1 = 1$ MHz 36

Figure 8 – Four orientations of the NV center in diamond and the ODMR spectrum with an applied static magnetic field of ~ 81G. It depicts carbon atoms in black, nitrogen (N) atoms in light-blue, and vacancies (V) in white. The NV electronic spin is indicated by red arrows and each orientation correspond to a different color in the data points. 38

Figure 9 – a) ODMR spectrum at various amplitudes B of the magnetic field. b) Contrast (drop in the photoluminescence signal) of the ODMR spectrum and c) normalized PL intensity. The solid line is the result of a rate equation model developed in Tetienne,J-P. et al. (54) 40

Figure 10 – Protocol to obtain the magnetic field with the NV center considering that the diamond chip has any crystallographic orientation. 41

Figure 11 – Representation of a resonance peak in the ODMR spectrum, describing the relevant parameter in the sensitivity analysis. 42
Figure 12 – a) Circuits for controlling the current and temperature the diode. b) Laser, 40 mW maximum 43
Figure 13 – Schematic representation of the optical microscope setup. The detection part could consist of a camera, photomultiplier or a spectrometer. . . . 44
Figure 14 – (a) Circuit diagram to control the amplitude and frequency of the RF wave that input in the AOM. (b) and (c) Response the VVA and VCO respectively. 45
Figure 15 – Schematic representation of the RF circuit. 45
Figure 16 – (a) when the laser beam diameter is 380 um, the response time of the AOM is $\sim$ 150 ns. (b) If the laser beam diameter is $\sim$ 95 um, the response time of the AOM is $\sim$ 28 ns. 46
Figure 17 – Schematic representation of the MW circuit. 47
Figure 18 – Left: Glass plate that has a copper film with a 100 nm thickness on one surface. Right: The diamond plate is positioned above a glass plate holding a single-loop antenna to apply the microwave excitation and a copper wire holding the DC current. 50
Figure 19 – CCD based wide-field fluorescence microscope: (left) schematic layout and (right) photograph of the experimental setup. 51
Figure 20 – Power broadening of the ODMR spectrum, due to the microwave power. (a) The full spectrum obtained at $\sim$ 55 gauss, showing that hyperfine levels become clear in CW-ODMR as MW power decreases. Signals are normalized to the off-resonance PL. 52
Figure 21 – (a) Detail of one peak as a function of microwave power, from 5 to 30 dBm. (b) Fit with a double Lorentzian function and one Lorentzian function.(c) Variation of the full width at half maximum (FWHM) as a function of microwave power. Points comparable to the error bar. . . . 53
Figure 22 – (a) Power broadening of one ODMR line, due to MW power, at 5 dBm and 30 dBm. (b) Signals at one pixel (indicated by the red crossing), showing a significant reduction in signal-to-noise at lower power. 54
Figure 23 – Results for one of the resonance peaks, with microwave power fixed at 15 dBm while varying the light (green laser) power. 54
Figure 24 – a) Bright-field image recorded with the CCD camera, focused on wire b), c) and d). ODMR spectrum measured in one column of the image (red dashed line), for the different sequences of images, without current, -15 mA and +15 mA, respectively. Note that the image in a) has 100×200 pixels and 1 pixel = 0.7 μm. 55

Figure 25 – a) Resonance peak in the ODMR spectrum of a single pixel the image before the binning for two set microwave power. b) Resonance peak after the binning. 57

Figure 26 – (a), (b) and (c) Components of the magnetic field the wire under a current I=15 mA in the lab frame. (d) Module of the magnetic field produced by the sample in the laboratory frame. (e) Image of the sample. (f) PL image of the area under laser excitation. 1 pixel = 1.4 μm. . . . 58

Figure 27 – a) Representation of the magnetic field produced of the ideal wire on the NV plane (red line). θ is the angle between a magnetic field $\vec{B}$ and the NV plane. b) $\tan(\theta)$ in function the y_1-axis along the black line perpendicular to the wire. 1 pixel = 1.4 μm. The connected blue dots correspond to experimental data points, determined from the magnetic image. 59

Figure 28 – Components B_x, B_y and B_z of the magnetic field created by a current $I = 15$ mA in the wire of width $W = 24\,\mu$m for various probe distance z_{NV} along the black line perpendicular to the wire, using the equations (5.7). 1 pixel = 1.4 μm. The connected blue dots correspond to experimental data points, determined from the magnetic images. . . . 60

Figure 29 – Components B_x, B_y and B_z of the magnetic field created by a current $I = 3$ mA in the wire. 1 pixel = 0.7 μm. 61

Figure 30 – (left) Representation of a sample with some planar current density $\vec{J}$, producing a magnetic field $\vec{B}$ at the NV-sensor plane. (right) Schematic diagram summarizing how to obtain the current density from the measured magnetic field. 63

Figure 31 – Components of the current density in the probe wire for I=15 mA in the lab frame. The probe distance is assumed to be $z_0 = 100$ nm. 1 pixel = 0.7μ m 64

Figure 32 – a) Two level system ($|0\rangle \rightarrow |-1\rangle$) and its geometrical representation in the Bloch sphere. b) Rabi sequence. c) Experimental (solid circles) and theoretical (solid line) of Rabi oscillations at room temperature between the $|0\rangle$ and $|-1\rangle$ levels. d) For a value of MW power, the π-pulse is defined as the MW pulse duration that gives the first minimum of fluorescence, corresponding to complete population transfer. 67

Figure 33 – Top: Ramsey sequence. Upper: the formation of a spin echo by means of a $\pi/2 - \tau - \pi/2$ pulse sequence viewed in the rotating reference frame. 68

Figure 34 – The magnetization vector is initially oriented along the z-axis (a). A $\pi/2$ pulse along x will rotate the magnetization to the y axis (b). During time τ between the first and second pulse, the different spin packets freely evolve (dephasing of the different spin packets). The π pulse inverts the y component of the individual magnetization vectors (c). After a time tau, the magnetization vectors are in phase along the y axis and a primary echo is observed (d). 69

Figure 35 – The three-pulse sequence, $\pi/2-\tau-\pi/2-T-\pi/2-\tau-\pi/2$ creates a stimulated echo at time τ after the third $\pi/2$ pulse. The equilibrium z-magnetization (a) is transferred to transverse magnetization by the first $\pi/2$ pulse (b). During free evolution of length τ, the magnetization dephases (b). The second $\pi/2$ pulse rotates the magnetization vectors into the xz plane (c). During time T, the transverse magnetization decays (c). At time $t = T + \tau$, the third $\pi/2$ pulse transfers the z-magnetization pattern again to transverse magnetization (d), which forms an echo at time $t = T + 2\tau$ along the $+y$-axis. Note that the fourth $\pi/2$ pulse is used to read the magnetization. 71

Figure 36 – The 16 resonances correspond to the different $|\Delta m_s| = 1$ transitions, four different NV orientations, and two different ^{15}N hyperfine transitions. . 72

Figure 37 – Control pulse sequence of the experimental system. 72

Figure 38 – a) Photoluminescence with MW and without MW. b) Population of the state ms=0 obtained dividing the photoluminescence with MW and without MW. 73

Figure 39 – Rabi oscillations observed using a CCD camera and the technique described in section 6.5. The blue and green dots are the experimental data for MW power at 40 dBm and 45 dBm, respectively, and the red and black lines are fits to these data. The dashed lines are the exponential envelops (as expressed in the figure) that represent the overall dephasing of the system. 74

Figure 40 – Ramsey sequence for two different detuning, $f_{MW} = 2792$ MHz (blue) and $f_{MW} = 2795$ MHz (red). The two frequencies corresponding to the two different spin states of the ^{15}N nuclear spin shape the oscillatory pattern. 75

Figure 41 – Two-pulse ESEEM, the red curve is the fit to the equation (6.8), resulting in two frequency components $f_1 = 3.022$ MHz and $f_2 = 198.84$ KHz. . . 76

Figure 42 – Three-pulse ESEEM. Data were collected with the follows conditions, MW power is 45 dBm, π-pulse is 88 ns and τ is 1450 ns. 77

Figure 43 – Pulse sequence for measuring T_1 of an NV ensemble. 78

Figure 44 – Rabi oscillation of an NV ensemble, using the imaging method. The curves were built summing a 2x2 pixel region (red curve), and summing over the full image, in a region of 200x200 pixels (blue curve). The larger sampling in the full area, results in better signal-to-noise ratio, but also in lower contrast. Here, 1 pixel = 0.6 μm 78
Figure 45 – Representation of experimental setup for femtosecond laser micromachining used to produce ablated grooves. The main elements are the laser, the translation stage, and objective lenses. 81
Figure 46 – Optical microscopy images from ablated grooves at diamond surface using femtosecond laser pulses to determine the threshold damage of the sample by the laser, the scanning speed is 10 μm/s. Objective 100x (NA = 1.25). 82
Figure 47 – Variation of the width of the optical damage as a function of the pulse energy for the diamond, using an objective x100 ($NA = 1.25$). 82
Figure 48 – Image of the confocal microscope (excitation at 543 nm) of the grooves made to calculate the damage threshold. 83
Figure 49 – Image of the confocal microscope (excitation at 543 nm) of the grooves made with low energy. 83
Figure 50 – White-light microscopy images showing the morphology damage lines written inside fused diamond at 10 μm/s for different distance between the surface and the focus the laser. The pulse energy used was 2.45 μJ and the objective used is $\times$60 (N.A = 0.85). The arrow next to the number show if the focus is inside ($\downarrow$) or up the surface ($\uparrow$) of the diamond. 84
Figure 51 – Confocal microscope image, laser excitation of $\lambda = 543$ nm. Grooves made with an objective $\times$ 60 and $NA = 0.85$. 85
Figure 52 – (a) Raman spectroscopy (He-Ne laser, 632.8, nm). We show the Raman spectroscopy onto the surface that was not damage with the laser (black line) and onto the groove 3 (blue line), see Figure 50 (b) Raman spectroscopy (Ar laser, 514nm), in another side the groove. 86
Figure 53 – Left-upper: White light microscopy image. Left-lower: The room-temperature photoluminescence. Right: PL spectra measured inside of region 1, 2 and 3 at 300K. Excitation was at 532 nm. 1 pixel = 0.7 μm. 87
Figure 54 – Zero field ODMR of the four regions. The experimental data was fit by a set of two Lorentzians. 88
Figure 55 – (a) Self-focusing for $n_2 > 0$ and (b) de-focusing for $n_2 < 0$ produced by a medium on a light beam with intensities $I(r) \propto e^{-\alpha r^2}$. 92
Figure 56 – Illustrative scheme of the experiment proposed by Sheik-Bahae to measure nonlinear refractive index and nonlinear absorption. 93

Figure 57 – Open and closed Z-scan signatures at 3.54 eV (350 nm) (a and b, respectively) and 2.21 eV (560 nm)(c and d, respectively). The inset in (a) and (b) displays the linear dependence on the transmittance change (ΔT) with the intensity at 3.54 eV (350 nm), whose slopes are approximately 1 in the log-log plot. 95
Figure 58 – Dispersion of the two-photon absorption coefficient (β) of diamond. Solid circles correspond to the experimental data obtained in this work and continuous line is the theoretical fit obtained from equation (8.17). Literature data are plotted as crosses (111), up-triangles (112), squares (101), pentagons (102) and star (113). 96
Figure 59 – Experimental (solid circles) and theoretical (solid line) dispersion of the diamond nonlinear refractive index. Squares (101), pentagons (102), star (103), cross (104) and triangles (105) correspond to the values find in the cited references. The values in (105) were increased by a factor of 4 to follow the calculation and definition of n_2 used herein. 98

LIST OF TABLES

Table 1 – Main characteristics the imaging system and the measured ODMR lines. 56
Table 2 – Raman spectroscopy. 85
Table 3 – Parameters to fit the Zero field ODMR. 88

LIST OF ABBREVIATIONS AND ACRONYMS

NV	Nitrogen-Vacancy
ZPL	Zero phonon line
ODMR	Optically detected magnetic resonance
ESR	Electron Spin Resonance
NMR	Nuclear Magnetic Resonance
CVD	Chemical vapor deposition
AOM	Acoustic optic modulator
PID	Proportional-integral-derivative
TTL	Transistor-transistor logic
DC	Direct current
MW	Microwave
VCO	Voltage-controlled oscillator
VVA	Voltage variable attenuators
APD	Avalanche photodiode
PMT	Photomultiplier tube
CCD	Chaege coupled device
SQUID	Superconducting Quantum Interference Device
EPR	Electron Paramagnetic Resonance
ESEEM	Electron spin echo envelope modulation
CPMG	Carr-Purcell-Meiboom-Gill

CONTENTS

1 INTRODUCTION . . . 25

2 NV BACKGROUND . . . 27
2.1 The Structure of the Nitrogen-Vacancy center . . . 29
2.2 Hamiltonian of the NV center . . . 31
2.2.1 Zero Field Splitting . . . 31
2.2.2 Electron Zeeman Interaction . . . 32
2.2.3 Hyperfine Interaction . . . 33
2.2.4 Nuclear Quadrupole Interaction . . . 33
2.2.5 Nuclear Zeeman Interaction . . . 33
2.3 Optically detected magnetic resonance (ODMR) . . . 35

3 MAGNETOMETRY WITH NV CENTER . . . 37
3.1 Introduction . . . 37
3.2 DC magnetometry with ensemble . . . 37
3.2.1 Sensitivity to DC magnetic fields . . . 40

4 EXPERIMENTAL SETUP . . . 43
4.1 Optical setup . . . 43
4.2 Electronic setup . . . 44

5 MAGNETIC FIELD IMAGING . . . 49
5.1 Sample preparation . . . 49
5.2 ODMR spectrum . . . 50
5.3 Magnetic field measurements . . . 55
5.4 Current density reconstruction . . . 61

6 SPIN COHERENCE MEASUREMENTS . . . 65
6.1 Introduction . . . 65
6.2 Rabi Oscillations . . . 65
6.3 Ramsey Interferometry . . . 67
6.4 Electron Spin Echo Envelope Modulation (ESEEM) . . . 68
6.4.1 Hahn Echo and the Two-pulse ESEEM . . . 69
6.4.2 Three pulse ESSEM . . . 70
6.5 Experimental Procedure . . . 71
6.6 Experimental Results . . . 73
6.6.1 Rabi sequence . . . 74

6.6.2 Ramsey sequence . . . 75
6.6.3 Two-pulse ESEEM or Hahn echo . . . 76
6.6.4 Three-pulse ESEEM . . . 76
6.6.5 T_1 spin relaxation time . . . 77

7 FABRICATION OF NV CENTERS WITH FEMTOSECOND LASER 79
7.1 Introduction . . . 79
7.2 Femtosecond laser micromachining . . . 79
7.3 Experimental Procedure . . . 80

8 NONLINEAR OPTICAL SPECTRUM OF DIAMOND AT FEMTOSECOND REGIME . . . 89
8.1 Introduction . . . 89
8.2 Nonlinear Optics . . . 90
8.3 Third-Order Nonlinear Optical Properties . . . 90
8.4 Z-scan . . . 93
8.5 Results and discussions . . . 94

9 CONCLUSION AND PERSPECTIVES . . . 99

REFERENCES . . . 103

APPENDIX 111

APPENDIX A – ELECTRON SPIN ECHO ENVELOPE MODULATION (ESEEM) . . . 113

1 INTRODUCTION

Among the several hundreds of defects that can occur naturally in diamond (1–3), the nitrogen-vacancy (NV) center, an optically active point-defect formed by a missing carbon adjacent to a substitutional nitrogen impurity in the diamond lattice, has drawn a lot of interest, mainly due to four characteristics (4–7):

1. It can be optically initialized in a well-defined quantum state, using a laser.
2. It has long coherence times at room temperature (up to few ms in single NV).
3. It is possible to create protocols to manipulate its spin-state using a combination of optical and magnetic resonance techniques.
4. Finally, the quantum states of the system can be read out by measuring its fluorescence.

This opens the possibility of exploring ideas and applications of quantum information and quantum computing even at room temperature. (8–11) The NV center is also an excellent quantum sensor, that can be used at the nanoscale because they can detect a wide variety of physical parameters such as temperature, magnetic and electric fields. (12–15) This brings great potential to this type of technology, especially in the production of ultrasensitive nanosensors, which are currently widely explored in areas such as biology and medicine, e.g., in the studies of biomolecules and cell structures. (16)

In the last years, NV diamond centers have also emerged as a promising platform for integrated photonic circuits (17–19), combining nonlinear properties, such as nonlinear refractive index, and the excellent thermal properties of the diamond (high thermal conductivity, for example), allowing the manipulation at high power. An interesting application lies in the field of quantum optics: non-linearity of diamonds can allow for frequency translation, for the wavelength range of telecommunication for example. (20)

In this thesis we conducted several studies in diamond, exploring the potential scientific and technological applications of NV centers in synthetic diamond, and, particularly, the use of engineered ensembles of NV centers for magnetometry. It is worth noting that many of the techniques studied and discussed here are also applicable to single NV centers, where coherence times can be very large, even at room temperatures.

In Chapter 2 we provide a brief introduction to the NV center, including the electronic structure and the specific photoluminescence of this atom-like point-defect. We also describe the Hamiltonian of the system. At last, we discuss the primary detection method used to probe these systems: the optically detected magnetic resonance (ODMR).

Chapter 3 provides a basic introduction of the standard techniques to measure the external magnetic field, using NV centers.

In Chapter 4 we describe the main parts of our setup, mostly the optical and electronic part, showing its versatility to develop several experiments.

In Chapter 5 we discuss several approaches to improve NV magnetic sensitivity, like reducing power-broadening and the need for an external magnetic bias field to measure weak fields. We also studied magnetic imaging with a CCD camera, capable of measuring the full vector field of an extended area with sub-micrometer resolution. As an extension of this method, we investigate how to apply these measurements to reconstruct the vector current density distribution ($\vec{\mathbf{J}}(\mathbf{r})$) on ultra-thin films of conductive materials.

In Chapter 6 we discuss some techniques for manipulating the NV spin using microwave pulses and an imaging technique that allows using a CCD camera as a detector, instead of the typical photomultiplier (PMT) or avalanche photodiode (APD), while still using extremely short pulses. This enabled us to apply different pulse sequences, such as Rabi, Ramsey and Hahn Echo, while potentially having detailed spin-coherence information over extended areas (at each pixel) of the NV ensemble.

In Chapter 7 we discussed a technique that was recently proposed (21) to create NV centers using a femtosecond laser. The centers we created using this method are characterized using Raman and fluorescence spectroscopy, as well as optically detected magnetic resonance (ODMR).

Finally, in Chapter 8 we studied nonlinear properties of diamond, conducting a study of its nonlinear refraction index in a wide spectral range. 22 We also discuss the technique known as z-scan, a versatile and relatively simple method used to obtain nonlinear properties with good precision. The studies described in Chapters 6 and 7 were developed in close collaboration with the Photonics Group, benefiting greatly from the knowledge and experience of Dr. Juliana Almeida and Prof. Cleber Mendonça.

2 NV BACKGROUND

Pure diamond is made of only carbon atoms, arranged in a regular repeating pattern, face-centered cubic (fcc) lattice structure with two atomic bases (lattice constant 3.57 A). The large forbidden energy gap between the valence and conduction band states in diamond, 5.47 eV at 300 K, makes it optically transparent and thus the absence of electronic transitions at energies in the visible spectrum. However, the transparency can be altered by the presence of a defect, such as nitrogen (N) and boron(B), in the carbon matrix. (1)

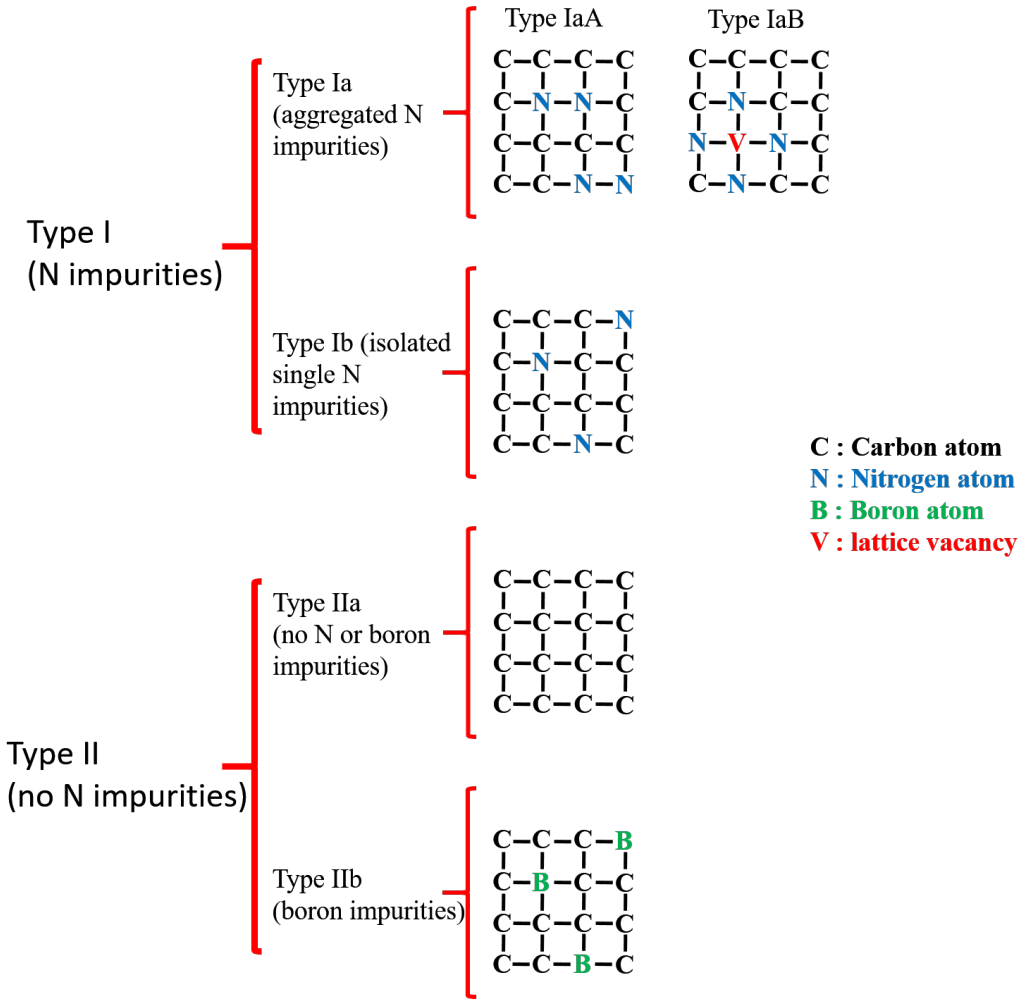

Figure 1 – Diamond type classification.

Source: By the author.

Diamond type classification is based on the presence or absence of nitrogen and boron impurities and their configurations in the diamond lattice. The schematic diagrams illustrate how nitrogen and boron atoms replace C atoms in the diamond lattice (see

figure 1). The diagrams are simplified two-dimensional representations of the tetrahedrally bonded C atoms (four bonds per C atom) that form the three-dimensional diamond crystal structure. Type Ia diamonds contain aggregated N impurities including A-aggregates (IaA), which consist of pairs of N atoms, and B-aggregates (IaB), which are made up of four N atoms around a vacancy (V). Type Ib diamonds have isolated N atoms. Type IIa stones contain no measurable impurities, and type IIb diamonds have boron impurities.

If the defect is stable inside the diamond, it gives rise to a new energy levels structure inside the diamond bandgap. The defect center can be excited by an appropriate light source, and the promotion of the electron to the excited state can result in the emission of a zero phonon line (ZPL) and a broadened phonon sideband of the electronic-phonon transitions. If the energy gap of the created level is smaller than the bandgap of the hosting material, the emission is not absorbed and can be detected as fluorescence.

The most common impurity found in diamond is nitrogen. It can be embedded in the diamond lattice in substitutional position by replacing one carbon atoms (2, 3) and this defect is usually called the P1 center (see Figure 2a), which is not optically active and acts as an electron donor in the crystal, since N possesses 5 electrons. If a N impurity is associated to a vacancy in a nearby lattice site, the defect becomes optically active and is called the nitrogen-vacancy (NV) color center (see Figure 2b).

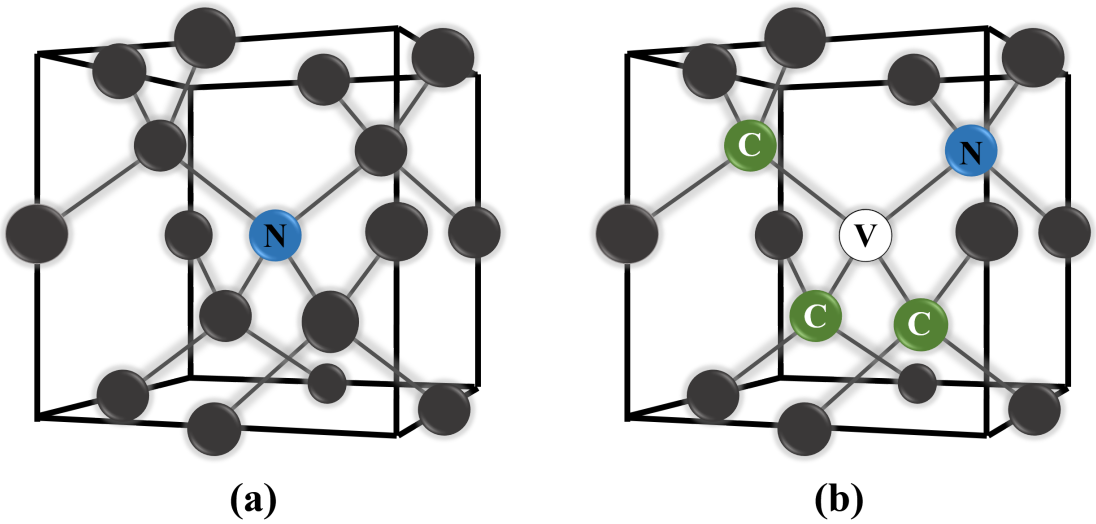

Figure 2 – a) In single-crystal type Ib diamond this environment is dominated by substitutional nitrogen defects (P1 centers). b) NV center atomic structure in diamond. We changed the color the carbon atoms to distinguish the nv center.

Source: By the author.

2.1 The Structure of the Nitrogen-Vacancy center

There are two approaches to understand the energy level of a NV center: *ab initio* calculations (4, 23–26) and semi-empirical molecular model of deep level defects in semiconductors. (27–29) Both models are complementary (30), but we limit ourselves to the details of the level structure that are relevant to the experiments described in this thesis.

The NV center possesses the C_{3v} symmetry, which implies 120^o symmetrical rotation along the axis given by the vector between the nitrogen atom and the vacancy known as the quantization axis (see Figure 3).

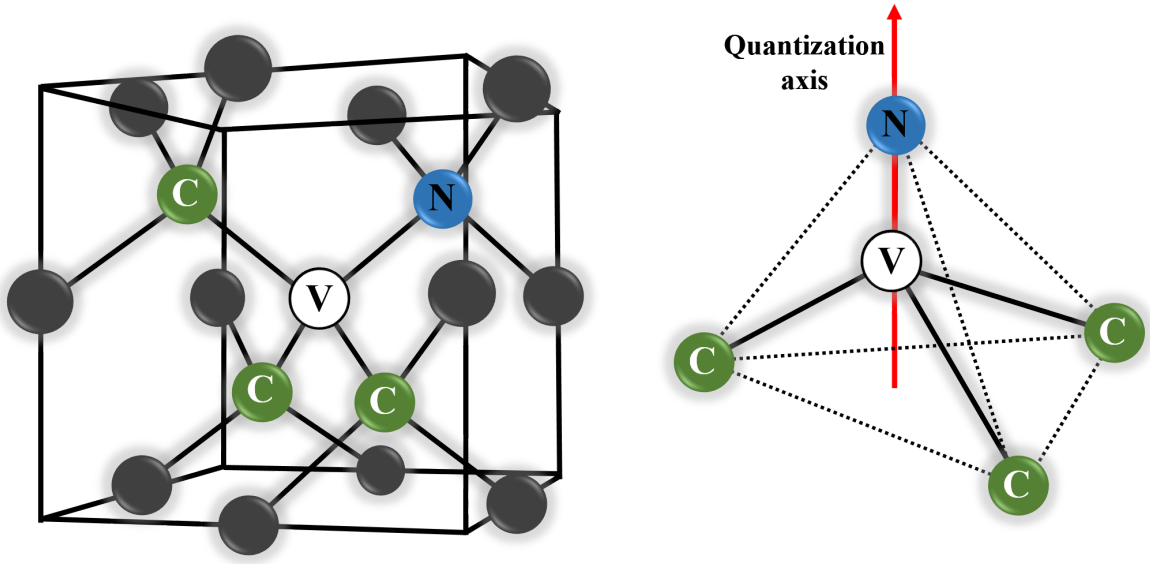

Figure 3 – Diamond unit cell with NV defect. The NV center possesses the C_{3v} symmetry and has a major symmetry axis that is defined by the direction joining the nitrogen and vacancy (quantization axis).

Source: By the author.

Experimental evidence has shown that the NV center can exist in two charge states: neutral NV^0 and negative NV^-. (30) The neutral charge state NV^0 has five unpaired electrons, four from the neighboring carbon atoms and one from the nitrogen atom. The negatively charged NV^- center, acquires an additional electron, due to this sixth electron the NV^- center has an electron spin equal to unity $S = 1$. (30–33)

NV center are excited by a 532 nm laser (green light) and emit a broadband photoluminescence signal with a Zero Phonon Line (ZPL) at 2.156 eV (575 nm) for the neutral charged state and 1.945 eV (637 nm) for negatively charged. (4,5,34) In this thesis, the focus lies on the negative charged NV^-. Consequently, the general notation **NV** in this thesis refers to the negative charge state, if not mentioned otherwise.

According to the proposed model in the references (35, 36) the NV center consist of a triplet ground state $^3A_2$ ($m_s = 0, \pm 1$) with a zero field splitting $D_{GS} = 2.87$GHz, a triplet excited state ^3E ($m_s = 0, \pm 1$) with a zero field splitting $D_{ES} = 1.42$GHz and a shelving states ^1A and ^1E involved in inter-system crossing (see Figure 4). The ground state sublevels are nearly equally populated at temperatures above ~ 1 K.

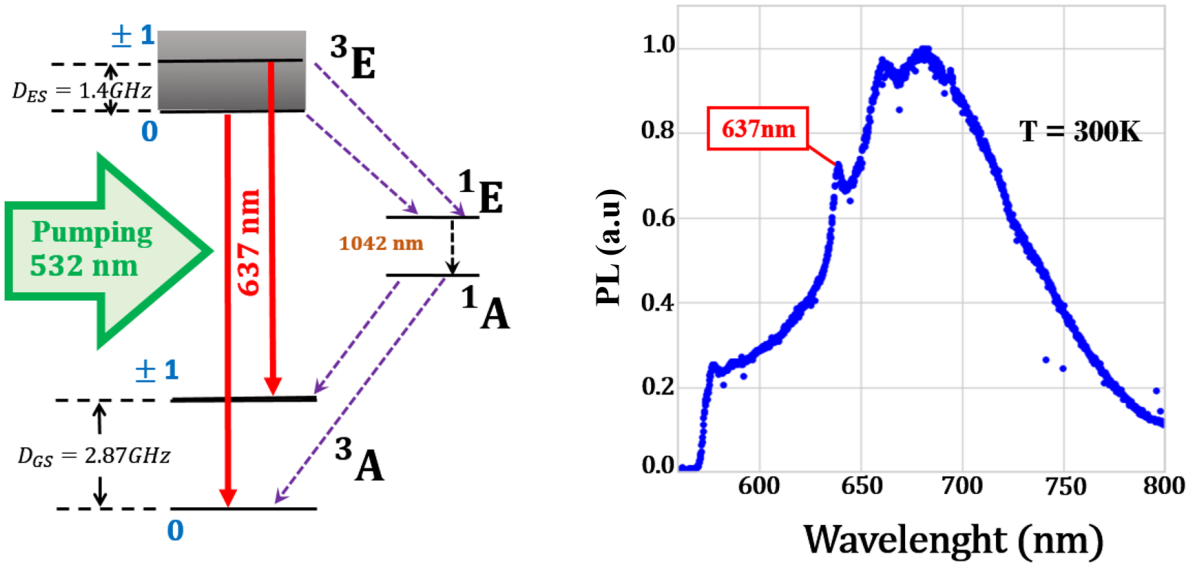

Figure 4 – Left: Energy level diagram showing the known optical transitions. The triplet ground state ^3A is split in a $m_s = 0$ and $m_s = \pm 1$ sublevel by 2.87 GHz. Right: The NV center is excited with green laser (532 nm) and decays emitting fluorescence with a ZPL at 637 nm.

Source: By the author.

The NV center can be optically excited with a green laser (532 nm) through a spin conserving transitions ($\Delta m_s = 0$) between $^3A \rightarrow {}^3E$, with a characteristic fluorescence with a ZPL at 637 nm and a broad phonon-sideband extended up to 800 nm at room temperature (Figure 4). However, relaxation can also occur via the metastable singlet level known as intersystem crossing (ISC), $^1A \rightarrow {}^1E$. The decay rate of the metastable state is slower (~ 300 ns) compared to the $^3A \rightarrow {}^3E$ transitions rate (~ 10 ns), furthermore experiments have shown that NV centers in the $m_s = \pm 1$ state are relatively more probable to undergo relaxation via the metastable states. Therefore, $m_s = \pm 1$ give less fluorescence compared to the $m_s = 0$ level in the beginning of an optical excitation. (5, 35, 37) Furthermore the states in ^1A level relaxes with higher probability to $m_s = 0$ sublevel of the ^3A ground state. (29, 31, 38, 39)

The fluorescence contrast can be as high as 30% and is limited by the branching ratios between $m_s = 0$ and $m_s = \pm 1$. (6, 31) After just a few optical cycles the system therefore occupies mainly the $m_s = 0$ state. When this occurs it is said that the system was spin-polarized by optical pumping. This enables the ability for optical readout of the

spin as well as optical initialization of the spin state, and both features are interesting to quantum information processing.

2.2 Hamiltonian of the NV center

The electron spin is mainly influenced by spin-spin and Zeeman interaction, so the level structure in the ^3A ground state, in a coordinate system with the z axis along the quantization axis, is governed by the Hamiltonian

$$H = H_{ZF} + H_Z^e + H_{hf} + H_Q + H_Z^N, \tag{2.1}$$

where H_{ZF} is the Zero Field interaction, H_Z^e is the electron Zeeman interaction, H_{hf} is the hyperfine interaction, H_Q is the nuclear quadrupole interaction and H_Z^N is the nuclear Zeeman interaction. Next, we describe these interactions. (40–43)

2.2.1 Zero Field Splitting

When the electron spin of the system is $S \geq 1$, the individual electron produces a permanent internal field, which partly removes the spin degeneracy. The Hamiltonian that describe the dipolar spin-spin interaction between two unpaired spins is

$$H_{ZF} = \frac{\mu_0}{4\pi}\left[\frac{\vec{\mu}_1^T \cdot \vec{\mu}_2}{r^3} - \frac{3(\vec{\mu}_1^T \cdot \vec{r})(\vec{\mu}_2^T \cdot \vec{r})}{r^5}\right]. \tag{2.2}$$

where $\vec{\mu}_1$ and $\vec{\mu}_2$ are two magnetic dipole moments that are far enough apart that they can be treated as point dipoles and $\vec{r}$ is the vector that joining the centers of the two dipoles. The corresponding spin operator can replace the magnetic moment operator, so the Hamiltonian becomes

$$H_{ZF} = \frac{\mu_0}{4\pi} g_1 g_2 \beta_e^2 \left[\frac{\vec{S}_1^T \cdot \vec{S}_2}{r^3} - \frac{3(\vec{S}_1^T \cdot \vec{r})(\vec{S}_2^T \cdot \vec{r})}{r^5}\right], \tag{2.3}$$

where g_1 and g_2 is the gyromagnetic factor of electrons. To simplify, let's suppose that $g_1 = g_2 = g$, then

$$\begin{aligned} H_{ZF} \;=\; & \frac{\mu_0 (g\beta_e)^2}{4\pi r^5}\left[(r^2 - 3x^2)S_{1x}S_{2x} + (r^2 - 3y^2)S_{1y}S_{2y} + (r^2 - 3z^2)S_{1z}S_{2z}\right. \\ & \left. -3xy(S_{1x}S_{2y} + S_{1y}S_{2x}) - 3xz(S_{1x}S_{2z} + S_{1z}S_{2x}) - 3yz(S_{1y}S_{2z} + S_{1z}S_{2y})\right]. \end{aligned} \tag{2.4}$$

Due to the coupling of the electrons, it is convenient to express H_{ZF} in terms of the spin operator $\vec{S} = \vec{S}_1 + \vec{S}_2$, so it can be shown that

$$S_{1x}S_{2x} = \frac{S_x^2}{2} - \frac{\mathbb{I}}{4} \tag{2.5}$$

$$S_{1x}S_{2y} + S_{2x}S_{1y} = \frac{1}{2}(S_xS_y + S_yS_x). \tag{2.6}$$

Similar expressions to (2.5) and (2.6) can be found for y, z, xz and yz, replacing these equations in (2.4) we get

$$\begin{aligned} H_{ZF} &= \frac{\mu_0(g\beta_e)^2}{4\pi r^5}\frac{1}{2}[(r^2-3x^2)S_x^2 + (r^2-3y^2)S_y^2 + (r^2-3z^2)S_z^2 \\ &\quad -3xy(S_xS_y + S_yS_x) - 3xz(S_xS_z + S_zS_x) - 3yz(S_yS_z + S_zS_y)], \end{aligned} \tag{2.7}$$

and rewriting the Hamiltonian we obtain

$$H_{ZF} = \frac{\mu_0}{8\pi}(g\beta_e)^2 \begin{bmatrix} S_x & S_y & S_z \end{bmatrix} \begin{bmatrix} \frac{r^2-3x^2}{r^5} & \frac{-3xy}{r^5} & \frac{-3xz}{r^5} \\ \frac{-3yx}{r^5} & \frac{r^2-3y^2}{r^5} & \frac{-3yz}{r^5} \\ \frac{-3zx}{r^5} & \frac{-3zy}{r^5} & \frac{r^2-3z^2}{r^5} \end{bmatrix} \begin{bmatrix} S_x \\ S_y \\ S_z \end{bmatrix}. \tag{2.8}$$

In general, we can write the Hamiltonian for $S = 0, 1$ as

$$H_{ZF} = \vec{S}^T\, \overline{D}\, \vec{S}, \tag{2.9}$$

where $\overline{D}$ describes the dipolar spin-spin interaction between two unpaired spins, from the equation (2.8) we can see that the trace of $\overline{D}$ is zero

$$\mathrm{tr}(\overline{D}) = 0. \tag{2.10}$$

In the principal axis frame (NV symmetry axis) D is diagonal, and the zero-field spin Hamiltonian is

$$H_{ZF} = D_xS_x^2 + D_yS_y^2 + D_zS_z^2 \tag{2.11}$$

$$= D_{GS}\left[S_z^2 - \frac{S^2}{3}\right] + E\left[S_x^2 - S_y^2\right], \tag{2.12}$$

where $D_{GS} = \frac{3D_z}{2}$ e $E = \frac{D_x - D_y}{2}$.

2.2.2 Electron Zeeman Interaction

For a free electron, we have an isotropic g_e factor and the electronic Zeeman interaction can be described by

$$H_Z^e = g_e\beta\vec{B}\cdot\vec{S} \tag{2.13}$$

If the crystal has paramagnetic impurity we must take into account the spin-orbit interaction, and its influence can be perceived even in a free atom, due to the coupling of angular moments of spin and orbital, this interaction is anisotropic and usually formulated by an effective Hamiltonian:

$$H_Z^e = \beta_e \vec{B}\, \overline{g}\, \vec{S} \tag{2.14}$$

where $\overline{g}$ is known as **tensor g**.

2.2.3 Hyperfine Interaction

The hyperfine interaction between the electron and nuclear spin is given by the following Hamiltonian

$$H_{hf} = \vec{S}^T\, \overline{A}\, \vec{I} \tag{2.15}$$

where $\overline{A}$ is the hyperfine tensor and $\vec{I}$ describes the nitrogen nuclear spin, which can be either $I = 1$ for the ^{14}N isotope or $I = 1/2$ for ^{15}N. For the axially symmetric case, is possible to write the tensor $\overline{A}$ as

$$\overline{A} = \begin{bmatrix} a_\perp & 0 & 0 \\ 0 & a_\perp & 0 \\ 0 & 0 & a_\parallel \end{bmatrix} \tag{2.16}$$

with $a_\perp$ and $a_\parallel$ being the perpendicular and parallel hyperfine parameters. The hyperfine interaction leads to further splittings of the possible transitions, for the ^{14}N isotope, the $m_s = 0 \leftrightarrow m_s = \pm 1$ transitions split into two triplets with $\Delta\nu = 2.2$ MHz and for ^{15}N a splitting into two doublets with $\Delta\nu = 3.1$ MHz ocurrs. (44)

2.2.4 Nuclear Quadrupole Interaction

In the case that the nuclear spins is $I > 1/2$, there is the interaction between the electric quadrupole of the nucleus with an electric field gradient that is usually established by the distribution of charges in the vicinity of the paramagnetic center, this interaction can be written Nuclei with spin

$$H_Q = \vec{I}^T\, \overline{P}\, \vec{I} \tag{2.17}$$

where the $\overline{P}$ is the quadrupole tensor.

2.2.5 Nuclear Zeeman Interaction

The spin Hamiltonian term describing the interaction of a nuclear spin with the external magnetic field is

$$H_Z^N = -\beta_N g_N \vec{B} \cdot \vec{I} \tag{2.18}$$

There are two stable nitrogen isotopes. In natural abundance, nitrogen is composed of 99.6% of ^{14}N and 0.4% of ^{15}N. The 14^N has a nuclear spin of spin $I = 1$, its total Hamiltonian is given by

$$H^{^{14}N} = D\left(S_z^2 - \frac{S^2}{3}\right) + E\left(S_x^2 - S_y^2\right) + \gamma_e \vec{B}.\vec{S} + a_\parallel S_z\, I_z + a_\perp (S_x I_x + S_y I_y) + P\, I_z^2 - \gamma_{^{14}N} \vec{B}.\vec{I} \tag{2.19}$$

where $D = 2.87$ GHz is the axial zero field splitting, $E \sim$ kHz $-$ MHz is the transversal zero field splitting, $\gamma_e = 28.8\,\frac{\text{GHz}}{\text{T}}$ is the electrons gyromagnetic ratio, $\vec{B}$ is the magnetic field vector, $a_\parallel = -2.14 \pm 0.07$ MHz and $a_\perp = -2.7 \pm 0.07$ MHz are the hyperfine terms, $\gamma_{^{14}N} = 3.077\,\frac{\text{GHz}}{\text{T}}$ is the nitrogen gyromagnetic ratio and $P = -5.01 \pm 0.06$ MHz is the quadrupole splitting.

The ^{15}N has a nuclear spin of spin $I = 1/2$, its total Hamiltonian is given by

$$H^{^{15}N} = D\left(S_z^2 - \frac{S^2}{3}\right) + E\left(S_x^2 - S_y^2\right) + g_e \beta \vec{B}.\vec{S} + a_\parallel S_z\, I_z + a_\perp (S_x I_x + S_y I_y) - \gamma_{^{15}N} \vec{B}.\vec{I} \tag{2.20}$$

where $\gamma_{^{15}N} = -4.316\,\frac{\text{GHz}}{\text{T}}$ is the gyromagnetic ratio and the hyperfine terms being $a_\parallel = -3.03 \pm 0.03$ MHz and $a_\perp = -3.65 \pm 0.03$ MHz.

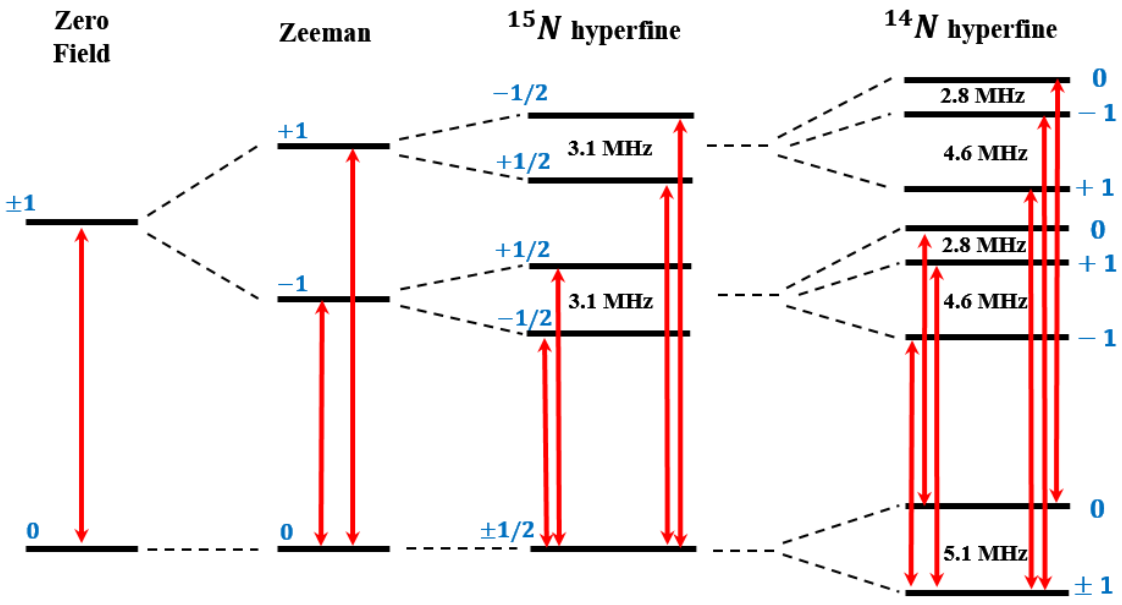

Figure 5 – The energy level scheme of the NV centre including zero-field splitting, electron Zeeman interaction and hyperfine interaction with the nitrogen nuclear spin of ^{14}N or ^{15}N.

Source: By the author.

2.3 Optically detected magnetic resonance (ODMR)

Optically Detected Magnetic Resonance (ODMR) is a powerful tool both for resolving the ground state structure and for magnetic sensing. It utilizes Electron Spin Resonance (ESR) in the NV center by examining the change in fluorescence when sweeping the microwave field along a frequency range. In the technique of ODMR, the frequency of microwave field (MW) is swipe around to the ground state of the NV center and the fluorescence resulting from illumination by laser exciting the ${}^3A \rightarrow {}^3E$ transition is monitored (30, 31). This allows to map out the energy levels, because when the microwave frequency is off resonance the fluorescence is at maximum intensity due that the optical transitions are predominantly from ${}^3A \rightarrow {}^3E$. When the microwave frequency is on resonance the population is transfered to $m_s = +1$ or $m_s = -1$, resulting in non-radiactive intersystem crossing and consequently reduced the fluorescence intensity.

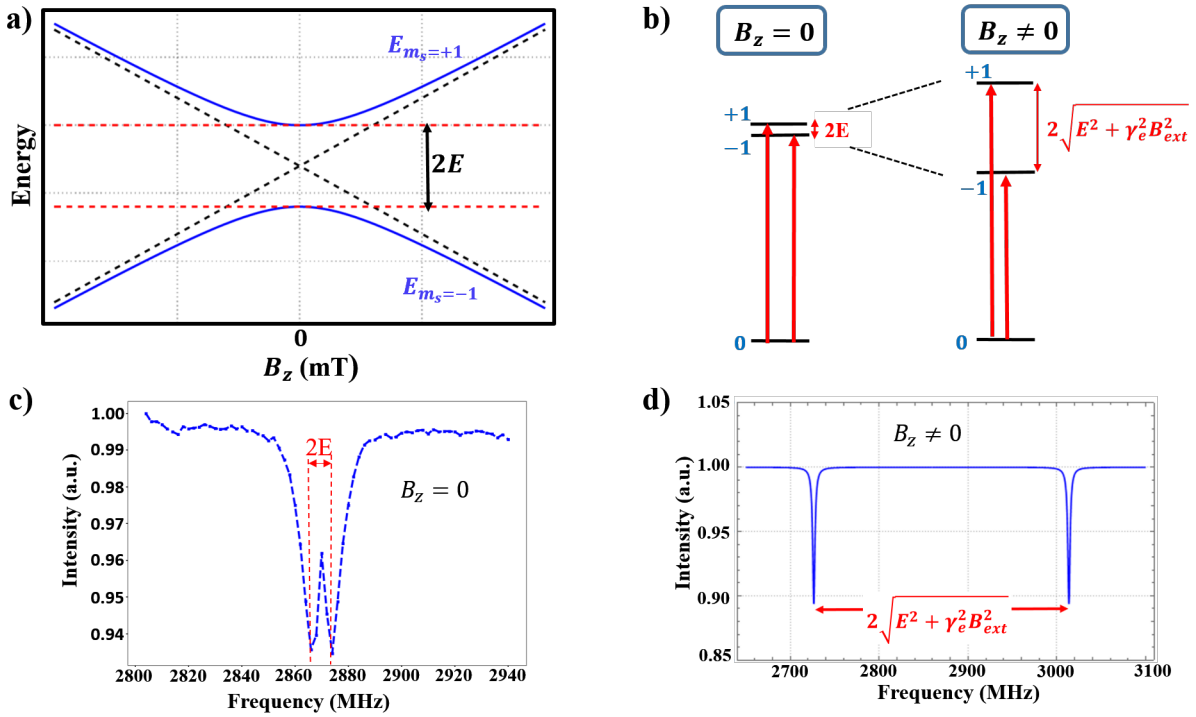

Figure 6 – a) Schematic representation of the shift of the ODMR resonance lines as a function of the applied magnetic field along the NV axis. b) NV defect structure at applied magnetic field B_z. c) ODMR spectra in a field $B_z = 0$, show two dips associated with the lattice strain. d) ODMR spectra in field $B_z \neq 0$, the two dips correspond to transitions $m_s = 0 \leftrightarrow m_s = \pm 1$ of an NV.

Source: By the author.

Figure (6) shows an ODMR spectrum of the NV center with and without a magnetic field applied along the symmetry axis. If we consider the simplest Hamiltonian, i.e. neglecting interaction with the nitrogen nucleus, the Hamiltonian of the NV can be

written as

$$H = D\left(S_z^2 - \frac{S^2}{3}\right) + E_1\left(S_x^2 - S_y^2\right) + g_e\beta\vec{B}.\vec{S} \tag{2.21}$$

and the frequencies are given by

$$f_{\mathrm{n}} = 2\sqrt{-Q}\cos\left(\frac{\phi}{3} + \frac{2\pi}{3}\mathrm{n}\right) - \frac{a_1}{3} \quad \mathrm{n} = 0, 1, 2 \tag{2.22}$$

where f_{n} are the frequencies for the spin states $m_s = 0, \pm 1$, $Q = (3a_2 - a_1^2)/9$, $R = (9a_1a_2 - 27a_3 - 2a_1^3)/54$, $\phi = \cos^{-1}\left(R/\sqrt{-Q^3}\right)$, $a_1 = 2D_1$, $a_2 = D_1^2 - E_1^2 - (g_e\beta B)^2$, $a_3 = (D_1 - E_1)(g_e\beta B_x)^2$ and $\vec{B} = \vec{B}_x + \vec{B}_z$. The Figure (7) shown the ODMR frequencies f_n, for the spin states $m_s = \pm 1$, as a function of the magnetic field $\vec{B}$ is applied with an angle θ with respect to the NV axis. One can see differents regimes depending on the magnetic field amplitude. For example, to magnetic fields smaller than 10 mT (i.e. $D >> g_e\beta B_x$) the quantization axis is the NV axis and after diagonalization of the Hamiltonian the energies are obtained

$$f_{\pm 1} = D \pm \sqrt{(g_e\beta B_z)^2 + E^2} \tag{2.23}$$

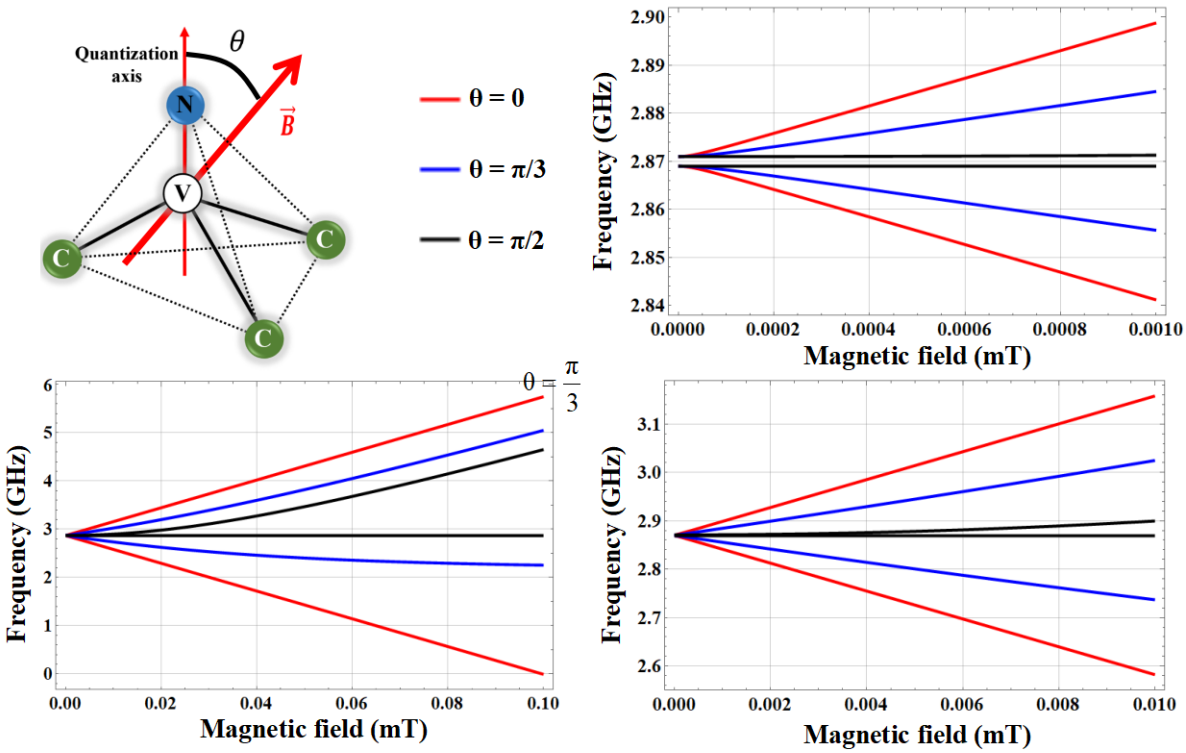

Figure 7 – ODMR frequencies f_n, for the spin states $m_s = \pm 1$, as a function of the magnetic field $\vec{B}$ is applied with an angle θ with respect to the NV axis. The lines are obtained the equation 2.22, using $D_1 = 2.87$ GHz, $g_e\beta = 28.8$ GHz/T and $E_1 = 1$ MHz

Source: By the author.

3 MAGNETOMETRY WITH NV CENTER

3.1 Introduction

The nitrogen-vacancy (NV) color center in diamond has recently emerged as a promising platform for several applications in quantum technology. One of the most promising applications is as magnetic sensors. (12, 13, 45) As mentioned in the chapter (2), the NV system possesses a combination of remarkable properties, which make it well-suited for magnetic sensing. Also, the NV spins can exhibit long coherence times (from a few μs to ms) at room temperature, and it can be used to perform sensitive magnetometry under ambient conditions. While magnetometers based on NV centers in diamond are currently less sensitive than other technologies such as SQUID magnetometers and vapor cell magnetometers, the high spatial resolution is their main advantage. (45, 46) Besides, the NV center offers the possibility to detect magnetic fields in a wide range of temperatures (from 0 K to well above 300 K), while allowing measurements of magnetic fields produced by an external source, such as a biological cell, electronic circuit, advanced materials (e.g., graphene, polymer), etc. The use of NV center for magnetometry applications has been discussed in essentially two contexts, either using a single NV center as scanning probe unit (14, 47–50) or a large ensemble of NV centers (15, 45, 51, 52) for magnetic field sensing and imaging. This chapter describes the main ideas behind the use of NV centers in magnetometry, and particularly the use of NV ensembles for imaging magnetic fields and its applications to determine currents density distributions in planar materials.

3.2 DC magnetometry with ensemble

In chapter 2 we discussed the interaction Hamiltonian of a NV center in the presence of an external magnetic field. Because of the Zeeman interaction, the projection of the magnetic field in the direction NV-axis causes energy shifts, allowing to use spectroscopy measurements to determine the magnetic field.

Diamond has C_{3v} symmetry, therefore NV centers' axis can have four possible orientations in the face-centered cubic Bravais lattice of the crystal, so there are four possible projections of the measured magnetic field along with those axes, see Figure (8). An ensemble of NV center enables a vectorial determination of the field by monitoring its projections on each possible orientation, in the crystal coordinates, by $[1, 1, 1]$, $[\overline{1}, \overline{1}, 1]$, $[\overline{1}, 1, \overline{1}]$ and $[1, \overline{1}, \overline{1}]$. Four additional orientations are possible by flipping the nitrogen atoms and vacancies in each configuration above; however, orientations with equivalent symmetry axes are spectrally indistinguishable and may, therefore, be considered in the same NV orientation class.

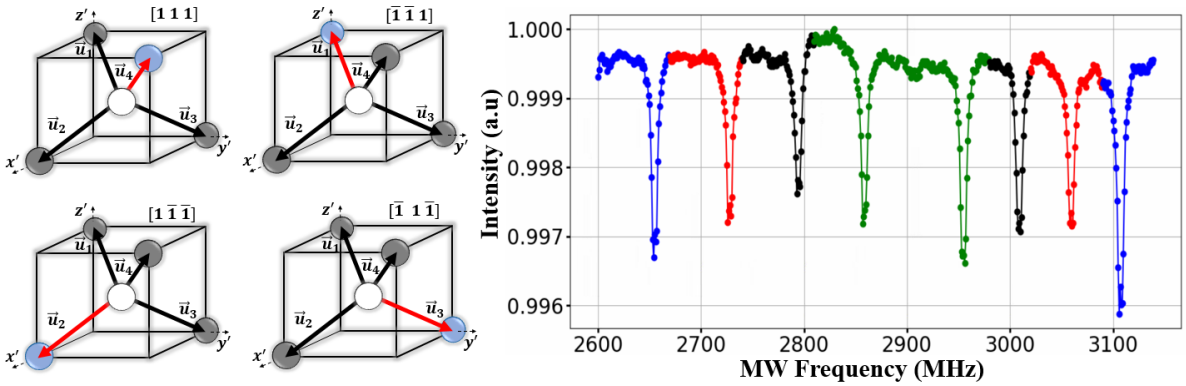

Figure 8 – Four orientations of the NV center in diamond and the ODMR spectrum with an applied static magnetic field of ~ 81G. It depicts carbon atoms in black, nitrogen (N) atoms in light-blue, and vacancies (V) in white. The NV electronic spin is indicated by red arrows and each orientation correspond to a different color in the data points.

Source: By the author.

The main idea of the method for measuring a magnetic field with NV center in diamond uses an ODMR spectrum to extract the magnetic field information from the resonance frequencies and their shifts relative to each orientation of the NV-axes. In chapter (2) we have shown that in the presence of a magnetic field, the $m_s = \pm 1$ spin states experience Zeeman splitting proportional to the projection of the magnetic field along the NV symmetry axis and when the MW frequency is on resonance with one of the $m_s = 0 \rightarrow m_s = -1$ or $m_s = 0 \rightarrow m_s = +1$ transitions, the fluorescence level decreases since the MW field spoils the NV optical pumping. Note that, each one of the four possible orientations has two resonances in the ODMR spectrum corresponding to transitions $m_s = 0 \Rightarrow m_s = +1$ and $m_s = 0 \Rightarrow m_s = -1$ respectively. We can rewrite the effective Hamiltonian for a NV center

$$H_{NV} = H_{\parallel} + H_{\perp} + E\left(S_x^2 - S_y^2\right), \tag{3.1}$$

where

$$H_{\parallel} = D\, S_z^2 + \gamma_e\, B_{NV}\, S_z \tag{3.2}$$

$$H_{\perp} = \gamma_e \left(B_x\, S_x + B_y\, S_y\right)$$

Note that, $H_{\perp}$ and $H_{\parallel}$ has the perpendicular and parallel components of the local magnetic field regarding the NV axis, respectively. As discussed in (53, 54), the zero-field splitting, $D = 2.87$ GHz, is sensitive to temperature fluctuations with a slope $dD/dT \sim -75$ kHz/K around room temperature. Those results have a major impact on performing NV-ensemble magnetometers and may ultimately limit their sensitivity.

By computing the eigenenergies of H_{NV}, we can obtain the two frequencies ν^+ and ν^- corresponding the two transitions for any magnetic field $\vec{B} = \vec{B}_x + \vec{B}_y + \vec{B}_z$. Depending of the magnetic field B (magnitude and direction), we can distinguish different regimes

- Considering that $H_\perp \ll H_\parallel$ and $\gamma_e \, (B_x^2 + B_y^2)^{1/2} \ll D$, we obtain

$$\nu^\pm = D \pm \sqrt{(\gamma_e \, B_{NV})^2 + E^2} \tag{3.3}$$

  In order to improve the sensitivity magnetometry requires one to apply a bias magnetic field such that $B_{bias} > E$, to compensate the strain-induced splitting and reach a linear dependence of the frequencies with the magnetic field (31,34,45), i.e.:

$$\nu_\pm = D \pm \gamma_e \, B_{NV}. \tag{3.4}$$

- When $H_\perp \ll H_\parallel$ is not satisfied. In this case the frequencies depended on the orientation of the magnetic field with respect to the NV axis and the quantization axis is no longer fixed by the NV defect axis in this regime, since the transverse component of the magnetic field $\vec{B}$ induces mixing of the electron spins states. (45,55)

It is also important to notice that the contrast (the drop in the photoluminescence signal) of the ODMR spectrum and the photoluminescence intensity (PL) of the NV center decrease with the magnetic field, as seen in Figure 9. In order to reduce the difficulties of operating in a strong magnetic field regime, we will mainly focus on the weak magnetic field regime (±10 mT), which typically is the most useful for NV magnetometry.

Diamonds are usually cut along one of the three crystallographic planes, (100), (110) and (111). In our case, the diamond chip has a (100) top surface. If $\vec{u}_1$, $\vec{u}_2$, $\vec{u}_3$ and $\vec{u}_4$ are the unit vectors representing the four possible orientations of the NV center, as shown in Figure 10, one sees that due to symmetry properties they are related by

$$\hat{u}_1 + \hat{u}_2 + \hat{u}_3 + \hat{u}_4 = 0. \tag{3.5}$$

Assuming a convenient axes system (x', y', z'), we define

$$\hat{u}_1 = \frac{\hat{i}' + \hat{j}' + \hat{k}'}{\sqrt{3}}; \quad \hat{u}_2 = \frac{-\hat{i}' - \hat{j}' + \hat{k}'}{\sqrt{3}}$$

$$\hat{u}_3 = \frac{\hat{i}' - \hat{j}' - \hat{k}'}{\sqrt{3}}; \quad \hat{u}_4 = \frac{-\hat{i}' + \hat{j}' - \hat{k}'}{\sqrt{3}}, \tag{3.6}$$

such that each axes (x', y', z') are to be related to the laboratory frame (x, y, z), where z is usually defined normal to the diamond surface and here we assume that x is parallel to the edges of the image. The next step is to reconstruct the external magnetic field in the laboratory frame, using $\vec{B} = B_x\hat{i} + B_y\hat{j} + B_z\hat{k}$

$$\vec{B} \cdot \hat{u}_1 + \vec{B} \cdot \hat{u}_2 + \vec{B} \cdot \hat{u}_3 + \vec{B} \cdot \hat{u}_4 = 0, \tag{3.7}$$

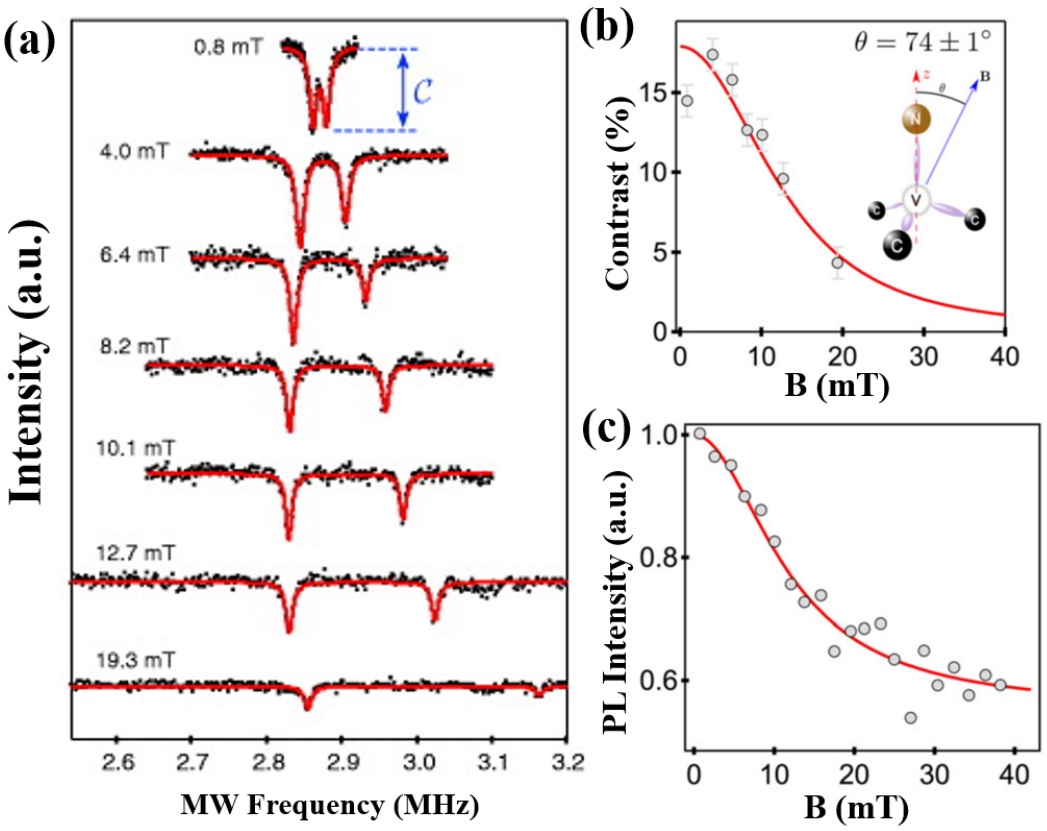

Figure 9 – a) ODMR spectrum at various amplitudes B of the magnetic field. b) Contrast (drop in the photoluminescence signal) the ODMR spectrum and c) normalized PL intensity. The solid line is the result of a rate equation model developed in Tetienne, et al. (55)

Source: Adapted from TETIENNE, et al. (55).

and

$$\vec{B} \cdot \hat{u}_i = B^i_{NV} \tag{3.8}$$

where B^i_{NV} is projection of the magnetic field along the i-axis of NV.

Figure 10 shows a typical protocol that can be used to determine the vector B field. From equation (3.8), one can use a least-square minimization algorithm to obtain the best estimate of B_x, B_y and B_z for each pixel. It is interesting to notice that the fact that this protocol is based on changes in frequency, instead of direct measurements of the fluorescence, conveniently filters out some of the noise sources such as laser instability and inhomogeneity of the NVs concentration.

3.2.1 Sensitivity to DC magnetic fields

Static magnetic field sensing with NV centers is based on ODMR spectroscopy. To derive the optimum sensitivity of an NV magnetometer to measure DC magnetic field, we consider the intensity profile of an NV resonance in the ODMR spectrum with the parameters described in Figure 11.

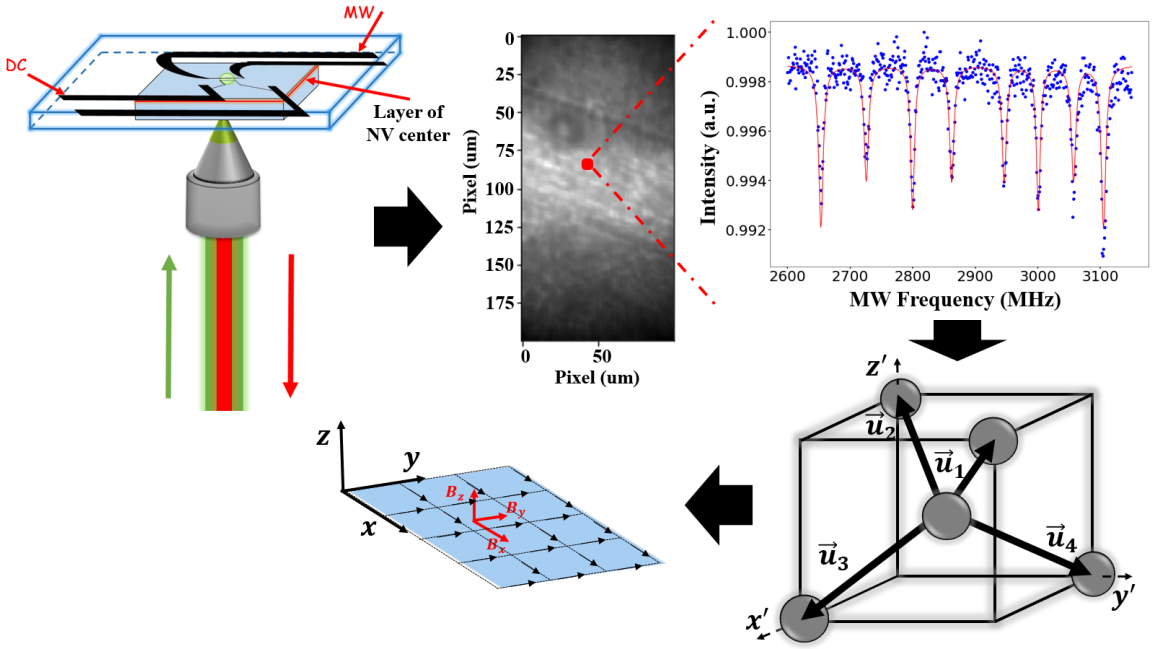

Figure 10 – Protocol to obtain the magnetic field with the NV center considering that the diamond chip has any crystallographic orientation.

Source: By the author.

In general, the lineshape of the resonance may be described by a Gaussian function (e.g., when a large number of nuclear ^{13}C spins dominate the dephasing), a Lorentzian function (e.g., when paramagnetic spins corresponding to nitrogen defects dominate the dephasing or when the resonance is power-broadened due to continuous laser or microwave excitation), or possibly a convolution of both (i.e., a Voigt function), (56–59), so, the intensity I of optically detected ODMR spectra as a function of the microwave frequency (f) can be written as

$$I(f) = R\left[1 - \alpha F\left(\frac{f - f_0}{\Delta f}\right)\right] \tag{3.9}$$

where R is the rate of detected photons per second, α is the resonance contrast, F is a function describing the lineshape, Δf is the linewidth, and f_0 is the resonance frequency.

The fluorescence intensity (I) is most sensitive to the magnetic field at the point of maximum slope:

$$\max\left|\frac{\partial I}{\partial f}\right| = \frac{\alpha R}{\Delta f P_f} \tag{3.10}$$

where P_f is a numerical parameter related to the specific profile F of the resonance. For Gaussian profile, $P_f = \sqrt{e/(8\ln 2)} \approx 0.7$, whereas a Lorentzian profile leads to $P_f = 4/\sqrt{27} \approx 0.77$.

Any magnetic field fluctuation δB induces a shift of the central frequency f_0 through the Zeeman effect. The photon shot noise of measurement with duration Δt has a standard

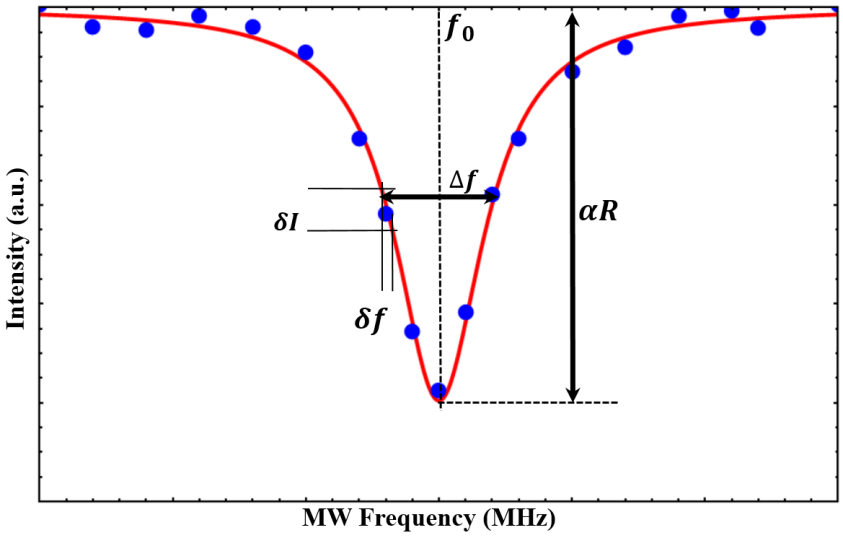

Figure 11 – Representation of a resonance peak in the ODMR spectrum, describing the relevant parameter in the sensitivity analysis.

Source: By the author.

deviation $\sqrt{I\Delta t}$. At low contrast ODMR, the shot-noise-limited magnetic field sensitivity η of the measurement is then given by the following relation (56, 59)

$$\eta = \delta B_{min}\sqrt{\Delta t} \approx \frac{h}{g\mu_B}\frac{\sqrt{R}}{\max|\partial I/\partial f|} \tag{3.11}$$

that becomes

$$\eta \approx P_f \frac{h}{g\mu_B}\frac{\Delta f}{\alpha\sqrt{R}} \tag{3.12}$$

Note that the parameters involved in the equation to obtain the sensitivity are not independent of each other, e.g., the resonance contrast α may be increased by increasing the power of the MW excitation at the expense of increasing the linewidth Δf due to power broadening. Using these relations, one can determine the best set of parameters to achieve the desired sensitivity of the magnetic field using this method.

4 EXPERIMENTAL SETUP

As discussed in chapters 2 and 3, the electron spin of the NV^- center can be initialized and read-out optically, while the control and manipulation of internal quantum spin states are done using microwave (MW) fields. For this purpose, we home-built a setup with the possibility of realizing fluorescence spectroscopy and ODMR spectroscopy, in addition to fast-pulse sequences for spin control, which are briefly described in this chapter.

4.1 Optical setup

The optical excitation of the NV center used a green laser (Thorlabs, DJ532-40) operating at 532 nm wavelength. To control the temperature and the current of the diode, we built two circuits. The first circuit maintains the constant current and the second circuit stabilizes the temperature, and it can be adapted to different thermal loads via a Proportional-Integral-Derivative controller (PID controller), see Figure 12.

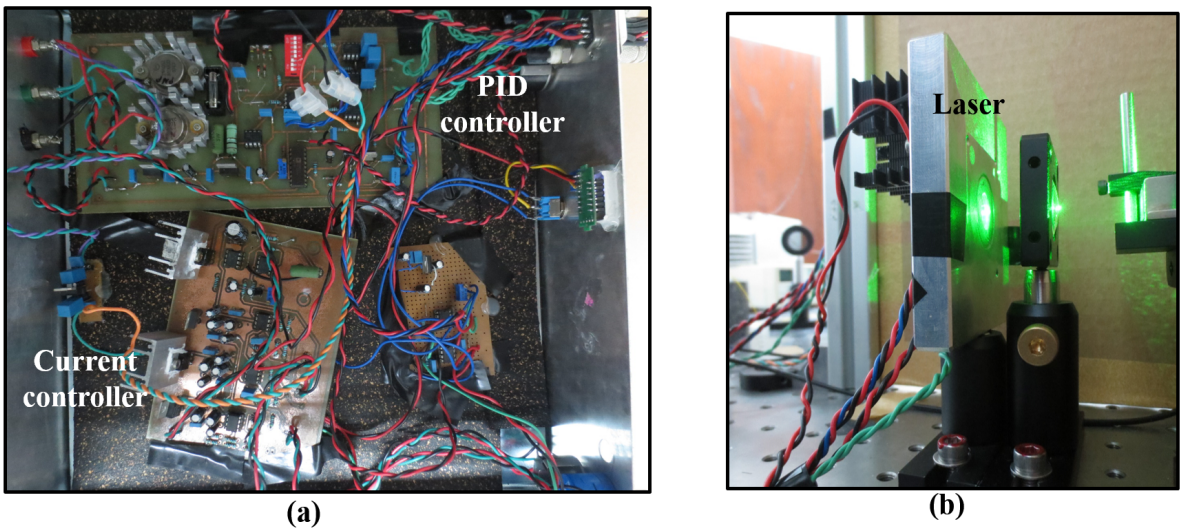

Figure 12 – a) Circuits for controlling the current and temperature the diode. b) Laser, 40 mW maximum

Source: By the author.

We can use pulsed and continuous-wave operating regimes. For experiments with the pulsed laser, we use an acoustic-optic modulator (AOM), as is shown in Figure 13. When the AOM modulation input is driven with a Radio frequency wave (ON), the laser light is subject to a diffraction pattern. The iris selects only the first order deflection, and therefore in the absence of Radio frequency at the modulation input (OFF), no light will

be passed. The RF is generated by an AOM driver with a Transistor-Transistor Logic (TTL) input, see Figure 15. After of the iris, the laser is expanded and collimated with two lenses to obtain a beam diameter of ∼10 mm. We focused the collimated beam through a microscope objective which can be x100 (Zeiss, oil immersion 1.4 NA) or x50 (Zeiss, 0.95 NA), depending on the experiment. The position control of the sample is done with a slide holder mounted on a nanopositioning stage (Thorlabs, NanoMax 300) which enables translations within three axes.

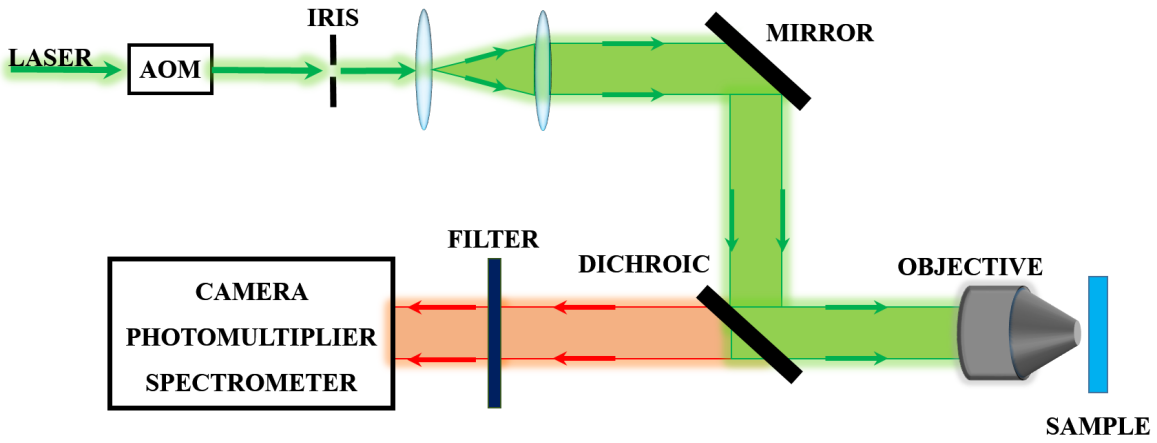

Figure 13 – Schematic representation of the optical microscope setup. The detection part could consist of a camera, photomultiplier or a spectrometer.

Source: By the author.

The emitted photoluminescence by NV centers is collected by the same microscope objective, filtered with a dichroic 561 nm (SemRock, Di02-R561-25x36) mirror and long pass filter 550 nm (FELH0550). This combination allows us to cut residuals of green laser light while keeping most of the light emitted by the NV center. The detection of the collected photoluminescence is realized with a camera (PointGrey, FL3-FW-03S1M-C), a photomultiplier (Hamamatsu, R1477-06) or a spectrometer (Ocean Optics, USB 4000), depending on the experiment which we want to make.

4.2 Electronic setup

We implemented an electronic circuit Figure 14 to change the frequency (Voltage-controlled oscillator (VCO), Mini-circuits, ZX95-200-S+) and the amplitude (Voltage Variable Attenuators (VVA), Mini-circuits, ZX73-2500-S+) of the RF. We choose the value of frequency and power such that the first order deflection of the laser to be maximum. After the RF is directly guided to a switch (Mini-circuits, ZASWA-2-50DR+). To control the switch we use a high-speed, programmable, multichannel Pulse Generator (Spincore, PulseBlaster, PBESR-PRO-300). The RF is guided to the power amplifier (Mini-circuits,

ZHL-03-5WF), see Figure 15. Finally, the amplified RF is conducted to the AOM (G&H 3110-120), in this way we can turn the laser (first order deflection) on and off.

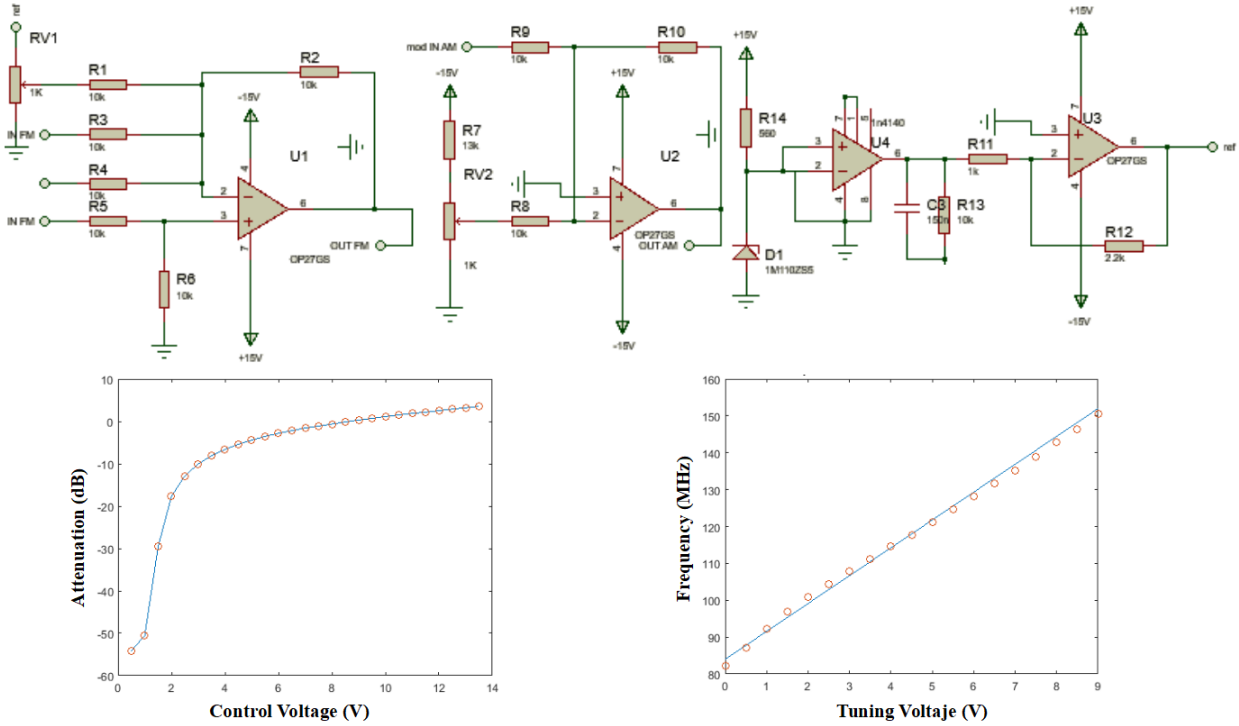

Figure 14 – (a) Circuit diagram to control the amplitude and frequency of the RF wave that input in the AOM. (b) and (c) Response the VVA and VCO respectively.

Source: By the author.

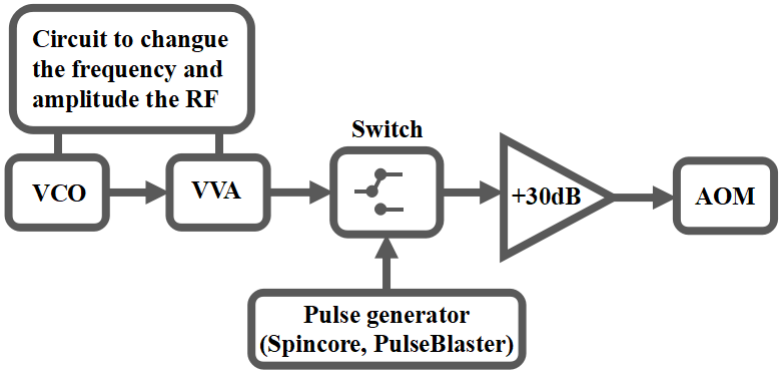

Figure 15 – Schematic representation of the RF circuit.

Source: By the author.

In order to measure the relevant lifetimes of the NV center, is important to determine the delay of the acousto-optic modulator (AOM) and the response time, for that we use a Photomultiplier Tube (PMT, Hamamatsu H9305 – 03) which has a response

time of 1.5 ns. We observe that the response time depends on the diameter of the laser beam at the AOM crystal, while the time delay between the pulse of the SpinCore and the PMT depends on the lateral distance from the beam axis and the piezoelectric transducer. We configured our setup to minimize those times, resulting in a response time of the AOM is 28 ns and delay time of 680 ns, as shown in Figure 16.

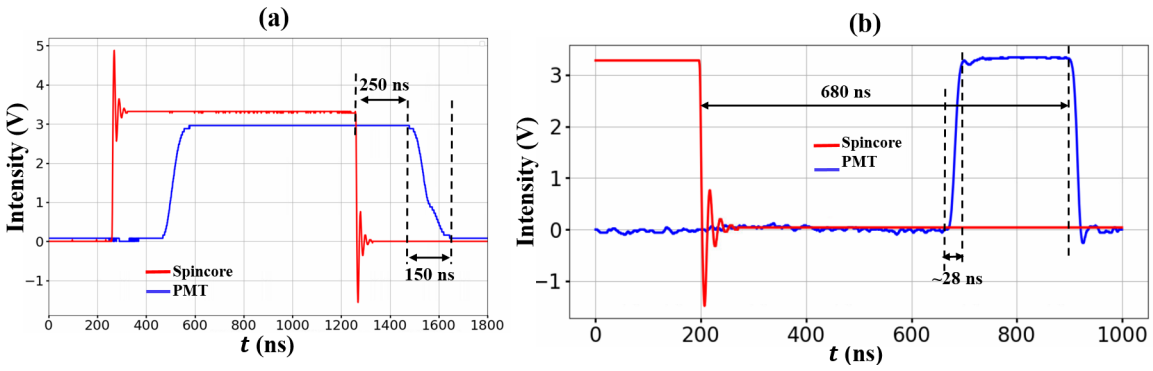

Figure 16 – (a) when the laser beam diameter is 380 um, the response time of the AOM is $\sim$ 150 ns. (b) If the laser beam diameter is $\sim$ 95 um, the response time of the AOM is $\sim$ 28 ns.

Source: By the author.

For the excitation of the NV electron spin with microwave, we used a setup consisting of a Signal Generator (Stanford Research, SG384), connected to a fast switch (CMCS0947A-C2) to control the MW pulse. For experiments using continuous wave (CW) excitation, the output of the synthesizer is directly guided to the power amplifier (Mini-circuits, ZHL-16W-43-S). For pulsed experiments, we implemented from a Pulse generator (Spincore, PulseBlaster, PBESR-PRO-300) to generate the TTL pulse sequence corresponding to the pulsed microwave excitation with the time resolution of 3.3 ns and to control the microwave signal we use a switch.

A microwave circulator (CS-3.000, 20 Watts, 2.0-4.0 GHz), connected at the amplifier output, protects the power amplifier from reflections caused by impedance mismatches. The backward port of the circulator coupler is terminated at a 50 Ω heavy-duty load, but can also be used to determine the level of the excitation power which is reflected at the micro-strip-line, see Figure 17.

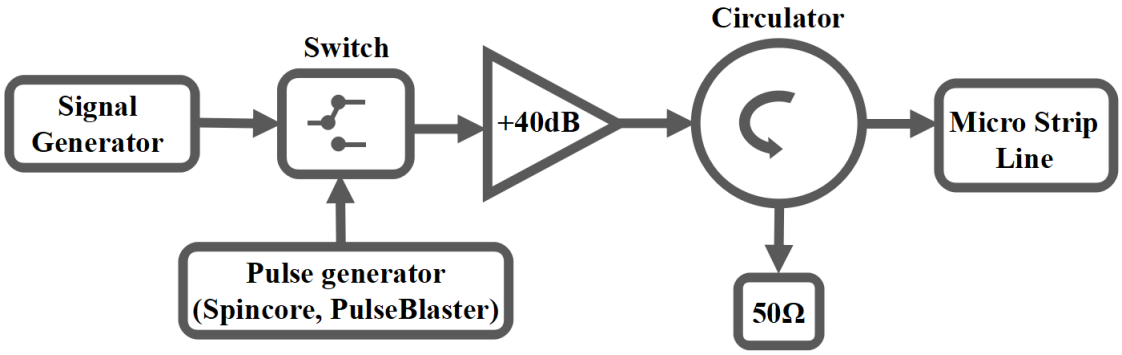

Figure 17 – Schematic representation of the MW circuit.

Source: By the author.

5 MAGNETIC FIELD IMAGING

In this chapter, we show results for imaging a magnetic field vector using an ensemble of NV centers in a thin layer near the surface of a diamond chip. The method allows finding the full vector field at each point in the NV plane, by combining ODMR spectroscopy with the ability to image onto a CCD camera the fluorescence from the NV centers. The primary goal was to build a simple setup to calibrate the basic method described in chapter 3 and to develop and study an interesting new application of this technology, towards mapping of current density distributions in 2D materials, such as thin films of organic field-effect transistors (OFETs).

To do that, we started by measuring the magnetic field produced by a simple test circuit (DC circuit, in Figure 18) that we etched onto a thin glass plate. On the same surface of the glass plate, we also etched the microwave line (MW circuit) to control the spins of the NV centers, maximizing the intensity of the microwave field. The diamond chip (our sensor) was placed over these circuit lines, on the glass surface, trying to place the NV layer as close as possible to these lines, as shown in Figure 18.

In order to demonstrate the imaging capabilities of NV ensembles in diamond, we custom built a wide-field fluorescence microscope where we added an extra lens in the optical path for the excitation green (532 nm) laser, before the objective (Zeiss 50x, 0.93 NA), to focus the collimated beam at the back aperture of the objective. The lens allows controlling the size of the irradiated area on the NV layer, by adjusting the beam spot size on the diamond surface, at the imaging plane of the microscope. We combine the optical paths for the excitation and fluorescence in a dichroic mirror (Semrock, Di02-R561-25x36). Figure 19 shows a simplified schematic and a picture of this setup.

5.1 Sample preparation

We built our 2D sensor from an ultra-pure diamond plate, that is made by Chemical vapor deposition (CVD), where a thin layer of NV centers was created near the top surface. Ion implantation produced the NV layer, irradiating the surface with $^{15}N^{+}$ ions at 5 keV and density of 1×10^{13} $^{15}N^{+}/cm^{2}$. Under these conditions, it creates a layer of nitrogen at around 8 to 16 nm below the surface (15,60,61), in addition to a number of vacancies along the nitrogen collision path. Following the implantation, the sample was annealed at 800 ^{o}C for a couple of hours, in vacuum, to allow the migration and trapping of the vacancies to the implanted nitrogen, which normally produces a 0.8% yield in the conversion of N to NV^{-}, and results in an estimated density around 10^{3} NV/μm^{2} (62,63).

The crystal is a (100) oriented plate whose edges coincide with axes [100], [010]

and [001], which represent the lab reference frame, denoted here as (x, y, z). The electronic grade single crystal was thinned and polished to a $2 \times 2 \times 0.1$ mm^3 size. We chose this thickness to help the collection of the photoluminescence from the NV layer, through the back face of the diamond plate, from where an inverted microscope is focused on the top surface, while, because of the small distance, the NV layer is still within the focal distance of the microscope.

The microwave antenna and test wire were prepared in-house using thin glass plates where a copper film of 100 nm thickness was deposited on one surface, by sputtering. We designed these circuits to be as simple as possible and easy to make, and printed it on photo paper or glossy paper, using a laser printer. After applying the printed pattern on an adequately cleaned copper surface, for 10 minutes, using a hot iron, we remove the paper, and we put the print-transferred plate into a chemical etching solution (ferric chloride solution) for about 30 seconds to removes the unwanted copper from the glass plate. Then, we rinsed it with water and cleaned with a few drops of thinner (nail polish remover works well) on a pinch of cotton to remove the ink completely on the plate, exposing the copper surface. Finally, the microwave and DC circuits were soldered to thicker copper lines etched on usual electronics circuit boards, where proper electrical connectors are attached (like a SMA connector for the microwave).

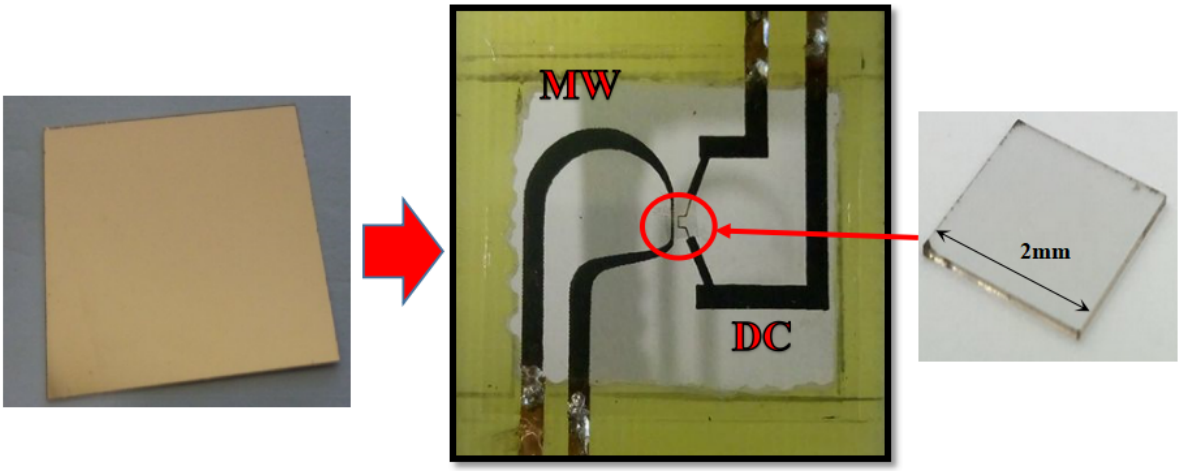

Figure 18 – Left: Glass plate that has a copper film with a 100 nm thickness on one surface. Right: The diamond plate is positioned above a glass plate holding a single-loop antenna to apply the microwave excitation and a copper wire holding the DC current.

Source: By the author.

5.2 ODMR spectrum

As described in chapter 3, an ensemble of NV centers in bulk diamond allows for the determination of the full vector field, due to the four different orientations of the

NV axis. To take advantage this useful feature, we used a permanent magnet to apply a static bias field, splitting the resonances into eight lines, whose visibility depends on the orientation of the magnet. By carefully aligning the magnet we were able to find all the eight peaks with approximately the same intensities in the ODMR spectrum. Figure 19 shows a picture of the relevant part of the apparatus, showing the position of the permanent magnet, relative to the NV sample.

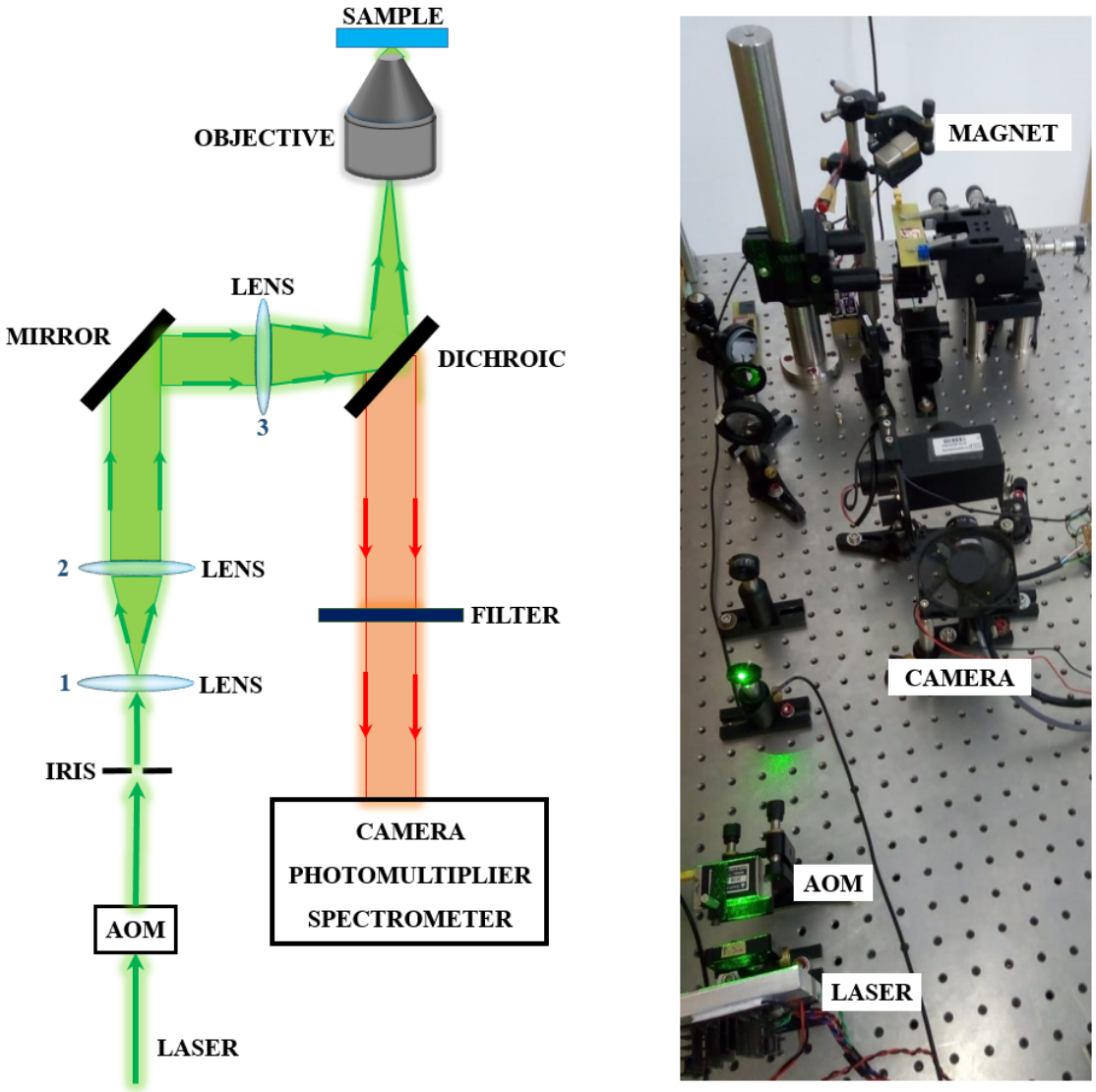

Figure 19 – CCD based wide-field fluorescence microscope: (left) schematic layout and (right) photograph of the experimental setup.

Source: By the author.

To find the optimal magnetic sensitivity, we study the linewidth and contrast of the spectrum ODMR for different microwave powers. For that, the diamond plate (described previously) was located in a static magnetic field of 55 G produced by the permanent magnet. The microwave field is produced by a computer controlled digital synthesizer and

amplified as described in chapter 4.

The ODMR spectrum comprises 64 images taken at each frequency, scanned using steps of 0.5 MHz, resulting in 44800 images and corresponding to about 15 GB of raw data for each full spectrum (one trace in Figure 20). After proper processing, the procedure allows building the ODMR spectra for each pixel in the fluorescing area, which can be then used in the analysis to determine the local (vector) magnetic field at the location represented by each pixel. In addition, one can build an averaged ODMR by summing pixels in a region of interest (ROI), to find the corresponding averaged field for that ROI. Figure 20 shows an example of the sum of all the pixels, where one sees a much cleaner signal, due to substantial improvement in signal-to-noise, as seen in Figure 22. Depending on the desired spatial resolution and signal-to-noise, one can do a binning of several pixels (or to apply convolution kernel-filtering) to reduce the noise level at each pixel, as we discuss later.

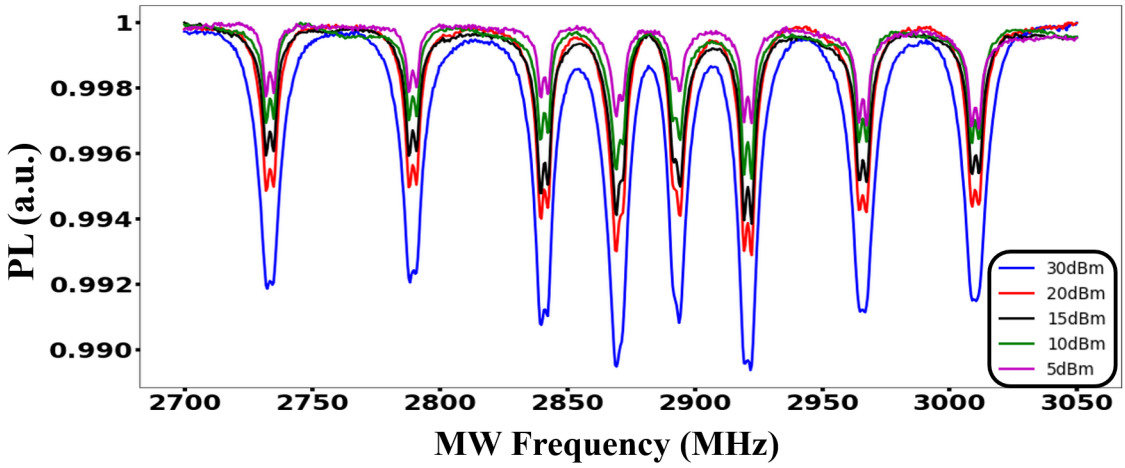

Figure 20 – Power broadening of the ODMR spectrum, due to the microwave power. (a) The full spectrum obtained at ~ 55 gauss, showing that hyperfine levels become clear in CW-ODMR as MW power decreases. Signals are normalized to the off-resonance PL.

Source: By the author.

In Figure 20, the ODMR signals are normalized to the signal obtained when the microwave frequency is detuned far from resonance, and each spectrum was taken at different microwave powers. It is possible to observe that at power levels lower than 20 dBm the resonance becomes sufficiently narrow to resolve the hyperfine interaction with the nuclear spin of ^{15}N ($I = 1/2$), with a splitting around 3 MHz. The figure also shows the behavior for power dependence of the full-width at half-maximum (FWHM), extracted from the spectrum using a fit with a double Lorentzian function, see Figure 21.

These results show that, at least in principle, one could enhance the magnetic field

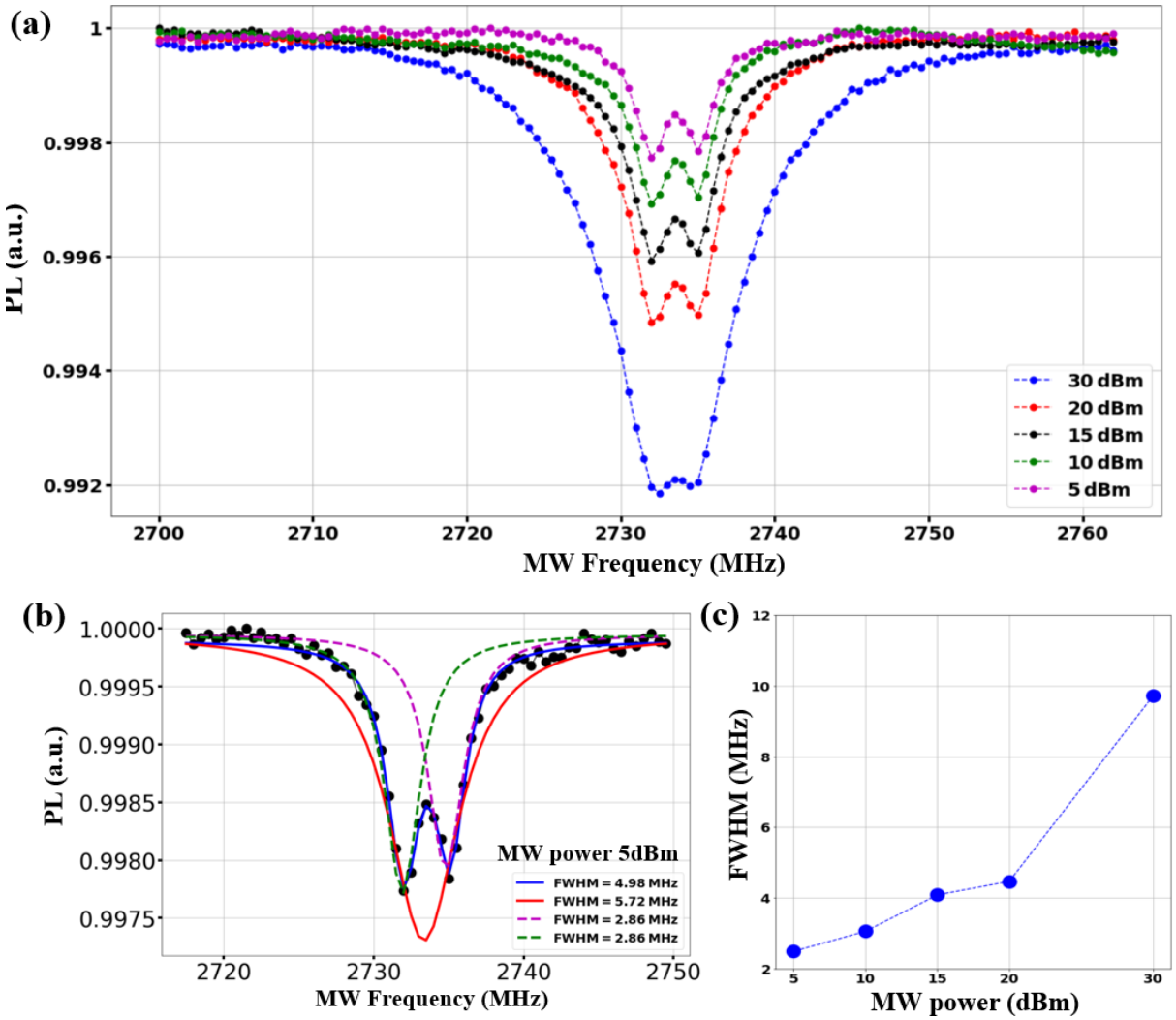

Figure 21 – (a) Detail of one peak as a function of microwave power, from 5 to 30 dBm. (b) Fit with a double Lorentzian function and one Lorentzian function.(c) Variation of the full width at half maximum (FWHM) as a function of microwave power. Points comparable to the error bar.

Source: By the author.

sensitivity by decreasing the microwave power to reduce the FWHM. However, one pays a significant reduction in signal contrast. (59) This is notably troublesome when trying to determine the resonance frequencies at each pixel, as shown in Figure 22, where the signal is comparable to the noise.

Previous studies (64–66) have observed that the power of the green laser has the opposite effect on the resonance width, decreasing the ODMR linewidth by increasing the laser power, due to increased optical pumping to $m_s = 0$.

In our case, fitting the spectral data reveals that increasing light power we observed only a slight decrease in the linewidth and some increase in the contrast, as seen in Figure

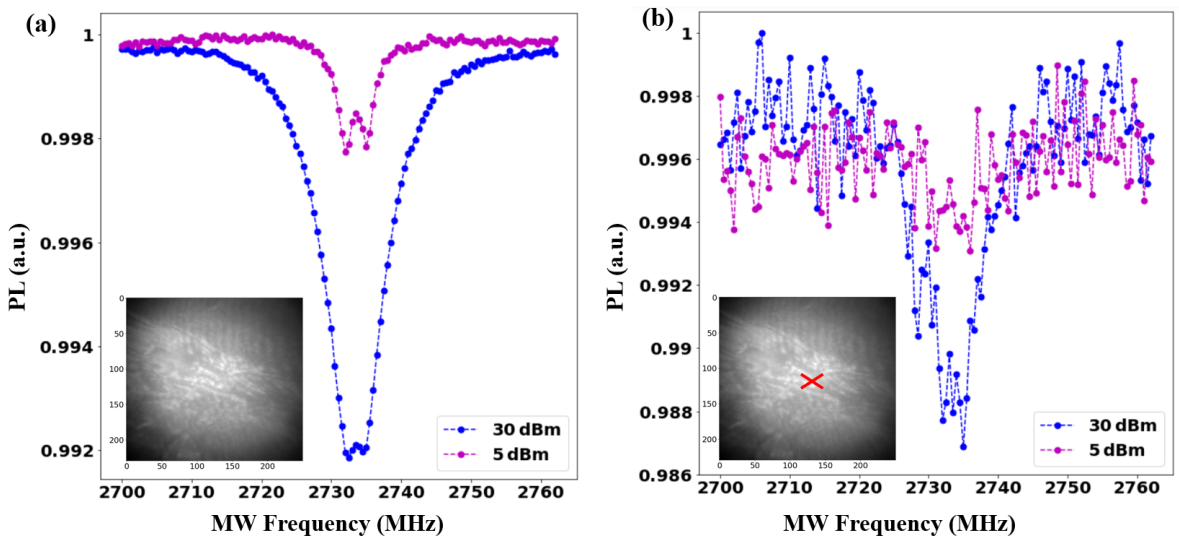

Figure 22 – (a) Power broadening of one ODMR line, due to MW power, at 5 dBm and 30 dBm. (b) Signals at one pixel (indicated by the red crossing), showing a significant reduction in signal-to-noise at lower power.

Source: By the author.

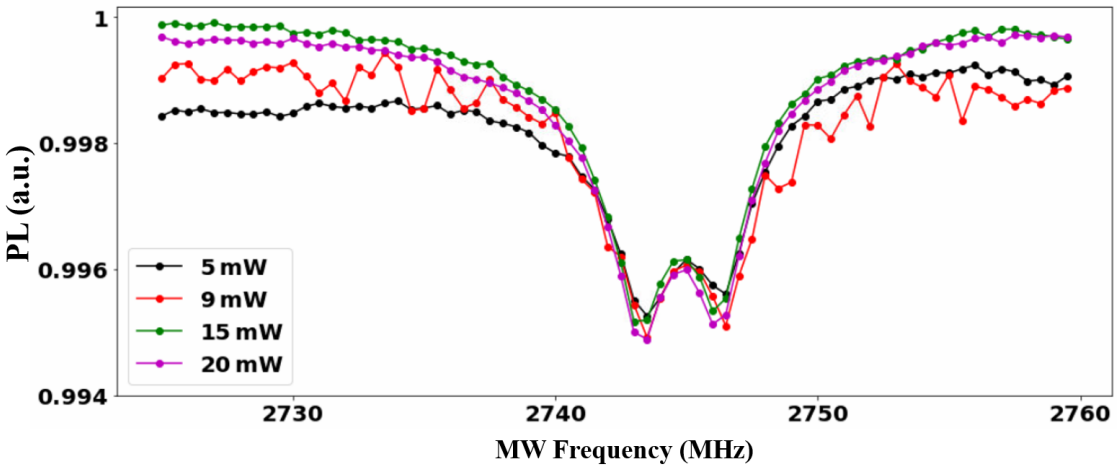

Figure 23 – Results for one of the resonance peaks, with microwave power fixed at 15 dBm while varying the light (green laser) power.

Source: By the author.

23, but we were limited in the laser intensity available.

5.3 Magnetic field measurements

As we discussed in the chapter 3 , when a static external magnetic field B is applied to the NV defect the levels corresponding to $m_s = 1$ and $m_s = -1$ are shifted due to Zeeman interaction and their resonance frequencies; ν^-, ν^+ respectively; are shifted. The Zeeman splitting are given by

$$\Delta\nu = 2\,|\gamma_e\, B_{NV}| \tag{5.1}$$

where $\gamma_e = 28$ MHz/G is the electron spin gyromagnetic ratio, B_{NV} is the projection of the magnetic field along the NV axis and $\Delta\nu = \nu^+ - \nu^-$.

Equation (5.1) shows the frequency splitting due to the external magnetic field. Therefore, to measure the small magnetic field of our test circuit (copper wire), we applied a known static bias field along a direction to distinguish the eight peaks due to the different orientations the NV centers. We chose an external bias field that is larger in magnitude than the local measured (test) field, to ensure that the sign of the total field is the same as the sign of the probed field, simplifying the analysis. Hence, when we subtract the external field from the total field, we get the local field with the proper sign. Another approach would be to do differential measurements of opposite signs currents directly. When an

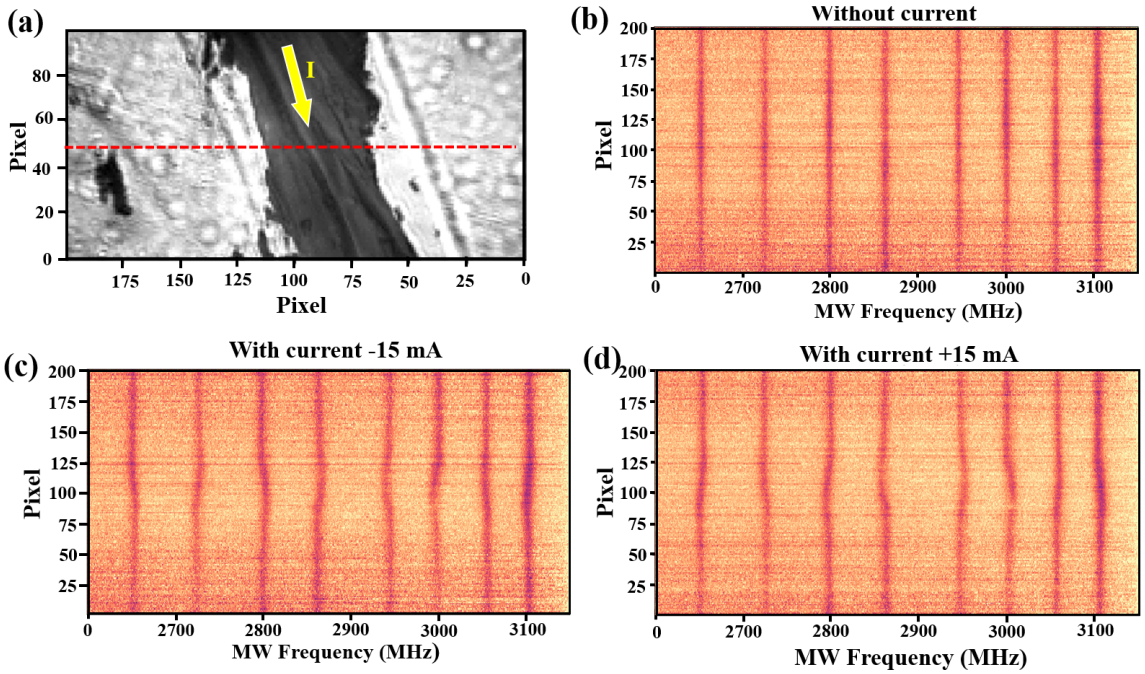

Figure 24 – a) Bright-field image recorded with the CCD camera, focused on wire b), c) and d). ODMR spectrum measured in one column of the image (red dashed line), for the different sequences of images, without current, -15 mA and +15 mA, respectively. Note that the image in a) has 100 × 200 pixels and 1 pixel = 0.7 μm.

Source: By the author.

electric current passes through the test circuit wire, we observe shifting in the ODMR

spectrum, due to the magnetic field produced around the wire. Note that the frequency splittings in the ODMR spectrum, caused by the current in the wire, are identical in absolute value for both directions of current. Therefore, to increase the signal-to-noise ratio, we record images with the two opposite signs of current. Thereby, we recorded three sequences of images: one without current and two of opposite signs of currents, as seen in Figure 24.

The main characteristics of the imaging system used in these experiments are described in Table 1

Table 1 – Main characteristics the imaging system and the measured ODMR lines.

Parameter	Symbol	Value
Wavelength of laser	λ	532 nm
Laser power	P_{Laser}	20 mW
MW power	P_{MW}	25 dBm
MW step	Δ	1 MHz
Linewidth (ODMR spectrum)	w	7.5 MHz
Signal to noise (camera)	S/N	65 dB
Exposure time	T	85 ms
Microscope magnification	M	50x (NA 0.93)
Pixel size	px	0.7 μm

Source: By the author.

To improve the signal-to-noise (S/N), we can combine 2x2 pixels into a single pixel, this procedure is known as binning. This leads to a reduced resolution by the same factor of binning, but it also improves the S/N by the same factor. An example can be seen in Figure 25.

To reconstruct the external magnetic field, at each pixel, we applied multi-Lorentzian fits to the ODMR spectra to extract the eight resonance frequencies due to four orientations of the NV center (15, 56, 63):

$$f(\nu) = A\left[1 - \sum_{i}^{4} C_i \left(L\left(\frac{\nu - \overline{\nu}_i - D_i/2}{\Delta\nu_i}\right) + L\left(\frac{\nu - \overline{\nu}_i + D_i/2}{\Delta\nu_i}\right)\right)\right], \tag{5.2}$$

where the index i is due to the four orientations the NV center, $L(x) = 1/(1+x^2)$ is the Lorentzian function, C_i is the contrast (peak amplitude) of the line's pair, $\overline{\nu}_i = (\nu^i_+ + \nu^i_-)/2$ is the central position of the pair, $D_i = \nu^i_+ - \nu^i_-$ is the Zeeman distance between the two lines of the pair and $\Delta\nu_i$ is their linewidth. Besides, the frequencies $\nu^i_\pm$ satisfy the equation (5.3).

$$\nu^i_\pm = D_{GS} \pm \gamma_e B^i_{NV}, \tag{5.3}$$

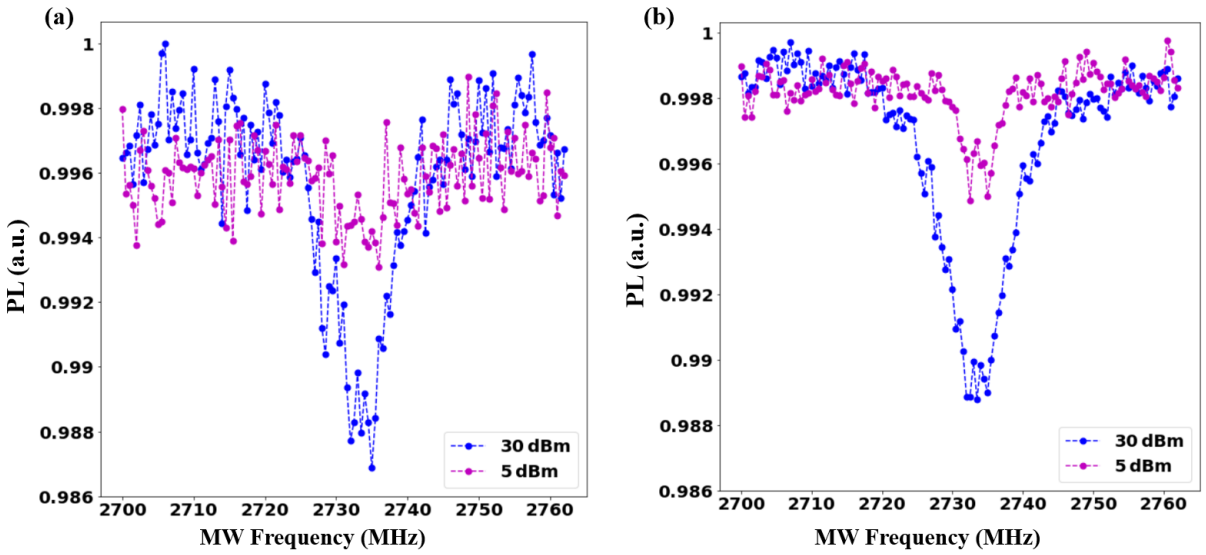

Figure 25 – a) Resonance peak in the ODMR spectrum of a single pixel the image before the binning for two set microwave power. b) Resonance peak after the binning.

Source: By the author.

where D_{GS} is the zero-field splitting.

As mentioned previously, the crystalline orientation of our sample is (100), so each axis x, y and z coincide with the edges of the plate. Let us consider $\hat{u}_1$, $\hat{u}_2$, $\hat{u}_3$ and $\hat{u}_4$ the unit vectors representing the four possible orientations of the NV axes. Due to the symmetry properties of the NV centers, we obtain

$$\hat{u}_1 + \hat{u}_2 + \hat{u}_3 + \hat{u}_4 = 0 \tag{5.4}$$

where

$$\hat{u}_1 = (\hat{i} + \hat{j} + \hat{k})/\sqrt{3}; \quad \hat{u}_2 = (-\hat{i} - \hat{j} + \hat{k})/\sqrt{3}$$

$$\hat{u}_3 = (\hat{i} - \hat{j} - \hat{k})/\sqrt{3}; \quad \hat{u}_4 = (-\hat{i} + \hat{j} - \hat{k})/\sqrt{3}. \tag{5.5}$$

If we consider that the external magnetic field is $\vec{B} = B_x\hat{i} + B_y\hat{j} + B_z\hat{k}$ in the lab frame, where z is perpendicular to the diamond surface. From the equation (5.4) we obtain an equation relating the module the magnetic field along the NV axis of the four possible orientations of the NV.

$$\vec{B}.\hat{u}_1 + \vec{B}.\hat{u}_2 + \vec{B}.\hat{u}_3 + \vec{B}.\hat{u}_4 = 0$$

$$B^1_{NV} + B^2_{NV} + B^3_{NV} + B^4_{NV} = 0 \tag{5.6}$$

From equations (5.3) and (5.6) we have a linear system of equations relating the vector components of $\vec{B}$, from which we use a least-square minimization algorithm (67) to obtain the best estimate for the vector components of $\vec{B}$, at each pixel.

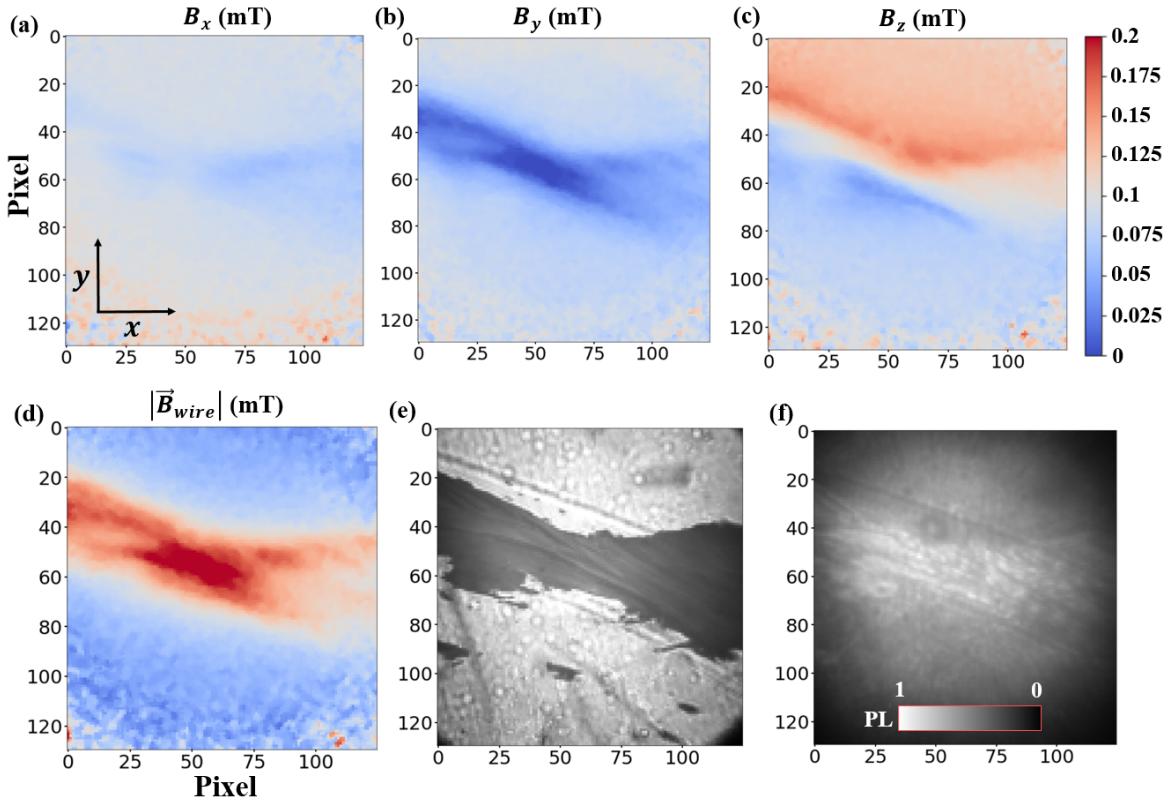

Figure 26 – (a), (b) and (c) Components of the magnetic field the wire under a current I=15 mA in the lab frame. (d) Module of the magnetic field produced by the sample in the laboratory frame. (e) Image of the sample. (f) PL image of the area under laser excitation. 1 pixel = 1.4 μm.

Source: By the author.

Figure 26 displays the reconstruction of a magnetic field produced by a current of 15 mA in the test wire, of 100 nm thickness. In this case, the magnetic field distribution is approximately known (limited by the imperfections of the wire, caused by the etching method), which allows us to determine the correct attribution of the ODMR peaks to each NV-axis direction. Is important to note that, once the external magnetic bias field is measured, it could be used to retrieve the current density (field-source) distributions for other samples.

Considering an idealized homogeneous ultra-thin wire, with width W and carrying a current I, we can use the Biot-Savart law to determine an analytic expression for the magnetic field. For convenience, we consider a new reference frame (x_1, y_1, z_1), where x_1 is parallel to the wire, y_1 is perpendicular, z_1 is perpendicular to the surface, the wire and the current of total intensity I flowing along the $+x_1$ direction, as seen in Figure 27(a), thus the field components are given by

$$B_{x_1}(y_1, z_{NV}) = 0$$

$$B_{y_1}(y_1, z_{NV}) = -\frac{\mu_0 I}{2\pi W}\left(\tan^{-1}\left[\frac{W-2(y_1-y_0)}{2\,z_{NV}}\right]+\tan^{-1}\left[\frac{W+2(y_1-y_0)}{2\,z_{NV}}\right]\right) \tag{5.7}$$

$$B_{z_1}(y_1, z_{NV}) = \frac{\mu_0 I}{4\pi W}\ln\left[\frac{(W+2(y_1-y_0)^2)+4\,z_{NV}^2}{(W-2(y_1-y_0)^2)+4\,z_{NV}^2}\right]$$

where the z_{NV} corresponds to distance between the wire and the NV plane and y_0 is the position of the wire in the y-axis.

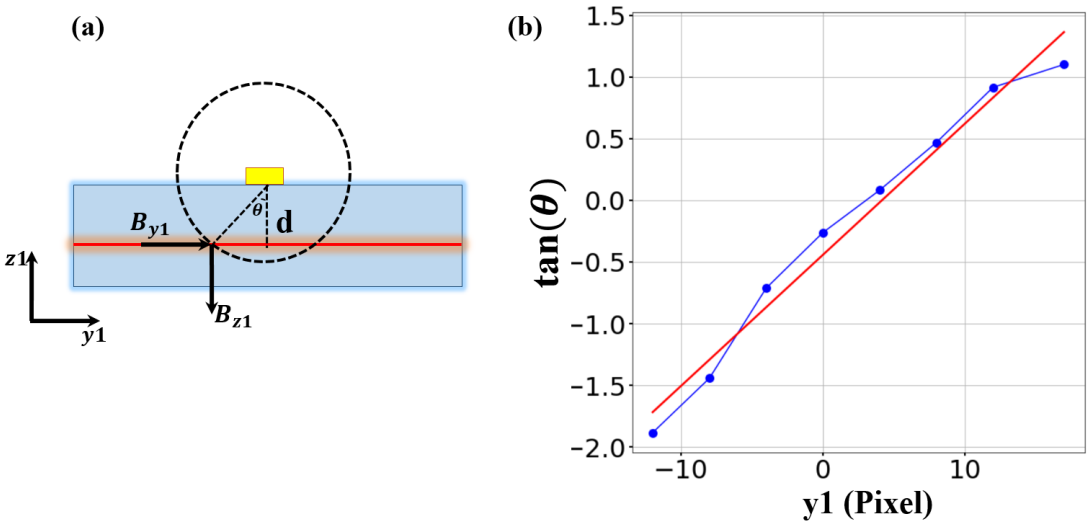

Figure 27 – a) Representation of the magnetic field produced of the ideal wire on the NV plane (red line). θ is the angle between a magnetic field $\vec{B}$ and the NV plane. b) $\tan(\theta)$ in function the y_1-axis along the black line perpendicular to the wire. 1 pixel = 1.4 μm. The connected blue dots correspond to experimental data points, determined from the magnetic image.

Source: By the author.

Figure 28 shows the profiles of those components along the black line, perpendicular to the wire, for several distances $z_{NV} = \{0.5, 1, 5, 10\}\,\mu$m, for a wire of width $W = 24\,\mu$m and carrying a current of $I = 10$ mA. Being the value of $z_{NV} = 10 \pm 2\,\mu$m the distance that best adjusts to data. Note that the sharp peaks in B_z and edges of B_x and B_y, seem to consistently support this much larger value of z_{NV}, than originally planned, which results in limited spatial resolution.

From Figure 27(a) we can obtain a relation between the components B_{y1} and B_{z_1}, along the y_1-axis, doing some geometric considerations, we obtain the following relation

$$\tan(\theta) = \frac{B_z}{B_y} = \frac{y_1 - y_0}{z_{NV}}. \tag{5.8}$$

Fitting the data along the black line, with equation 3, and taking into account the effective size of the pixel, we can extract the values $y_0 = 81.03\,\mu$m and $z_{NV} = 14.5\,\mu$m.

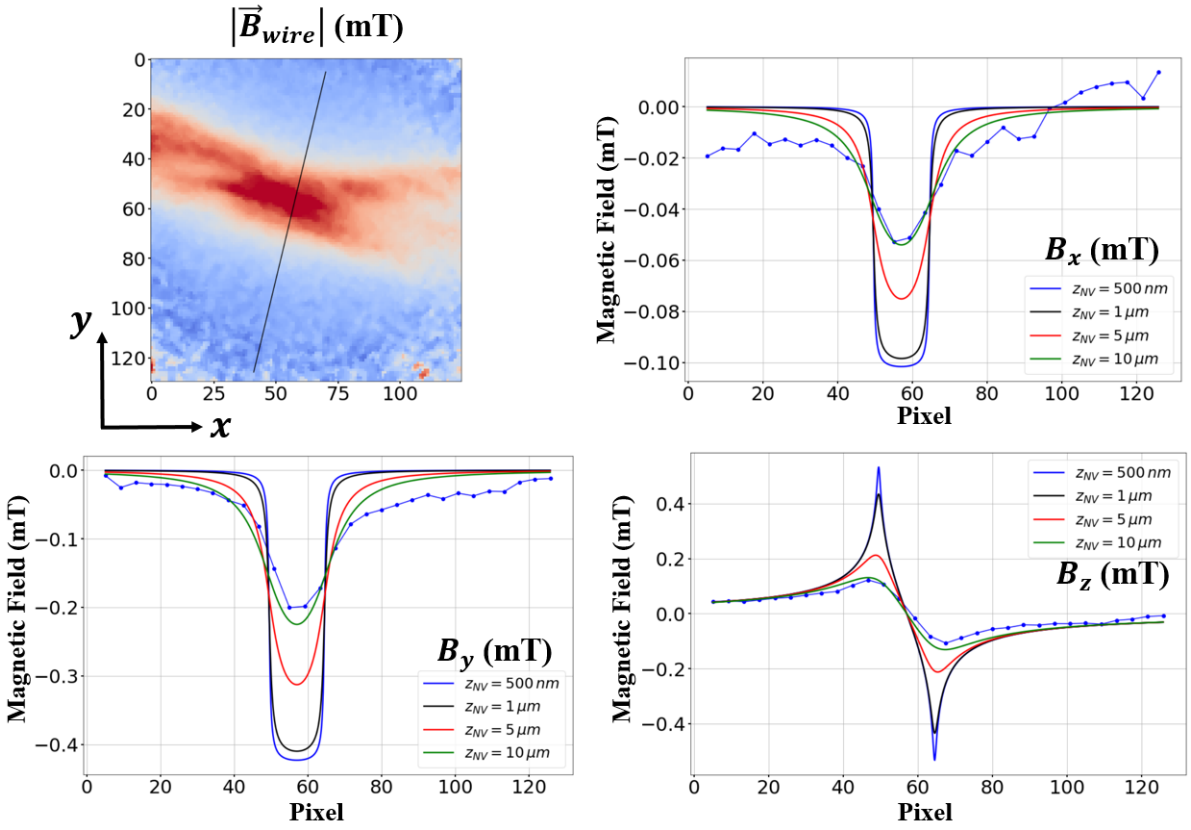

Figure 28 – Components B_x, B_y and B_z of the magnetic field created by a current $I = 15$ mA in the wire of width $W = 24\,\mu$m for various probe distance z_{NV} along the black line perpendicular to the wire, using the equations (5.7). 1 pixel = 1.4 μm. The connected blue dots correspond to experimental data points, determined from the magnetic images.

Source: By the author.

From table 1 and equation (3.12), we obtain a sensitivity of $\eta = 6\,\mu$T μm Hz$^{-1/2}$ in one pixel. This value is particularly due to the contrast and the linewidth that we obtain, we measure contrasts in the range of 0.3% to 0.6% per pixel. These values are much lower than those found in the literature (about 1%). (15, 63, 68) This is largely due to the power of the laser, 20 mW reaching the objective, high power is needed to excite a large diamond surface. In addition, we find that the distance between the layer of NV and the wire is around $\sim 12\,\mu$m. This partially justifies the reason why we fail to detect magnetic fields of currents less than 3 mA, see Figure 29.

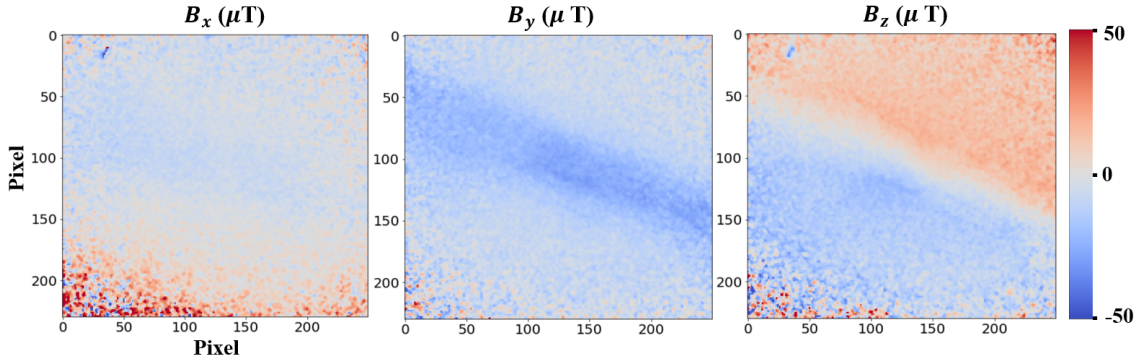

Figure 29 – Components B_x, B_y and B_z of the magnetic field created by a current $I = 3$ mA in the wire. 1 pixel = 0.7 μm.

Source: By the author.

5.4 Current density reconstruction

Now we discuss how to obtain the current distribution by measuring its magnetic field. (15, 69) The method assumes that the current is confined to a 2D plane, meaning that the sample has to be flat. In our case, for example, we chose a thickness of 100 nm for the test wire, with a width of around 10 μm. This leads to a distribution $\vec{J}(x, y)$ expressed in units of amperes per meter (A/m), that can be calculated by inverting the Biot-Savart law, as described by Roth et al. (69), and summarized in Figure 30.

If the magnetic field vector $\vec{B}$ at a given point in the space is related to the current distribution $\vec{J}(\vec{r})$ through the Biot Savart law

$$\vec{B}(\vec{r}) = \frac{\mu_0}{4\pi} \int \frac{\vec{J}(\vec{r'}) \times (\vec{r} - \vec{r'})}{|\vec{r} - \vec{r'}|^3} d^3\vec{r'} \tag{5.9}$$

where μ_0 is the permeability of the free space and the integral is over the whole space (where $\vec{J}(\vec{r})$ not negligible). We can also express this as a function the magnetic vector potential $\vec{A}$, through

$$\vec{B} = \vec{\nabla} \times \vec{A} \tag{5.10}$$

Using Maxwell's equations in the Lorentz gauge, the magnetic vector potential is given by

$$\vec{A}(\vec{r}) = \frac{\mu_0}{4\pi} \int \frac{\vec{J}(\vec{r'})}{|\vec{r} - \vec{r'}|} d^3\vec{r'}. \tag{5.11}$$

Now, defining the Green's function

$$G(\vec{r}, \vec{r'}) = \frac{1}{|\vec{r} - \vec{r'}|} = \frac{1}{2\pi^2} \int \frac{e^{i\vec{k}(\vec{r} - \vec{r'})}}{\vec{k}^2} d^3\vec{k}, \tag{5.12}$$

the magnetic field can be written as

$$\vec{B}(\vec{r}) = \frac{\mu_0}{8\pi^3} \nabla \times \int \int \vec{J}(\vec{r'}) \frac{e^{i\vec{k}(\vec{r} - \vec{r'})}}{\vec{k}^2} d^3\vec{k}\, d^3\vec{r'}$$

$$\vec{B}(\vec{r}) = \frac{-i\,\mu_0}{8\pi^3} \int\int \vec{J}(\vec{r'}) \times \vec{k}\; \frac{e^{i\vec{k}(\vec{r}-\vec{r'})}}{\vec{k}^2}\, d^3\vec{k}\, d^3\vec{r'}. \tag{5.13}$$

Considering that the current distribution is in x-y plane, the Fourier transform of $\vec{J}(\vec{r'})$ and $\vec{B}(\vec{r})$ are

$$b_n(k_x, k_y, z_0) = \frac{1}{2\pi} \int_{-\infty}^{+\infty} B_n(x, y, z_0)\, \mathrm{e}^{i(k_x x + k_y y)} dx\, dy \quad n = x, y \text{ and } z \tag{5.14}$$

$$j_m(k_x, k_y) = \frac{1}{2\pi} \int_{-\infty}^{+\infty} J_m(x, y)\, \mathrm{e}^{i(k_x x + k_y y)} dx\, dy \quad m = x \text{ and } y \tag{5.15}$$

where k_x and k_y are the components of the spatial frequency $\vec{k}$.

The equations (5.13), (5.4) and (5.15), relate the magnetic field and density current to their the spatial frequency in Fourier space, where each component is related by

$$b_x(k_x, k_y, z_0) = \frac{\mu_0}{2} \mathrm{e}^{-z_0\sqrt{k_x^2+k_y^2}}\, j_y(k_x, k_y), \tag{5.16a}$$

$$b_y(k_x, k_y, z_0) = -\frac{\mu_0}{2} \mathrm{e}^{-z_0\sqrt{k_x^2+k_y^2}}\, j_x(k_x, k_y), \tag{5.16b}$$

$$b_z(k_x, k_y, z_0) = i\frac{\mu_0}{2} \mathrm{e}^{-z_0\sqrt{k_x^2+k_y^2}} \left[\frac{k_y}{\sqrt{k_x^2+k_y^2}}\, j_x(k_x, k_y) - \frac{k_x}{\sqrt{k_x^2+k_y^2}}\, j_y(k_x, k_y) \right], \tag{5.16c}$$

We assume that the current is quasi-static, so the current density obeys the equation of continuity

$$\bigtriangledown \cdot \vec{J} = 0, \tag{5.17}$$

which in Fourier space becomes

$$k_x\, j_x(k_x, k_y) + k_y\, j_y(k_x, k_y) = 0 \tag{5.18}$$

Thus, for each spatial frequency (k_x, k_y) we have a set of four equations, given by Eqs. (5.16) and (5.18), to be solved. This represents an over-determined linear system, that can easily be solved with a least-square minimization algorithm, to find the best estimate of the variables $j_x(k_x, k_y)$ and $j_y(k_x, k_y)$. After determining $j_x(k_x, k_y)$ and $j_y(k_x, k_y)$, we use the inverse Fourier transform to obtain the current density in the real space

$$J_m(x, y) = \frac{1}{2\pi} \int_{-\infty}^{+\infty} j_m(x, y)\, \mathrm{e}^{-i(k_x x + k_y y)}\, dk_x\, dk_y \quad m = x \text{ and } y \tag{5.19}$$

Figure 31 shows the calculated components of the current density in a section of the test (DC circuit) wire, obtained following these steps and using the measurements of vector field $\vec{B}(\vec{r})$ at the NV-sensor plane. The figure also shows the vector lines of $\vec{J}$, superposed to its magnitude map, as well as a direct (bright field) microscopy image of the same portion of the test wire.

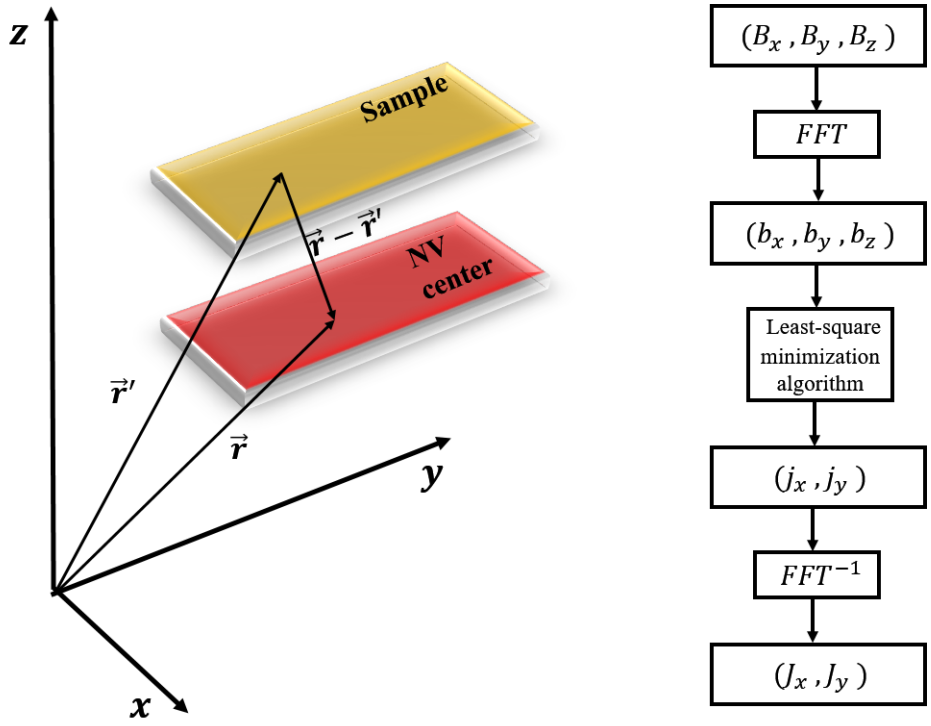

Figure 30 – (left) Representation of a sample with some planar current density $\vec{J}$, producing a magnetic field $\vec{B}$ at the NV-sensor plane. (right) Schematic diagram summarizing how to obtain the current density from the measured magnetic field.

Source: By the author.

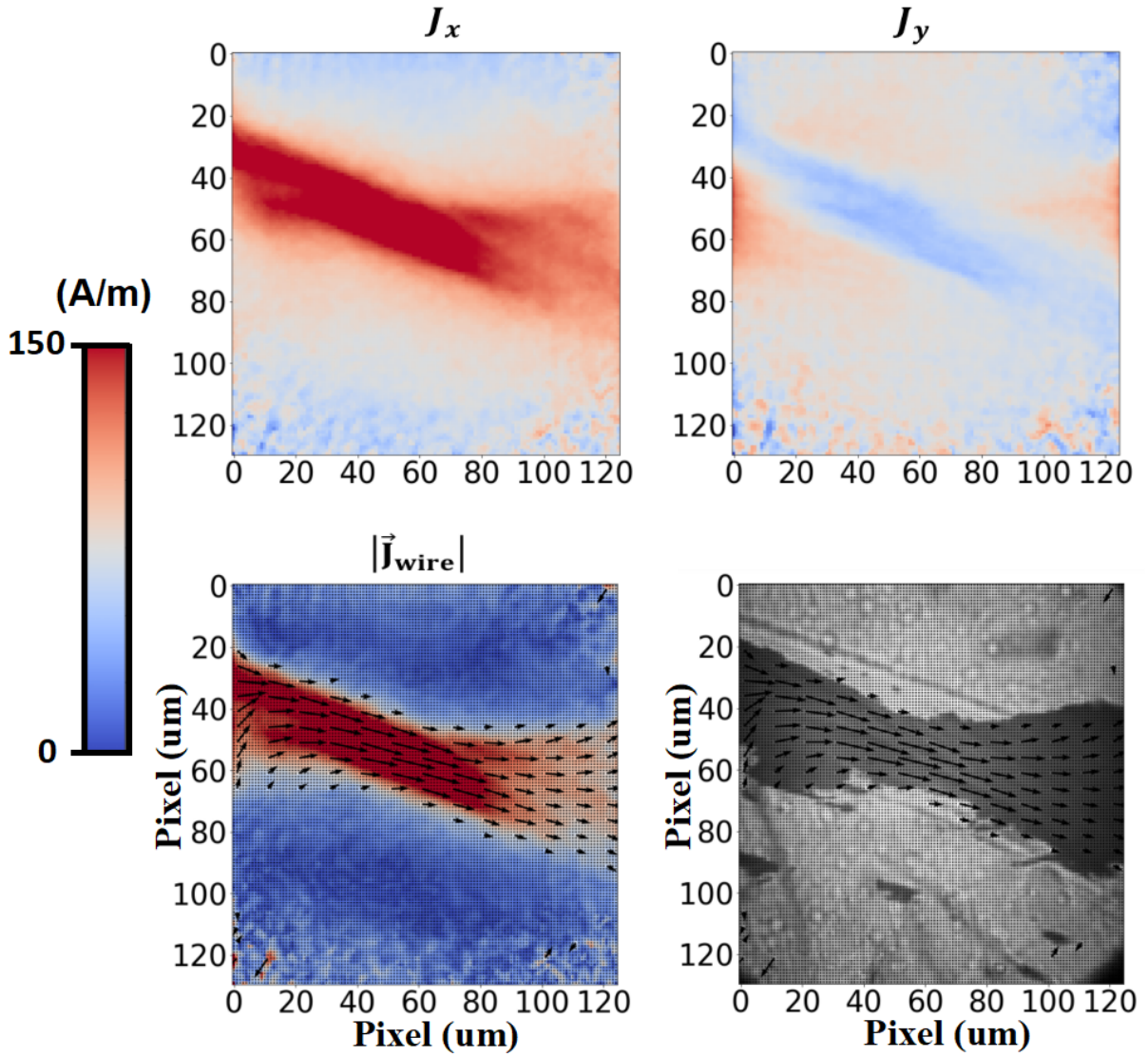

Figure 31 – Components of the current density in the probe wire for I=15 mA in the lab frame. The probe distance is assumed to be $z_0 = 100$ nm. 1 pixel = 0.7μ m

Source: By the author.

6 SPIN COHERENCE MEASUREMENTS

6.1 Introduction

Coherence properties of NV spin have been one of the most intensively studied topics in NV-related research, because of their many applications. In general, spin coherence of a NV center is affected by several factors, such as proximal electronic and nuclear spins (^{13}C, ^{14}N or ^{15}N), fluctuations in the external magnetic field, and temperature. These may lead to a homogeneous and inhomogeneous broadening of the transitions. When the time scale is relatively long compared to the experimental pulse sequence, some of these effects can be considered quasi-static sources of decoherence.
In summary, the three main characteristic time scales are:

- T_1: the population decay (longitudinal or spin-lattice relaxation) time, resulting from Raman interaction with lattice phonons at room temperature. For NV centers in bulk diamond at room temperature, T_1 is typical of order $\sim 1-10$ ms; however, since spin-lattice relaxation is a phononic process, T_1 is quite sensitive to temperature.

- T_2: the characteristic time for homogeneous spin dephasing (whereas T_2^* is the characteristic time in the presence of inhomogeneities), more commonly referred to as spin decoherence, T_2 is intrinsic to the NV center and its local spin environment and is often referred to as spin-spin relaxation in conventional NMR nomenclature. The NV spin coherence time T_2 is typically measured using Electron Spin Echo Envelope Modulation (ESEEM) of two pulses also known as Hahn echo pulse sequence.

- T_2^*: the spin-spin decoherence time, resulting from the interaction between the electron spin and adjacent nuclear-spin bath, from ^{13}C or an additional N (either ^{14}N or ^{15}N) atom. These nuclear spins create a fluctuating nonzero magnetic field, that interacts with the electron spin of the NV, leading to decoherence. The spin coherence time defines how long the spin is coherent enough to perform spin manipulations. One method to measure T_2^* is to apply a Ramsey pulse sequence and extract the characteristic time of the free induction decay (FID) curve.

As the spin-lattice decoherence takes place on a much longer time scale we are only limited by the spin-spin decoherence time ($T_1 >> T_2 >> T_2^*$).

6.2 Rabi Oscillations

We consider a two-state system initially prepared in the lower state, then subjected to a resonant external oscillating field. This coupling induces transitions between the two

states, usually referred to as Rabi oscillations. We probed the Rabi oscillations in our system between the $|m_s = 0\rangle$ and one of the $|m_s = \pm 1\rangle$ levels, that is separated by an external magnetic field.

Population transfer between the two states causes changes in the fluorescence, which we use as our signal, captured in a CCD camera. In the experiment, we drive transitions between states $|0\rangle$ and $|\pm 1\rangle$, depending on the set frequency, with a resonant microwave pulse of varying duration, while measuring the population remaining population in state $|0\rangle$. Figure 32 shows a typical Rabi signal.

The interaction of a microwave field B_{MW} with the NV center, at frequency ω_{MW}, is described by

$$H_{MW} = \gamma_e \, B_{MW} \, S_x \cos(\omega_{MW} t) \tag{6.1}$$

and the complete Hamiltonian, in the S_z basis, may be represented as

$$H = D \, S_z^2 + \gamma_e B_z \, S_z + \gamma_e \, B_{MW} \, S_x \cos(\omega_{MW} t) \tag{6.2}$$

$$H = \begin{bmatrix} D + \gamma_e B_z & \frac{1}{\sqrt{2}}\cos(\omega_{MW} t)\gamma_e B_{MW} & 0 \\ \frac{1}{\sqrt{2}}\cos(\omega_{MW} t)\gamma_e B_{MW} & 0 & \frac{1}{\sqrt{2}}\cos(\omega_{MW} t)\gamma_e B_{MW} \\ 0 & \frac{1}{\sqrt{2}}\cos(\omega_{MW} t)\gamma_e B_{MW} & D - \gamma_e B_z \end{bmatrix}. \tag{6.3}$$

The transformation of the Hamiltonian from the laboratory to the rotating frame ($U = e^{-i\omega_{MW} t S_z}$) is

$$H^{rot} = U \, H \, U^\dagger + i\dot{U}U^\dagger = \begin{bmatrix} D + \gamma_e B_z - \omega_{MW} & \frac{1}{2\sqrt{2}}\gamma_e B_{MW} & 0 \\ \frac{1}{2\sqrt{2}}\gamma_e B_{MW} & 0 & \frac{1}{2\sqrt{2}}\gamma_e B_{MW} \\ 0 & \frac{1}{2\sqrt{2}}\gamma_e B_{MW} & D - \gamma_e B_z - \omega_{MW} \end{bmatrix}. \tag{6.4}$$

To drive the transition $|0\rangle \leftrightarrow |1\rangle$, the first and second main diagonal entry have to be zero, so $D \pm \gamma_e \, B_z \pm \omega_{MW} = 0$, giving the resonance condition. As seen in the Figure 32, for different lengths in t, the NV center experiences coherent population transfer between the two states. The fluorescence signal S, acquired at the end of the pulse sequence, corresponds to a projection of the state vector onto the $|0\rangle$ eigenstate, therefore $S \propto |\langle \Psi | \, 0\rangle|$. The probability to find the system in this state at time t is

$$S(t) \propto \left(\frac{\gamma_e \, B_{MW}}{\Omega_R}\right)^2 \text{sen}^2\left(\frac{\Omega_R t}{2}\right), \tag{6.5}$$

where $\Omega_R = \sqrt{(\gamma_e \, B_{MW})^2 + \Delta^2}$ is the generalized Rabi frequency, and $\Delta = \omega_{MW} - \omega_0$ describes the detuning of the driving frequency ω_{MW} to the actual transition frequency $\omega_0 = D \pm \gamma_e \, B_z$, between $|0\rangle$ and $|+1\rangle$ (or $|0\rangle$ and $|-1\rangle$). The decay of the amplitude of

the Rabi oscillations (seen in Figure 32) is determined by the ensemble coherence time T_2^*. Therefore

$$S(t) \propto e^{-t/T_2^*} \left(\frac{\gamma_e B_{MW}}{\Omega_R} \right)^2 \text{sen}^2 \left(\frac{\Omega_R t}{2} \right) \tag{6.6}$$

Monitoring the Rabi oscillations may provide us with information regarding the coherence of our system, and the actual interaction of the NV centers with the microwave field. So, the π-pulse is defined as the MW pulse duration that gives the first minimum of fluorescence, corresponding to complete population transfer ($|0\rangle \rightarrow |-1\rangle$ spin flip).

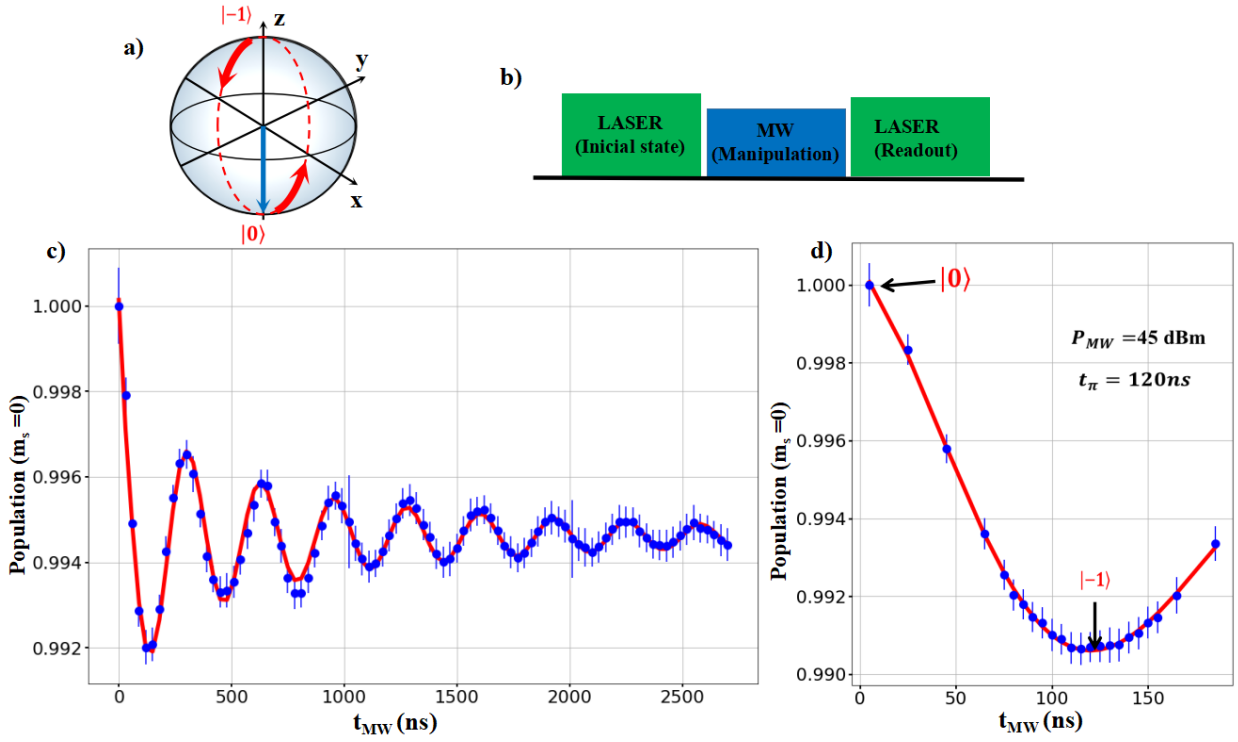

Figure 32 – a) Two level system ($|0\rangle \rightarrow |-1\rangle$) and its geometrical representation in the Bloch sphere. b) Rabi sequence. c) Experimental (solid circles) and theoretical (solid line) of Rabi oscillations at room temperature between the $|0\rangle$ and $|-1\rangle$ levels. d) For a value of MW power, the π-pulse is defined as the MW pulse duration that gives the first minimum of fluorescence, corresponding to complete population transfer.

Source: By the author.

6.3 Ramsey Interferometry

The detuning $\Delta\omega = |\omega_{MW} - \omega_{NV}|$ between the excitation field and the spin level splitting can be measured with the Ramsey sequence, shown in Figure 33. It creates a superposition state of the NV center, which subsequently free evolves by a time τ and then the population of the state $m_s = 0$ is measured.. Experimentally, this is realized by first initializing the spin to the $|0\rangle$ ground state, via optical pumping, and turning off the laser excitation during the MW driving. Once initialized in the ground state, the spin is

then rotated by a $\pi/2$-pulse onto the y axis, to prepare a superposition state. After that, we allow the system to freely evolve for a duration of τ. The last $\pi/2$ pulse is to convert the coherence into population difference which can be optically detected. The expression describing Ramsey oscillation is (70, 71)

$$S(t) = A + B\, e^{-t/T_2^*} \sum_i \cos\left[2\pi(f_{MW} - f_{NV}^i)t\right] \tag{6.7}$$

Ramsey interferometry follows the method of separated oscillatory fields and is traditionally used to sense a time-independent, or DC magnetic field. (59, 72, 73)

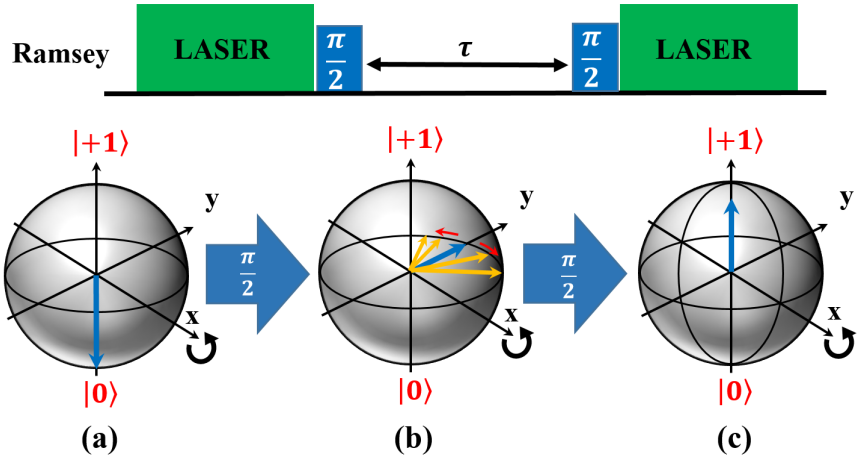

Figure 33 – Top: Ramsey sequence. Upper: the formation of a spin echo by means of a $\pi/2-\tau-\pi/2$ pulse sequence viewed in the rotating reference frame.

Source: By the author.

6.4 Electron Spin Echo Envelope Modulation (ESEEM)

Electron Spin Echo Envelope Modulation (ESEEM) is an important technique for measuring the hyperfine interaction parameters between electron spins and nearby nuclear spins. (40, 74–77) This interaction causes a periodic oscillation in the echo height superimposed on the normal echo decay. If we subtract the decay of the spin echo and Fourier transform the oscillations, we get the splittings due to the nuclei. ESEEM is suited for measuring weak hyperfine couplings of the order of the free nuclear Larmor frequency. The theoretical treatment of the nuclear modulation effect is based on the spin density operator formalism (see Appendix A).The two most common forms of ESEEM experiments use either a two pulse ($\pi/2 - \tau - \pi - \tau - \pi/2$) (typical Hahn Echo sequence) or three pulse ($\pi/2 - \tau - \pi/2 - T - \pi/2\tau - \pi/2$) sequences.

6.4.1 Hahn Echo and the Two-pulse ESEEM

One of the most popular sequence in Electron Paramagnetic Resonance (EPR) for measuring the nuclear modulation effect is the Hahn echo sequence $\pi/2 - \tau - \pi - \tau - \pi/2$ (40), shown in Figure 34. This sequence is an extension on the Ramsey pulse sequence after the NV spin is prepared in a coherent superposition with the first $\pi/2$ pulse, the spin system is allowed to freely precess by time τ. During this period of time, the spin system loses some coherence (dephasing), due to interactions with its magnetic environment, causing some spins to slow down (due to lower local field strength) while others to speed up (in higher field strengths), and this produces a distribution of spin phases, as depicted in Figure 34b. This effect leads to a decay in the amplitude of the signal, as function of time.

If the local magnetic field fluctuations are slow on the time scale of the free precession interval τ, the MW π pulse inverts the accumulated phase such that the same amount of phase is accumulated over the second free precession interval τ, thus refocusing the net phase and ideally eliminating the net phase shift. The efficacy of the refocusing depends on how slow the magnetic field fluctuations are compared to the free precession interval; faster fluctuations result in a less perfect refocusing. The final $\pi/2$ pulse projects the NV center spin back into the basis where spin-dependent photoluminescence readout can be performed; thus coherence is mapped onto a population difference between the states $|0\rangle$ and $|1\rangle$.

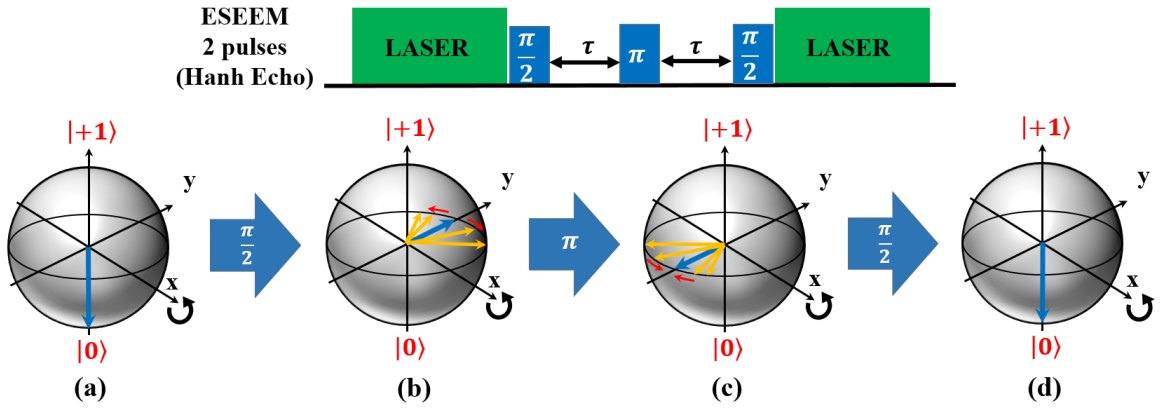

Figure 34 – The magnetization vector is initially oriented along the z-axis (a). A $\pi/2$ pulse along x will rotate the magnetization to the y axis (b). During time τ between the first and second pulse, the different spin packets freely evolve (dephasing of the different spin packets). The π pulse inverts the y component of the individual magnetization vectors (c). After a time tau, the magnetization vectors are in phase along the y axis and a primary echo is observed (d).

Source: By the author.

Varying the free precession time τ one can observe the decay of the echo amplitude

curve, which allows one to extract a damping constant, by fitting the data to an exponential decay with the function (76)

$$S(\tau) = e^{-(2\tau/T_2)^n}\,[1 - 0.25\,k\,(2 - 2\cos(\mathbf{2}\pi\,\mathbf{f_1}\tau) - 2\cos(\mathbf{2}\pi\,\mathbf{f_2}\tau) + \cos(\mathbf{2}\pi\,(\mathbf{f_1} + \mathbf{f_2})\tau) + \cos(\mathbf{2}\pi\,(\mathbf{f_1} - \mathbf{f_2})\tau))] \tag{6.8}$$

where the contrast k depends on the external magnetic field vector, f_1, f_2 are the frequency of the nuclear transitions (see Appendix A), T_2 is the spin coherence time and n is the power index which is dependent on the decoherence mechanisms. (76, 78)

With the two-pulse ESEEM (Hahn echo sequence) is possible to get the nuclear frequencies using EPR measurements. The two-pulse modulation formula shows that not only the primary nuclear transition frequencies is observed, but it also peaks at the sum and difference frequencies. Analyzing the positions of these frequencies can be very useful in interpreting properties of the material (especially in disordered systems), and is one of the applications of the two-pulse ESEEM spectra in EPR studies.

6.4.2 Three pulse ESSEM

Similarly to 2-pulse ESEEM, an envelope modulation of the stimulated echo can be observed using a different sequence, if time T between the second and the third pulse is increased while the time between the first and second pulses is kept constant. Figure 35 shows a representation of this sequence.

Considering an electron spin ($S = 1/2$) system coupled to a nuclear spin with $I = 1/2$, in a constant magnetic field, the modulation part of the echo signal is given by (see Appendix A, for details on the derivation)

$$S(\tau, T) = e^{-\tau/T_1}\left[\frac{1}{2} - \frac{k}{8}(1 - \cos(\mathbf{2}\pi\mathbf{f_1}\tau))(1 - \cos(\mathbf{2}\pi\mathbf{f_2}(\tau + \mathbf{T}))) + \frac{k}{8}(1 - \cos(\mathbf{2}\pi\mathbf{f_2}\tau))(1 - \cos(\mathbf{2}\pi\mathbf{f_1}(\tau + \mathbf{T})))\right] \tag{6.9}$$

In contrast to the two-pulse ESEEM experiment, the three-pulse ESEEM spectra are free from the sum and difference frequencies. The resolution is limited by the electron spin-lattice relaxation time (T_1), which is usually much larger than the electronic spin-spin lattice relaxation time T_2. A feature of the three-pulse ESEEM sequence results as consequence of the factor $(1 - \cos(\mathbf{2}\pi\mathbf{f_{1,2}}\tau))$, in the equation (6.9), where the modulation vanishes at nuclear frequencies with a period of $\mathbf{f_{1,2}} = \mathbf{n}/\tau$. This leads to so-called blind spots in the spectrum where the nuclear frequencies are efficiently suppressed.

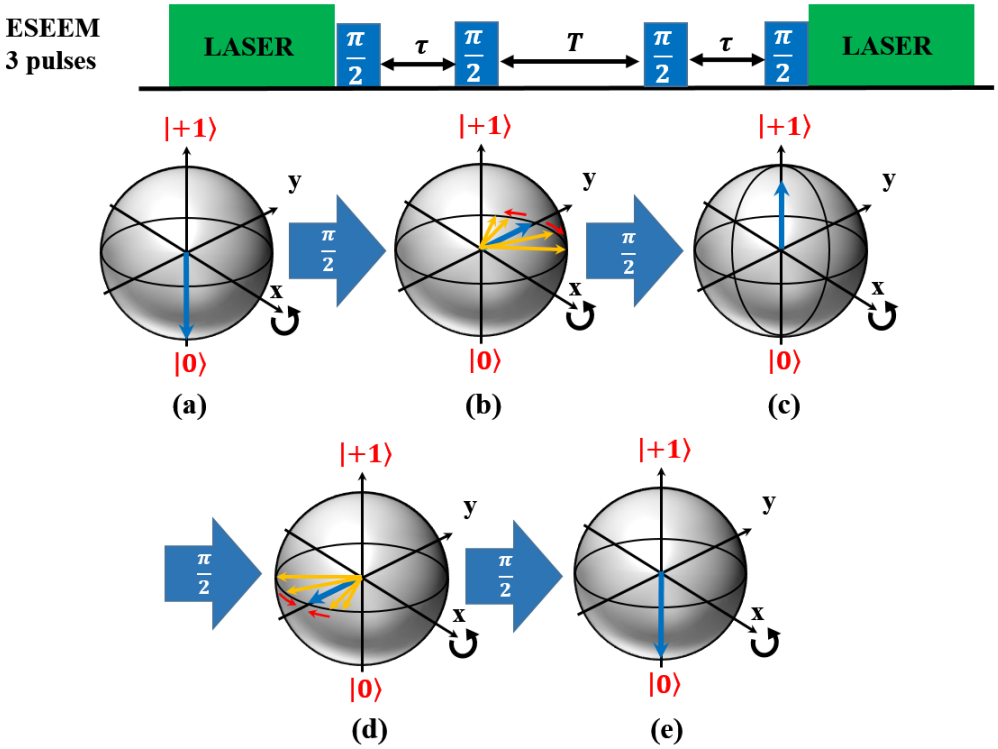

Figure 35 – The three-pulse sequence, $\pi/2-\tau-\pi/2-T-\pi/2-\tau-\pi/2$ creates a stimulated echo at time τ after the third $\pi/2$ pulse. The equilibrium z-magnetization (a) is transferred to transverse magnetization by the first $\pi/2$ pulse (b). During free evolution of length τ, the magnetization dephases (b). The second $\pi/2$ pulse rotates the magnetization vectors into the xz plane (c). During time T, the transverse magnetization decays (c). At time $t = T + \tau$, the third $\pi/2$ pulse transfers the z-magnetization pattern again to transverse magnetization (d), which forms an echo at time $t = T + 2\tau$ along the $+y$-axis. Note that the fourth $\pi/2$ pulse is used to read the magnetization.

Source: By the author.

6.5 Experimental Procedure

We used the technique of ODMR (under a magnetic field ~ 74.5 G) to determine the resonances of the different $\Delta m_s = \pm 1$ transitions. For these experiments, we chose the $|0\rangle \leftrightarrow |1\rangle$ transition at frequency is $f = 2980.5$ MHz, because of the best contrast among other peaks.

It is interesting to point out that the actual measurement was performed with a CCD camera (PointGrey, FL3-FW-03S1M-C), instead of the usual PMT (or APD) as normally found in the literature. We decided to do that because of the higher quantum efficiency of the sensor. To achieve this, we had to devise an appropriate imaging protocol to allow sufficient illumination and image capture in the camera, while still using extremely short pulse times in the MW sequences.

Figure 37 summarizes the protocol, where we encode an array of pulse sequences

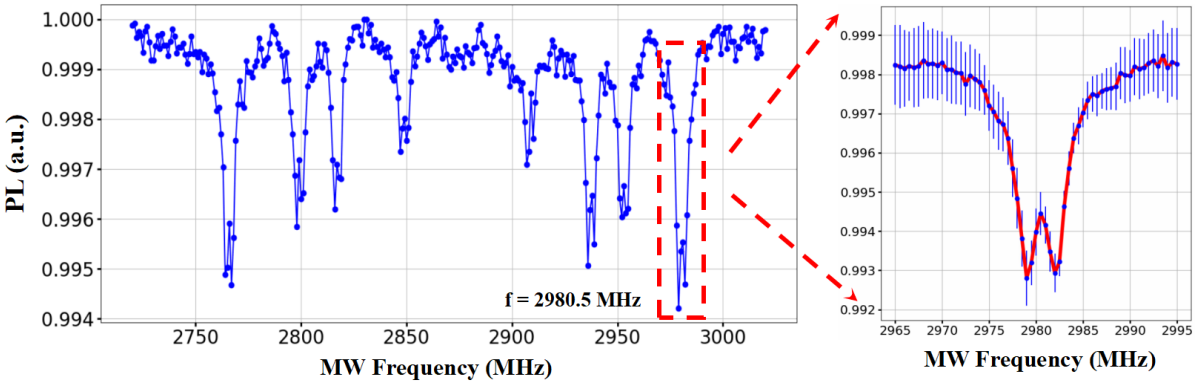

Figure 36 – The 16 resonances correspond to the different $|\Delta m_s| = 1$ transitions, four different NV orientations, and two different ^{15}N hyperfine transitions.

Source: By the author.

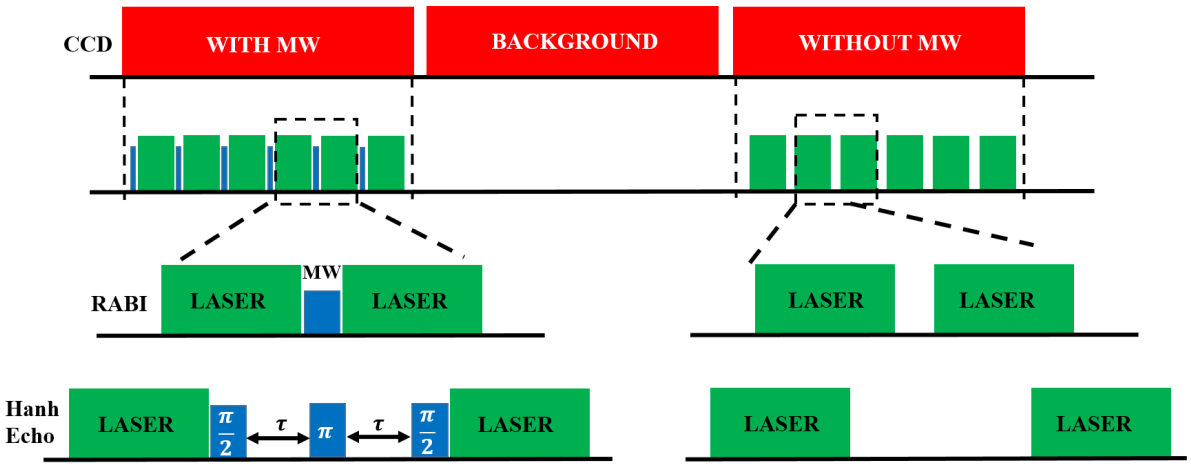

Figure 37 – Control pulse sequence of the experimental system.

Source: By the author.

into a low-frequency envelope (whose time is determined by the exposure time of CCD camera), as is schematically shown in the figure. Three types of sequences allow capturing three images, corresponding to the fluorescence in presence or absence of the MW, as well as a background image, for proper normalization of the fluorescence signal. Each type of pulse sequence (Rabi, Hanh echo, Ramsey, etc.) can be implemented in this protocol, just by encoding them in a block with MW-field turned on.

All pulses are generated from the SpinCore plugin board, using less than four signal lines. In essence, our protocols takes three images (seen in Figure 37): the first one is an image of the fluorescence with MW (this contains the changes due to the MW-pulse sequences), the second image is the light background (mostly environmental lights and scattered light from the laser), and the third image is the fluorescence without MW (as

a reference for the normalization). We subtract the background image from the other two, and divide both fluorescence image, to get the information to any pulse sequence we design, as seen in Figure 38.

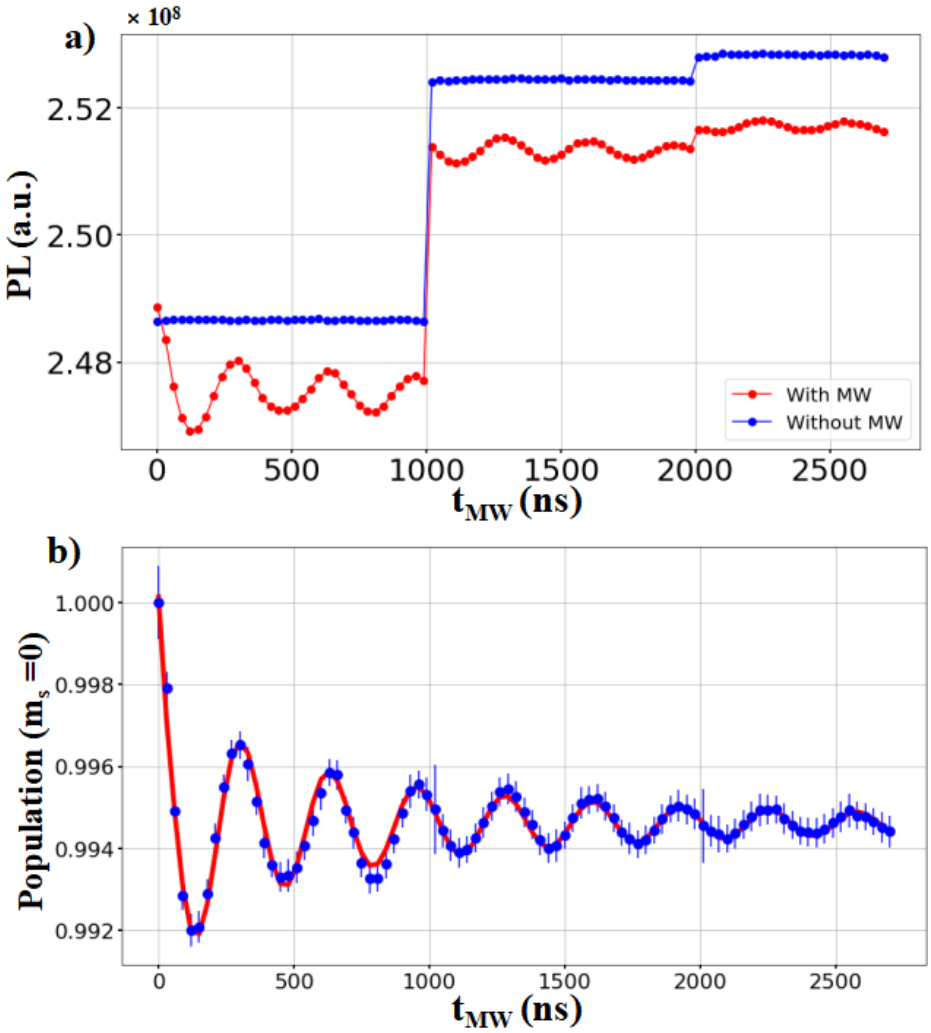

Figure 38 – a) Photoluminescence with MW and without MW. b) Population of the state ms=0 obtained dividing the photoluminescence with MW and without MW.

Source: By the author.

In Figure 38 we showed an example of a Rabi sequence, where we observed the photoluminescence with MW and without MW, the all sequence was obtained in three parts to know if the procedure is independent of the small variations of the laser power (around of 0.5%). Note that the change the photoluminescence is less than 1%.

6.6 Experimental Results

Now we show some of the results we obtain applying this technique to the pulse sequences discussed above: Rabi, Ramsey, and ESEEM (Hahn echo). Besides providing

relevant information about our sample, these methods are key measurements techniques that can be used in magnetometry and other quantum measurement applications. (7,45,79)

To implement these measurements, we developed the instrumentation and know-how on acquiring and processing thousands of images, analyzing a substantial amount of information (several GB of digital data), usually using customized scripts to process the data automatically computationally. This knowledge is useful for future applications, using more advanced measurements strategies, as this research goes further.

From the results presented here, one set is particularly interesting, as it was not anticipated when we started. These are the results relative to the ESSEM measurements, constituting something we rediscovered in NV-ensemble while trying to measure T_2, using a regular Hahn echo sequence.

6.6.1 Rabi sequence

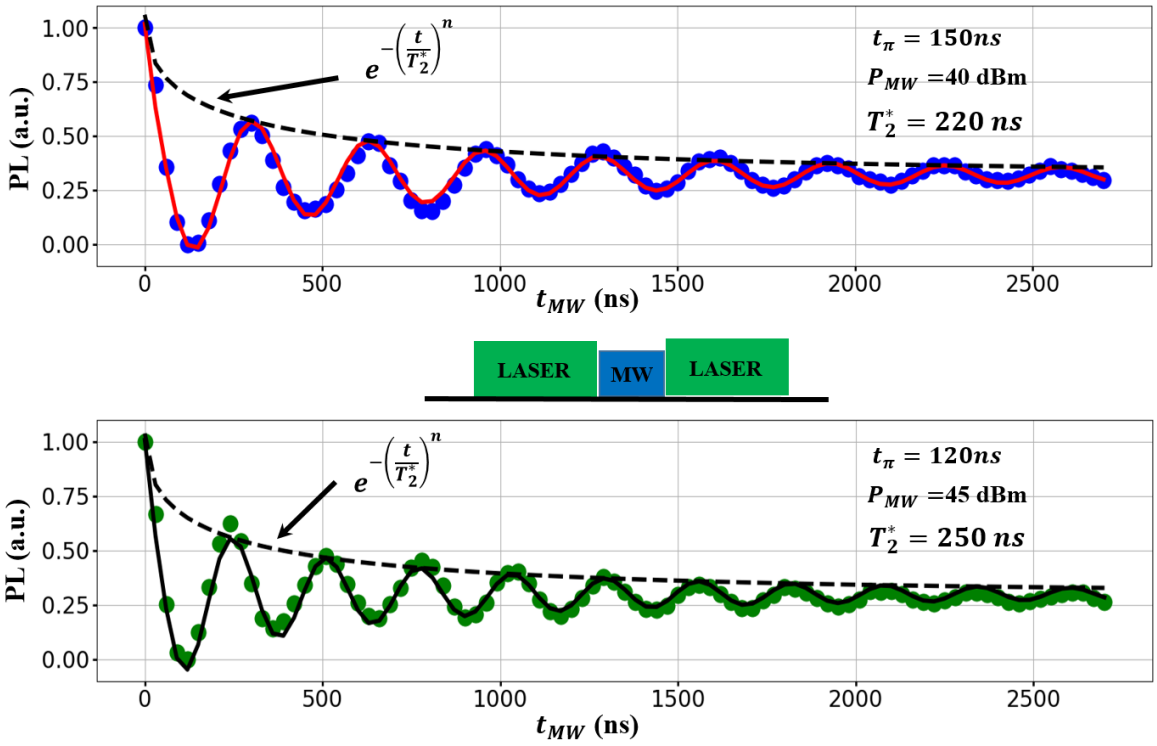

Figure 39 – Rabi oscillations observed using a CCD camera and the technique described in section 6.5. The blue and green dots are the experimental data for MW power at 40 dBm and 45 dBm, respectively, and the red and black lines are fits to these data. The dashed lines are the exponential envelops (as expressed in the figure) that represent the overall dephasing of the system.

Source: By the author.

We can see in Figure 39 a typical Rabi oscillations measurement from our sample, showing the decay of the spin coherence over the whole imaged area. The maximum

fluorescence intensity corresponds to the NV spin population occupying the $|0\rangle$ state, whereas minimum fluorescence intensity corresponds to the NV spin population in the $|1\rangle$ state. These signals allow one to easily determine the duration of the π-pulse for each specific MW power and frequency. As shown in Figure 39, the results for the π-pulses are 150 ns at 40 dBm and 120 ns at 45 dBm.

Choosing an intermediate pulse time, between 0 and π-pulse, we can obtain a superposition state. For example, for a $\pi/2$-pulse one can drive from state $|0\rangle$ to state $(|0\rangle + |1\rangle)/\sqrt{2}$. These type of operation are of crucial importance in quantum information.

Looking at our data, we can see that as the microwave power decreases the π-pulse increases, i.e., the time to produce the transition from state 0 to 1 increases. So, increasing the MW power the population exchange between the levels is faster. Note that, the Rabi oscillations do not continue indefinitely, due to the limited spin coherence of the system. The way these measurements are done, they provide the effective T_2^* time, over the whole imaging area (or over some region of interest, if so selected). One can eliminate the effects of inhomogeneous dephasing by applying a Hahn echo sequence.

6.6.2 Ramsey sequence

We observe a decay curve consisting of the superposition of two cosine functions with different detuning due to hyperfine interaction with the ^{15}N, see equation (6.7). Figure 40 shows the measurement performed for two different detunings from the central resonant frequency ($f = 2794$ MHz). The average dephasing time T_2^* for the measurements is ~ 268 ns.

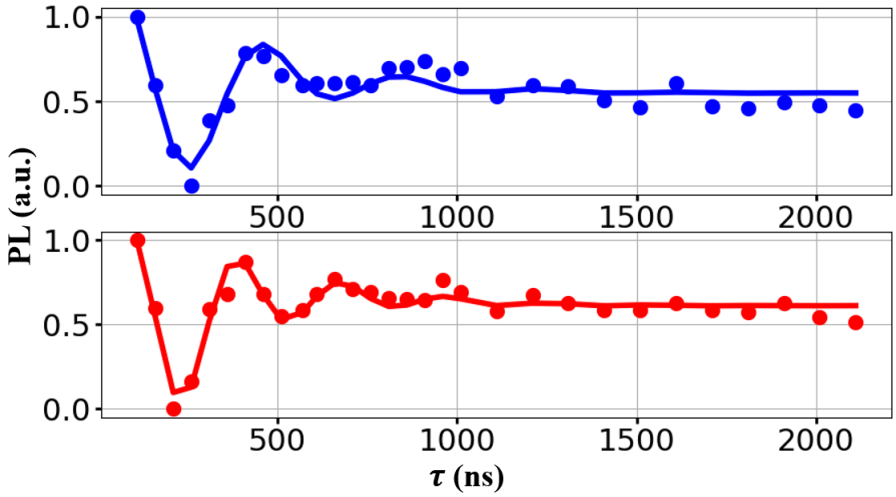

Figure 40 – Ramsey sequence for two different detuning, $f_{MW} = 2792$ MHz (blue) and $f_{MW} = 2795$ MHz (red). The two frequencies corresponding to the two different spin states of the ^{15}N nuclear spin shape the oscillatory pattern.

Source: By the author.

6.6.3 Two-pulse ESEEM or Hahn echo

The hyperfine interaction of the spin of the NV center with its near ^{15}N nucleus ($I = 1/2$) leads to a two-fold splitting, as discussed in chapter 2. Figure 36 show this very clearly in the ODMR spectrum. While trying to measure T_2 time, using a Hahn echo sequence, we observed a modulation signal on top of the expected exponential decay of the echo amplitude. The frequency of this modulation corresponded to the same frequency of this hyperfine interaction. Further analysis, lead us to identify this effect as resulting from ESEEM, whose results we discuss here.

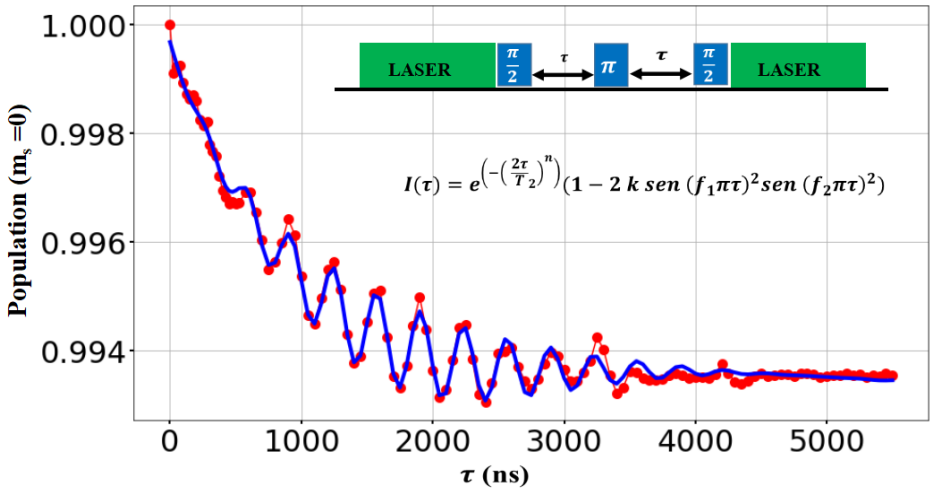

T_2	2.17 ± 0.08 us
f_1	3.022 ± 0.009 MHz
f_2	198.84 ± 5.78 kHz
n	0.792 ± 0.041
k	0.59 ± 0.04

Figure 41 – Two-pulse ESEEM, the red curve is the fit to the equation (6.8), resulting in two frequency components $f_1 = 3.022$ MHz and $f_2 = 198.84$ KHz.

Source: By the author.

Figure 34 shows the ESEEM modulation directly on top of the decay of the echo amplitude. As discussed in previous section, this coupling induce modulations at two frequencies $f_1$and f_2, corresponding to the ^{15}N Larmor precession frequencies for electron spin sub-levels $m_s = 0$ and $m_s = +1$. From the best fit of the experimental data to the expression shown in the figure, we obtain the frequencies $f_1 = 3.022$ MHz (hyperfine coupling frequency) and $f_2 = 198.84$ kHz, proportional to the perpendicular component of the external magnetic field relative to the NV center symmetry axis (76, 80). These measurements correspond to a magnetic field of 38.4 G along the NV direction.

From the data, we obtain $T_2 = 2.17\,\mu$s. This is due to the presence of a natural abundance of ^{13}C and relatively high concentration of nitrogen in the ensemble. (58)

6.6.4 Three-pulse ESEEM

According the discussion on the appendix A, the decay for this sequence is governed by the spin-lattice relaxation (T_1), the electron cross relaxation, and the nuclear spin-spin

relaxation. All these processes are much longer than T_2, allowing for higher resolution.

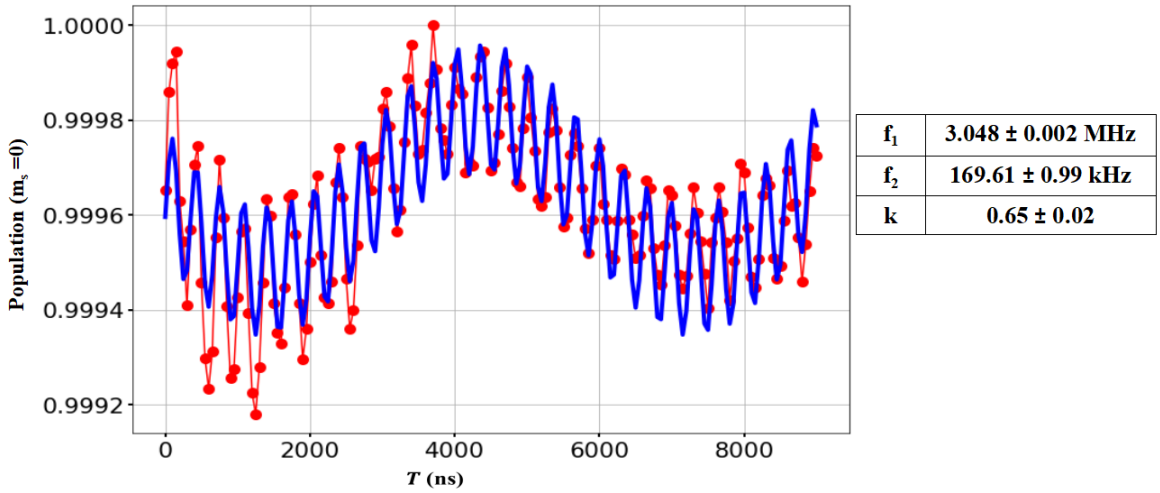

Figure 42 – Three-pulse ESEEM. Data were collected with the follows conditions, MW power is 45 dBm, π-pulse is 88 ns and τ is 1450 ns.

Source: By the author.

Figure 42 shows three-pulse ESEEM data collected for the same sample, under the same conditions, used in the two-pulse experiment. As expected, the longer coherence time allows for a better determination of the frequencies f_1 and f_2.

Equation (6.9) shows that the value of τ affects the amplitudes of the modulations, vanishing when $(1 - \cos(\mathbf{2}\pi\mathbf{f_{1,2}}\tau)) = 0$,. In our experiment, we chose $\tau = 1450$ ns, for the best compromise in the signal amplitude.

6.6.5 T_1 spin relaxation time

The pulse sequence for measuring T_1 is shown in Figure 43. In our experiment, each sequence begins with a 300 μs green light pulse, to optically pump the NV centers into the $|0\rangle$ state, thereby creating spin polarization into the $m_s = 0$ ground state. Then a resonant microwave π-pulse is applied to transfer the NV centers into the $|1\rangle$ state (or $|-1\rangle$, depending on the chosen frequency). After an adjustable time delay of τ, another light pulse is applied, and the NV fluorescence is detected to determine the remaining spin polarization of the color centers.

As a result, we observe the decay of the spin polarization, corresponding to the relaxation of the population back to the thermally mixed state, that existed before the optical pumping. As shown in Figure 43, this process happens in a time $T_1 = 1.78$ ms.

It is worth mentioning that an advantage of using a CCD camera as a detector is the ability to quickly analyze an extended area with micrometric (or sub-micrometric) resolution while keeping a good signal to noise ratio, as shown in Figure 44. This figure

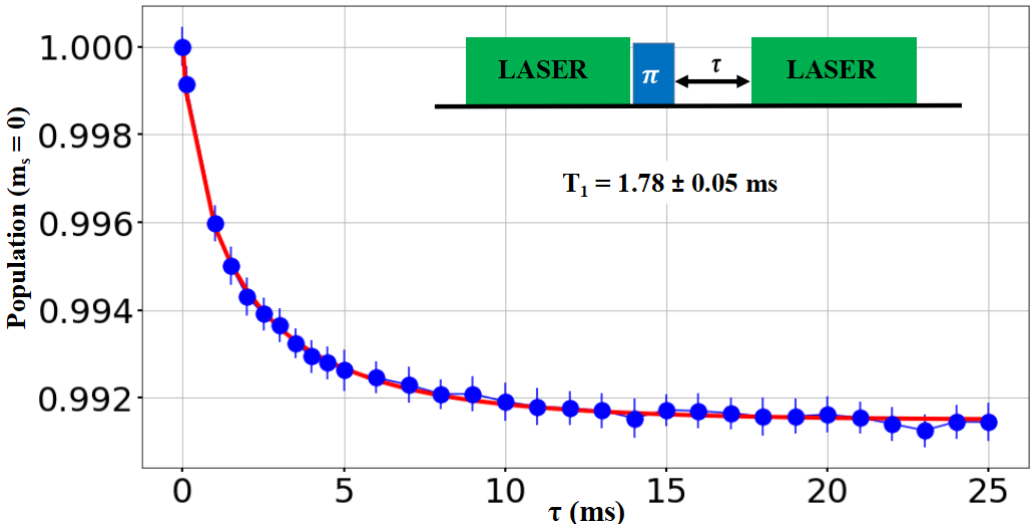

Figure 43 – Pulse sequence for measuring T_1 of an NV ensemble.

Source: By the author.

shows, however, that this analysis must be done carefully, as larger areas may result in decreased contrast, due to larger inhomogeneity and dephasing. On the other hand, this also typically leads to less noise in the signal (compared to a single pixel), due to larger sampling. This tradeoff must be considered, depending on the purpose of the measurements.

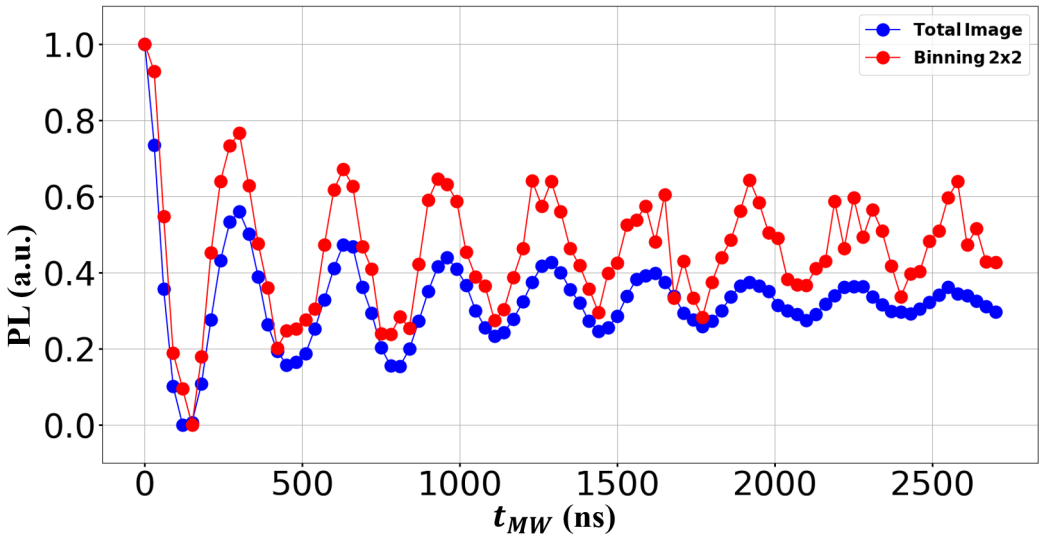

Figure 44 – Rabi oscillation of an NV ensemble, using the imaging method. The curves were built summing a 2x2 pixel region (red curve), and summing over the full image, in a region of 200x200 pixels (blue curve). The larger sampling in the full area, results in better signal-to-noise ratio, but also in lower contrast. Here, 1 pixel = 0.6 μm

Source: By the author.

7 FABRICATION OF NV CENTERS WITH FEMTOSECOND LASER

7.1 Introduction

The controlled fabrication of single NV centers or a controlled set of them is an important step in the development of semiconductor-based quantum devices (44, 81). This ability to engineer such devices could be widely used in quantum optics, magnetometry, thermometry, and other applications. This prompts the development of new methods that could be potentially be used for precise positioning of an individual NV center, or a small set of them, in particular regions of a diamond structure.

To generate the vacancies, the synthetic diamonds are typically irradiated with high-energy particles, from a few keV to MeV, usually electrons or nitrogen ion. In addition to the particle energy, another tunable parameter is the irradiation dose, which determines the density of vacancies generated in the sample. (82–84)

Alternatively, a recently proposed method is to use femtosecond laser illumination (21, 85–88), where the ultra-short intense pulses propagating in air induce ionization of molecules like O_2 and N_2, generating free electrons that are accelerated by the subsequent pulses, producing a beam of electrons that collide with some atoms of carbon at the diamond surface, taking them out of the crystal lattice, thus generating the vacancies. These vacancies can move during annealing (at high temperatures), therefore, creating the possibility of binding to some nitrogen impurity in the crystal, resulting in the NV center.

7.2 Femtosecond laser micromachining

Femtosecond laser micromachining is a process by which laser pulses are used to produce micrometric structures on the surface or volume of materials. This occurs due to the transfer of energy to a material, causing ionization. In solids, the photons transfer their energy to the crystalline lattice resulting in permanent damage. For microstructures to occur, the field strength must be high enough to promote multiphoton absorption. For a transition between bands to occur, the total energy absorbed by n photons must exceed the energy difference between bands, that is, $n\hbar\omega \geq E_g$. (89–91)

The outcome of micromachining is strongly dependent on experimental parameters such as excitation wavelength, pulse duration, energy, laser repetition rate, numerical aperture, focusing objective, and scan speed. Knowledge of the threshold for material ablation is crucial for the proper experimental parameter for devices fabrication. Here we use a method to determine the ablation threshold proposed by Liu. (92)

Considering a Gaussian pulse,

$$I(r,t) = I_0\, e^{-(t/\tau)^2}\, e^{-2(r/\omega_0)^2} \tag{7.1}$$

where I_0 is the peak intensity, τ is the pulse duration and ω is the beam waist diameter. Then, the fluence is obtained by integrating the intensity,

$$F(r) = F_0\, e^{-2(r/\omega_0)^2} \quad F_0 = \sqrt{\pi}\tau\, I_0 \tag{7.2}$$

Experimentally, accurate fluence measurements are difficult due to the small spot size of the focused beam. The ablation threshold fluence of a material can be determined by performing experiments with different pulses. It is more practical to work with pulse energy (E_p) rather than fluence. The energy of a pulse is obtained by integrating its fluence, such that

$$E_p = \frac{F_0 \pi}{2}\omega^2. \tag{7.3}$$

Adjusting the laser energy by one order of magnitude can cause dramatically different results: from no modification to the controlled modification used for producing optical devices, to uncontrolled damage as shown in Figure 46.

From equation (7.2) we can determine the radius (L) of the region of circular ablation, that has an associated threshold energy E_{th}, resulting in

$$L^2 = \frac{\omega_0^2}{2}\ln\left(\frac{E}{E_{th}}\right), \tag{7.4}$$

where E is the absorbed energy.

Another important experimental parameter for the micromachining processes is the laser repetition rate. In the femtosecond regime, the time interval is shorter than the time of thermal diffusion of various materials ($\sim 1\mu s$). (93) In this way, the thermal energy deposited per pulse accumulates inside the sample in the vicinity of the focus, due to insufficient time for it to diffuse out of the focal volume before the next pulse arrives. (94)

7.3 Experimental Procedure

The experimental setup for micromachining with ultrashort pulses requires an objective lens, a three-axis translation stage, a femtosecond laser, and a camera to follow the processing of micromachining in real time. Figure 45 shows a simplified schematics of such setup. The numerical aperture (NA) of the objective lens determines the focal volume, so its change enables to control the micromachined region, featuring the size and shape of micromachined structures.

We used a synthetic (CVD) diamond of dimensions $5 \times 5 \times 1\,\mathrm{mm}^3$, provided by the group of Prof. Carlos Graeff (UNESP, Bauru), for which we had limited information,

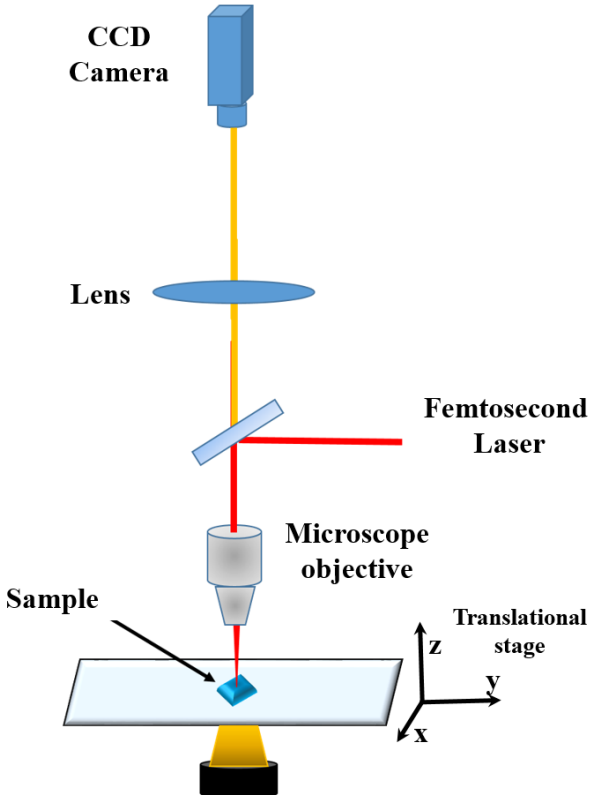

Figure 45 – Representation of experimental setup for femtosecond laser micromachining used to produce ablated grooves. The main elements are the laser, the translation stage, and objective lenses.

Source: Adapted from ALMEIDA (89).

except that it had very little nitrogen content (not used during fabrication). Other methods later confirmed this information.

The laser used to generate the defects in the diamond is a pulsed Ti-sapphire (Clark-MXR) laser at 775 nm, with pulses of 150 fs and the repetition rate of 1 kHz. After making the grooves with the laser, the sample was annealed at a temperature of 680 ^oC degrees for 30 min, to remove the amorphous carbon generated in the ablation process and to move the possible vacancies generated in the process. Finally, the sample was cleaned with a mixture of acids (hydrochloric acid, nitric acid, and sulfuric acid in the proportion of 1: 1: 1) to remove any remaining impurities from the surfaces.

Our interest is to produce the NV centers in a controlled manner, causing little damage to the sample. To establish some parameters, allowing to control the implantation, we did three experiments, that are described here. It is important to mention that the analysis of the first and second experiments was done at the beginning of this project, still in 2015, before we developed most our current infrastructure, such that we did not have all current methods available at of time.

First experiment

In this experiment, we study the damage threshold, finding the energy that causes the least damage to sample, by focusing the laser with an objective 100x (NA = 1.25) and moving the sample with a speed of 10 μm/s to make lines at different laser powers.

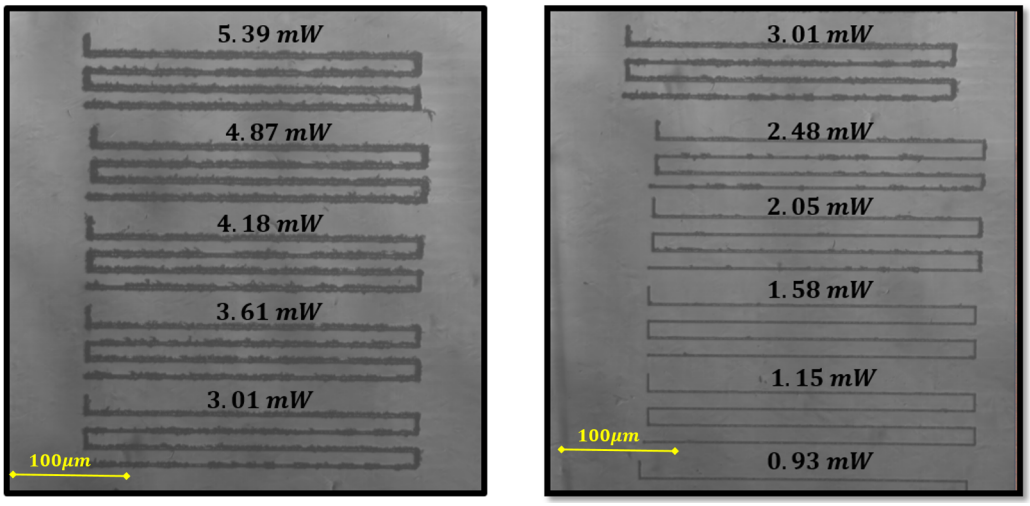

Figure 46 – Optical microscopy images from ablated grooves at diamond surface using femtosecond laser pulses to determine the threshold damage of the sample by the laser, the scanning speed is 10 μm/s. Objective 100x (NA = 1.25).

Source: By the author.

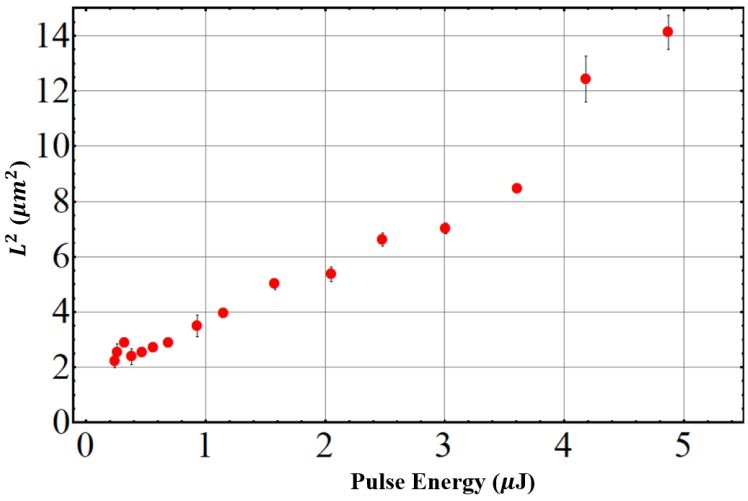

Figure 47 – Variation of the width of the optical damage as a function of the pulse energy for the diamond, using an objective x100 ($NA = 1.25$).

Source: By the author.

From the analysis of Figure 46, we built a table relating the grooves line width with the pulse energy of the laser, resulting in data of Figure 47. From the experiment

(Figure 47), we determined the threshold energy value $E_{th} = 0.24 \pm 0.02\,\mu$J.

The sample was later analyzed in a commercial confocal microscope system (Zeiss LSM-780) to observe if the ablated regions produce fluorescence when pumped with a laser at 543 nm. More specifically, we probed the fluorescence spectrum for the presence of NV centers. Figures (48) show that at laser power $\sim$ 3 mW or higher we observe many optically active defects, emitting fluorescence in diverse regions of the image.

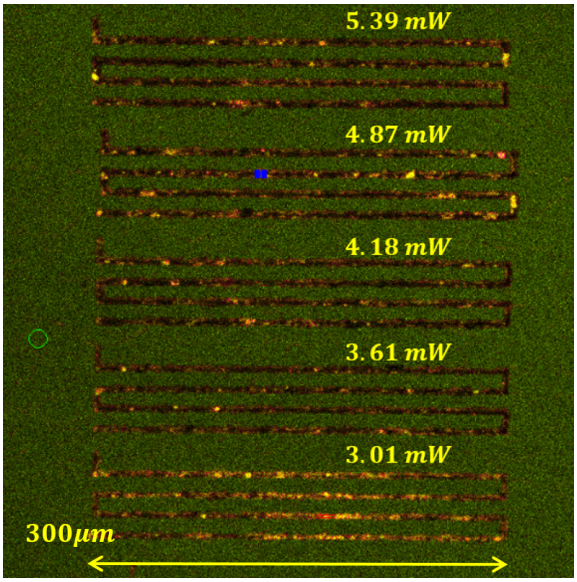

Figure 48 – Image of the confocal microscope (excitation at 543 nm) of the grooves made to calculate the damage threshold.

Source: By the author.

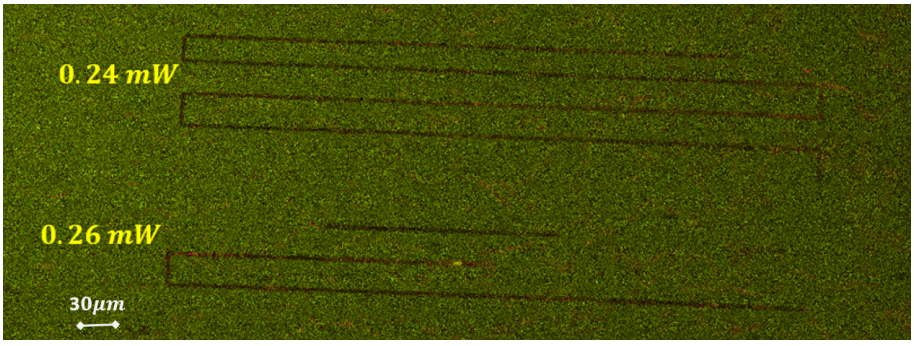

Figure 49 – Image of the confocal microscope (excitation at 543 nm) of the grooves made with low energy.

Source: By the author

In contrast, at lower powers, in Figure 49 not many defects are observed in the image, maybe because the fluorescence is low compared to background fluorescence (excitation laser scattering).

Figures 48 and 49 provide a viable region of values for the intensity of femtosecond laser. To generate the defects the power should not be too low, on the other hand, we intend to do the least damage in the sample, while still producing the NV defects.

Second experiment

Based on the first experiment, we planned the second experiment, still drawing lines, but starting with the focal point at 50 μm below the surface and moving it upwards in steps of 10 μm, up to a distance of 20 μm above the surface. For this experiment, the microscope objective was a 60× (NA = 0.85), and the laser power was fixed at 2.45 mW.

The ablated grooves made using this procedure are shown in Figure 50 and the image of the confocal microscope is shown in the Figure 51, where it can be seen that when the focus is 20 μm above the surface (groove 8), the damage caused is significantly lower, when compared the others. More interestingly, we can still observe some fluorescence for defects produced under such conditions.

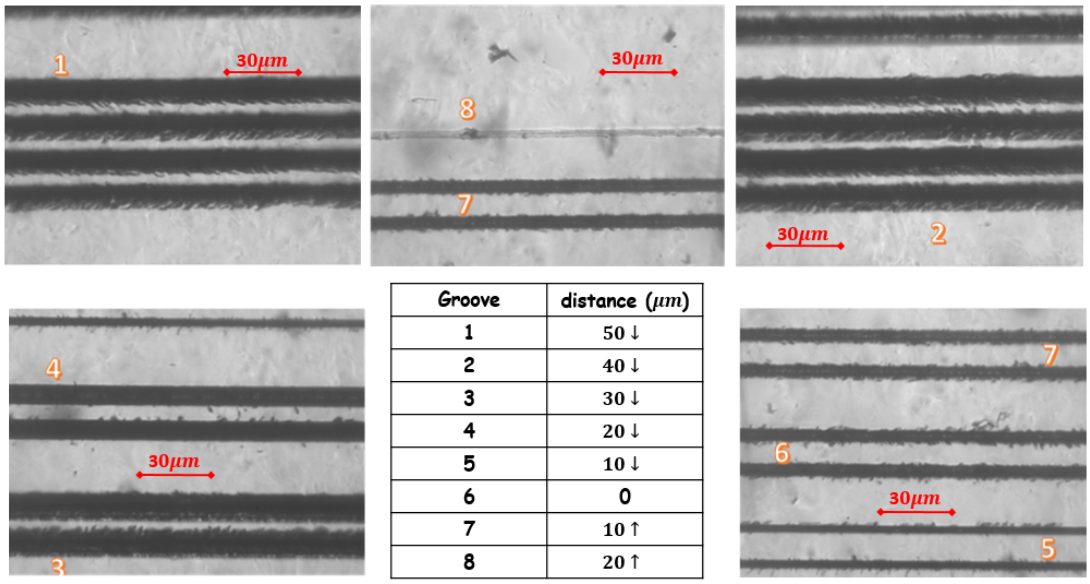

Groove	distance (μm)
1	50 ↓
2	40 ↓
3	30 ↓
4	20 ↓
5	10 ↓
6	0
7	10 ↑
8	20 ↑

Figure 50 – White-light microscopy images showing the morphology damage lines written inside fused diamond at 10 μm/s for different distance between the surface and the focus the laser. The pulse energy used was 2.45 μJ and the objective used is ×60 (N.A = 0.85). The arrow next to the number show if the focus is inside (↓) or up the surface (↑) of the diamond.

Source: By the author

At first, while still we were developing our own diagnostic infrastructure to detect NV centers, we did a study with Raman spectroscopy, since according to the references (95–97) the center NV^0 has a peak near 2050 cm^{-1} and NV^{-1} near 3750 cm^{-1}. The idea was to probe the fluorescing regions to find out if any was related to NV centers.

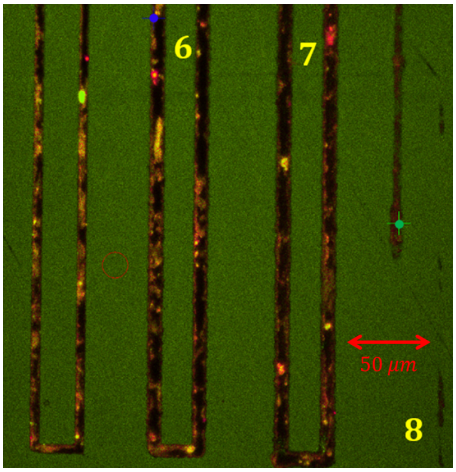

Figure 51 – Confocal microscope image, laser excitation of $\lambda = 543\,\text{nm}$. Grooves made with an objective $\times 60$ and $NA = 0.85$.

Source: By the author.

Figure 52 shows an example of the Raman spectrum from a representative groove. Analyzing many Raman spectra, we did find the characteristic peaks of NV centers (95–97), although it does not appear in all the grooves, suggesting a stochastic process, that depends on several parameters, and especially the pulse energy. In addition, in Figure 52 we see that ablation has generated some C-N bonds, as reported in table 2.

Table 2 – Raman spectroscopy.

Experimental peaks (cm^{-1})	Peaks in the references (cm^{-1})	Chemical bonds
220	220	$\beta - C_3N_4$
274	284	
300	300	
370	362	
893	892	
1050	1048	
1220	1238	
1250	1275	$C_x\,N_y$
1332	1332	Diamond
1480	1480	$\beta - C_3\,N_4$
2260	2260	Silicon impurities

Source: Adapted from IAKOUBOVSKII (95); VLASOV (96); WANG (97).

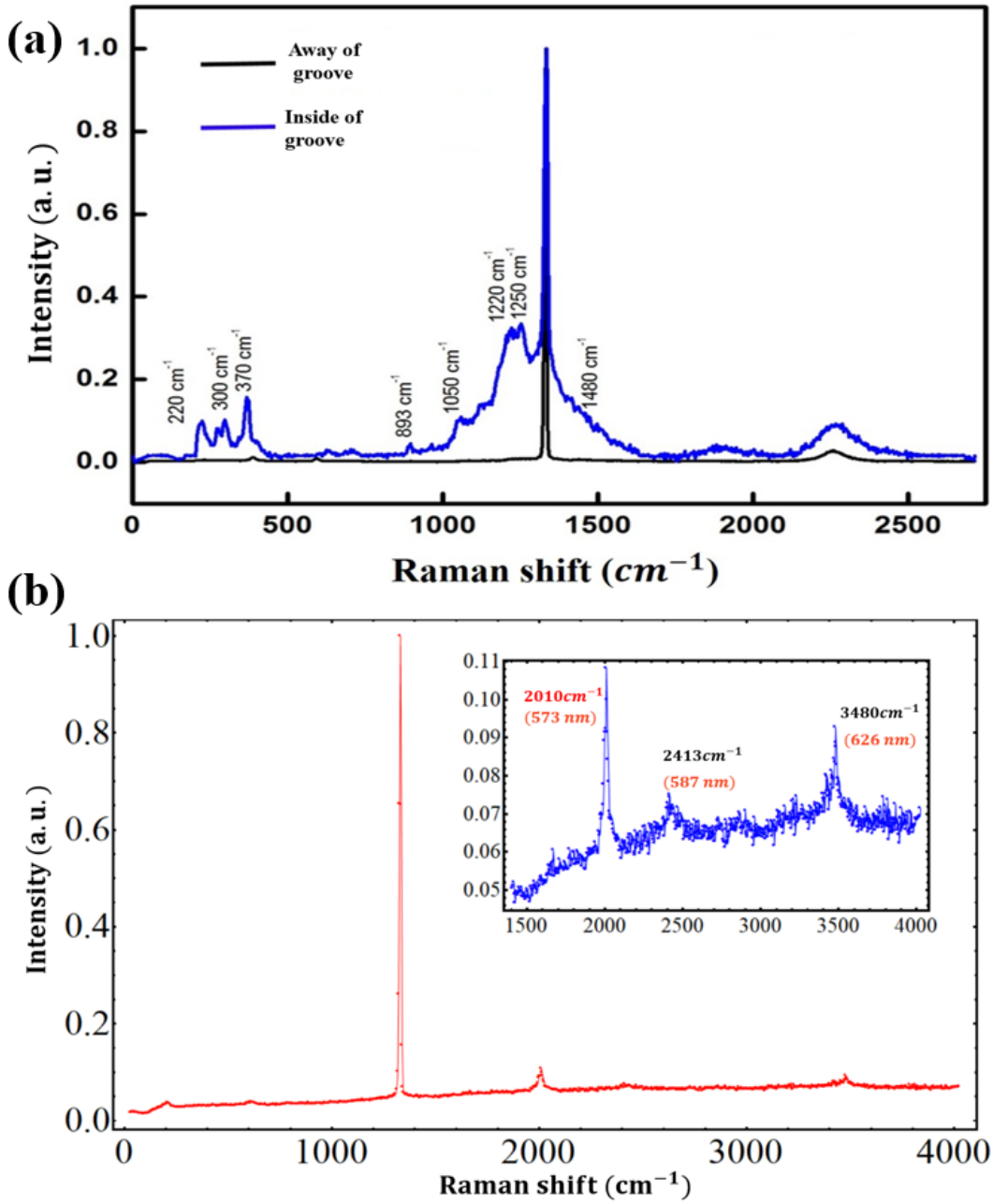

Figure 52 – (a) Raman spectroscopy (He-Ne laser, 632.8, nm). We show the Raman spectroscopy onto the surface that was not damage with the laser (black line) and onto the groove 3 (blue line), see Figure 50 (b) Raman spectroscopy (Ar laser, 514nm), in another side the groove.

.

Source: By the author.

Third experiment

Another parameter important to be analyzed is the energy deposited in the sample (irradiation intensity). For that, we performed another experiment, and we produce a set of spots with different illumination times. Figure 53 shows data at 2 s , 4 s , 7.75 s , 15.75 s , 31.25 s and 62.5 s. The illumination was done with an objective lens of 60x (NA=0.85), the pulse energy was 2.48 μJ (Ti:Sapphire (Clark-MXR),775nm,1 kHz) and the focus of the laser must be above the surface of the diamond, around $15 \pm 1\,\mu$m .

The fluorescence analysis was done in our home-built microscope set-up, where it is possible to obtain the fluorescence spectra and also allows us to do studies using the technique of optically detected magnetic resonance.

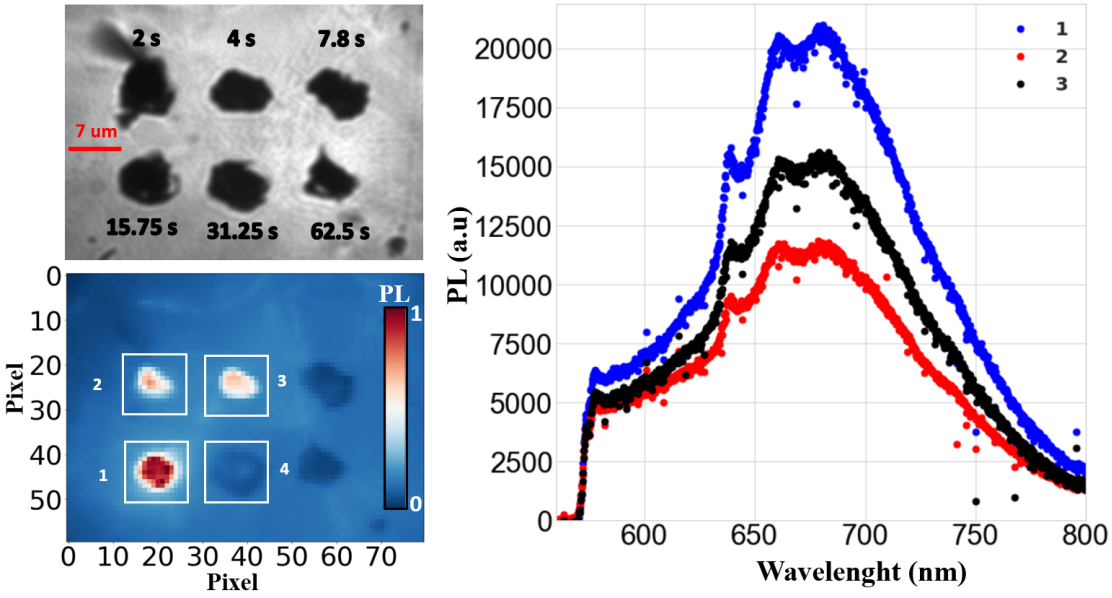

Figure 53 – Left-upper: White light microscopy image. Left-lower: The room-temperature photoluminescence. Right: PL spectra measured inside of region 1, 2 and 3 at 300K. Excitation was at 532 nm. 1 pixel = 0.7 μm.

Source: By the author.

Figure 53 shows photoluminescence emission, along with the typical spectra of the NV center at 300 K for three of the highlighted regions in the image.

We have analyzed the signal at each region by fitting the ODMR spectra with a sum two Lorentzian curves, as expressed by

$$y = A\left(1 - C_1\frac{1}{1+(\frac{x-f_0+E/2}{w_1})^2} + C_2\frac{1}{1+(\frac{x-f_0-E/2}{w_2})^2}\right) \tag{7.5}$$

where C_i is the contrast of each peak, f_0 is the central position the spectrum, E is the strain and w_i is the linewidth. For each region, Lorentzian fits were applied to the ODMR spectra and the parameters of equation (7.5) were extracted, as shown in Table 3.

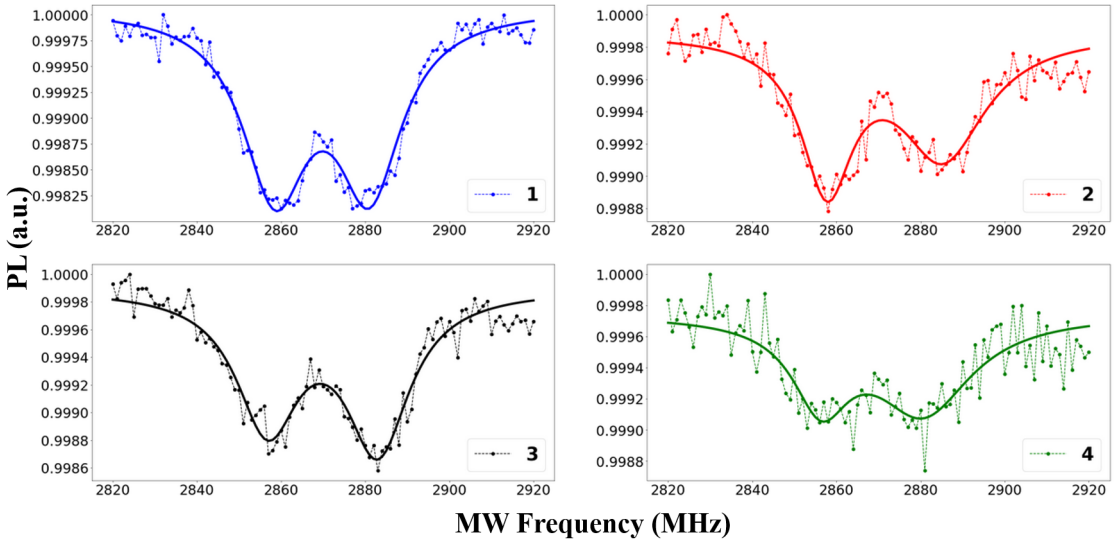

Figure 54 – Zero field ODMR of the four regions. The experimental data was fit by a set of two Lorentzians.

Source: By the author.

Table 3 – Parameters to fit the Zero field ODMR.

Region	1	2	3	4
E (MHz)	22.44	27.52	26.18	24.28
w_1 (MHz)	9.35	7.35	9.06	8.18
w_2 (MHz)	9.28	12.42	9.19	14.16
f_0	2869.80	2871.53	2869.91	2868.49
C_1 (%)	0.172	0.092	0.098	0.053
C_2 (%)	0.169	0.075	0.113	0.062

Source: By the autor.

These experiments showed that the creation of the NV center is a stochastic process. (21, 86) Besides, in Figure 53 we can see that the minimum time to create an ensemble of NV is 2 s, at the power level and conditions used here. From the zero-field ODMR, we observed that the local field (strain) around the NV center is much higher than usual, and it changes with the illumination time, this may be because the femtosecond laser modifies the local structure of the diamond, in the region illuminated by the laser.

For this reason, we intend to systematically investigate the relationship between the laser irradiation intensity and the coherence time, besides knowing the hyperfine interaction of the NV center. To carry out these studies, the Hahn echo and ESEEM sequences of three pulses will be used.

8 NONLINEAR OPTICAL SPECTRUM OF DIAMOND AT FEMTOSECOND REGIME

The study and parts of the text in this chapter have been published in ref. (22). Here we expand on that discussion, offering more context on the subject and including a brief review on relevant topics of nonlinear optics and more details on the experimental setup.

8.1 Introduction

Diamond presents a striking combination of mechanical, thermal and optical properties, which has prompted its investigation for the development of a new generation of photonic devices that are expected to overcome the silicon limitations. (98) Among its features are the wide transmission window, a low absorption loss and a high index of refraction, associated with excellent hardness and thermal conduction, all supporting the use of diamond in the design of integrated nonlinear and quantum optical platforms. Particularly, its ability to hold stable color centers, able of acting as single photon sources, has motivated many applications in quantum information science. (98–101) Recent advances on the fabrication of synthetic diamonds, along with good control of color centers have resulted in significant progress towards the development of diamond Raman lasers (102, 103) and quantum optics. (98, 101, 104, 105) On the other hand, studies on the nonlinear optical properties of diamond are still limited, hindering the full development of integrated diamond photonics platforms. (20) Currently, the available data are restricted to a few measurements of optical nonlinearities at specific wavelengths (106–110), impairing the analysis of the spectral behavior of the optical nonlinearities.

Therefore, considering the interests on diamond nonlinear photonics, this work presents measurements of third-order optical nonlinearities in type IIa diamond, performed over a broad spectral range, from 0.83 – 4.77 eV (1500 – 260 nm), at femtosecond regime.(22) To the best of our knowledge, this is the first report of such a wide range of nonlinear optical properties in diamond, particularly for nonlinear refraction and absorption. The measurements that were obtained by Z-scan technique are compared to theoretical prediction for indirect gap semiconductors, which is based on phonon-assisted two-photon absorption (111–113). In addition to the nonlinear refraction and absorption data, it is also presented here the optical Kerr gate data, to confirm the response time of the nonlinear refraction in diamond. Together, these measurements in such a broad spectral range are of foremost relevance to determine the correct order of magnitude of the two-photon absorption coefficient, still in debate in the literature, and to unravel the dominant underlying mechanism responsible for the nonlinear refraction in diamond.

8.2 Nonlinear Optics

Studies (20, 106, 114) show that the optical properties of matter vary with the intensity of light. High light intensities can cause changes in the optical properties of the medium by changing, for example, the refractive index or the coefficient of absorption. In nonlinear optics, the electrical susceptibility χ, which represents the optical properties of the medium, depends on the electric field. In general, we can expand the polarization P into a power series of the electric field, like

$$P(t) = \epsilon_0 \left(\chi^{(1)} E(t) + \chi^{(2)} E(t)^2 + \chi^{(3)} E(t)^3 + \ldots \right) \tag{8.1}$$

where ϵ_0 is the vacuum permittivity. The term $\chi^{(1)}$ is the linear susceptibility, which represents the linear properties, such as the index of refraction, absorption, and birefringence, this term is much higher than the highest order terms. The quantities $\chi^{(2)}$ and $\chi^{(3)}$ are the second and third order optical susceptibilities respectively. The $\chi^{(2)}$ represents the non-linear properties the second-order, while $\chi^{(3)}$ is related to third-order processes such as the generation of the third harmonic, Raman scattering and Kerr effect.

8.3 Third-Order Nonlinear Optical Properties

Considering the simplest case, a monochromatic field $E(t) = E_0 \cos(\omega\, t)$ is applied to a medium with inversion symmetry ($\chi^{(2)} = 0$), such that the polarization can be expressed as

$$P(t) = \epsilon_0 \left(\chi^{(1)} E(t) + \chi^{(3)} E(t)^3 \right) \tag{8.2}$$

with

$$P^{(3)}(t) = \epsilon_0 \chi^{(3)} E(t)^{(3)} = \epsilon_0 \chi^{(3)} E_0^3 \cos^3(\omega\, t), \tag{8.3}$$

which becomes

$$P^{(3)}(t) = \frac{\epsilon_0 \chi^{(3)} E_0^3}{4} \cos(3\omega\, t) + \frac{3\epsilon_0 \chi^{(3)} E_0^3}{4} \cos(\omega\, t). \tag{8.4}$$

The first term in equation (8.4) reveals the generation of the third harmonic, where three photons of frequency ω are destroyed and a photon of frequency $3\,\omega$ is created. The second term describes the nonlinear contribution of polarization keeping the same incident frequency ω.

We are interested in samples with inversion symmetry, where

$$P = \epsilon_0 \left[\chi^{(1)} + \frac{3}{4} \chi^{(3)} E_0^2 \right] E(t). \tag{8.5}$$

Assuming that light is propagating in the direction z, Maxwell's equations give

$$\frac{\partial^2 E}{\partial z^2} - \mu_0 \epsilon_0 \frac{\partial^2 E}{\partial t^2} = \mu_0 \frac{\partial^2 P}{\partial t^2}, \tag{8.6}$$

using the equation (8.5) we obtain

$$\frac{\partial^2 E}{\partial z^2} - \mu_0 \epsilon_0 \left[1 + \chi^{(1)} + \frac{3}{4}\chi^{(3)} E_0^2\right] \frac{\partial^2 E}{\partial t^2} = 0. \tag{8.7}$$

From equation (8.7) we obtain

$$\frac{1}{v^2} = \mu_0 \epsilon_0 \left[1 + \chi^{(1)} + \frac{3}{4}\chi^{(3)} E_0^2\right] \tag{8.8}$$

where v is the speed of light in the medium, so

$$\left(\frac{c}{v}\right)^2 = n^2 = 1 + \chi^{(1)} + \frac{3}{4}\chi^{(3)} E_0^2 \tag{8.9}$$

and then

$$n = \sqrt{1 + \chi^{(1)}} \left[1 + \frac{3\chi^{(3)} E_0^2}{4(1 + \chi^{(1)})}\right]^{1/2} \tag{8.10}$$

$$n \approx n_0 \left[1 + \frac{3\chi^{(3)} E_0^2}{8\, n_0^2}\right]. \tag{8.11}$$

Now, remembering that intensity (I) is given by

$$I = \frac{1}{2}\, c\, n_0\, \epsilon_0\, E_0^2 \tag{8.12}$$

we obtain

$$n = n_0 + \frac{3\chi^{(3)}}{4 c n_0^2 \epsilon_0} I \;\Rightarrow\; n = n_0 + n_2\, I. \tag{8.13}$$

where n_0 is the linear refractive index, n_2 is the nonlinear refractive index and I is the light intensity. It is worth noting that in this section, to simplify calculations, we considering that $\vec{E}$ and $\vec{P}$ fields are in the z-direction, and so, we work with χ being scalar. So, to generalize we must use the vector form of the fields and the tensorial nature of the electric susceptibility.

The refractive index, equation (8.13), depends on the intensity of the radiation, so it is different along the beam profile.. Rays near the optical axis refract more than rays farther away from the axis. Thus, some materials may behave like a lens, focusing or diverging the light that propagates through it depending on its nonlinear properties. This effect is called self-focusing (for $n_2 > 0$) or de-focusing (for $n_2 < 0$).

Recalling that the susceptibility is a complex quantity, different non-linear optical effects are associated with the real and imaginary part of the susceptibility, $\chi^3 = \chi_R^{(3)} + i\chi_I^{(3)}$. The momentary change in the refractive index (n), known as the optical Kerr effect, is associated with the real part of $\chi(3)$. The nonlinear absorption coefficient (β_2) is related to the imaginary part of $\chi^{(3)}$, in such a way that

$$\beta = \beta_0 + \beta_2\, I \;\Rightarrow\; \Delta\beta = \beta_2\, I\,. \tag{8.14}$$

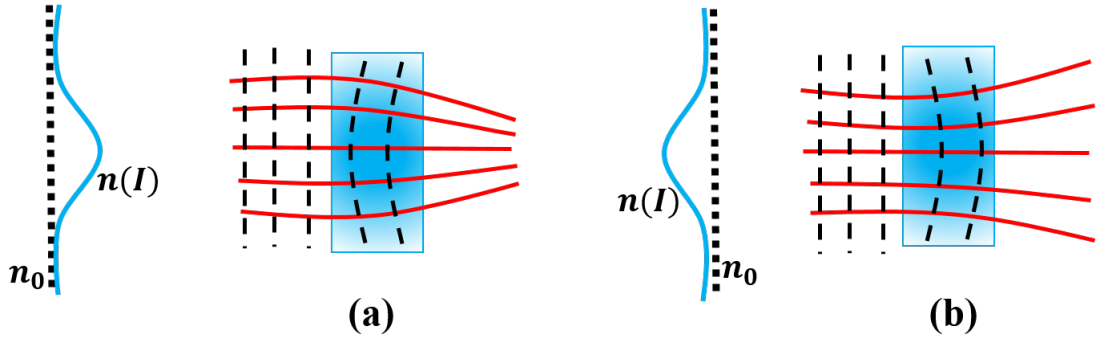

Figure 55 – (a) Self-focusing for $n_2 > 0$ and (b) de-focusing for $n_2 < 0$ produced by a medium on a light beam with intensities $I(r) \propto e^{-\alpha r^2}$.

Source: By the author.

Based on the principle of causality, Kramers-Krönig relates the index of refraction and the coefficient of absorption as follows

$$n_2(\omega) = \frac{c}{\pi}\int_0^{\infty} \frac{\beta_2(\omega,\omega')}{\omega'^2 - \omega^2} d\omega' \quad \left[\frac{\mathrm{m}^2}{\mathrm{W}}\right] \tag{8.15}$$

The theory based on second-order perturbation developed by Sheik-Bahae *et al.* (114, 115) has been applied to modeling the dispersion of optical nonlinearities in wide-gap dielectrics and direct gap semiconductors. This theory does not include phonon-assisted transitions; therefore a few models have been proposed for indirect gap materials (104, 111, 112), which is the case of diamond and other group IV semiconductors (Si and Ge).

The formalism proposed in the references (111,113) enables to predict the dispersion of the Two-photon absorption (2PA) coefficient for indirect gap semiconductors, considering the sum of three transition processes: allowed-allowed ($i = 0$), allowed-forbidden ($i = 1$), and forbidden-forbidden ($i = 2$), according to

$$\beta_2(\omega) = \sum_{i=0}^{2} \beta_2^{(i)}(\omega) \quad \left[\frac{\mathrm{cm}}{\mathrm{GW}}\right], \tag{8.16}$$

using

$$\beta_2^{(i)}(\omega) = K_i \frac{1}{n_0^2 E_{ig}^3} F_2^{(i)}\left(\frac{\hbar\omega}{E_{ig}}\right) \tag{8.17}$$

where

$$F_2^{(i)}(x) = \frac{(2x-1)^{i+2}}{(2x)^5}, \tag{8.18}$$

K_i is a curve-fitting factor, as described in refs (111, 113), E_{ig} is the indirect band gap energy, n_0 is the linear refractive index

8.4 Z-scan

The Z-scan is a technique of nonlinear spectroscopy that uses the effect of self-focusing or self-blurring of an intense light beam propagating in a nonlinear medium. (89, 115) This technique consists of focusing the laser beam and translating the sample in the vicinity of the focal plane of the lens, along with the direction of propagation of the light (direction Z), as shown in the Figure 56.

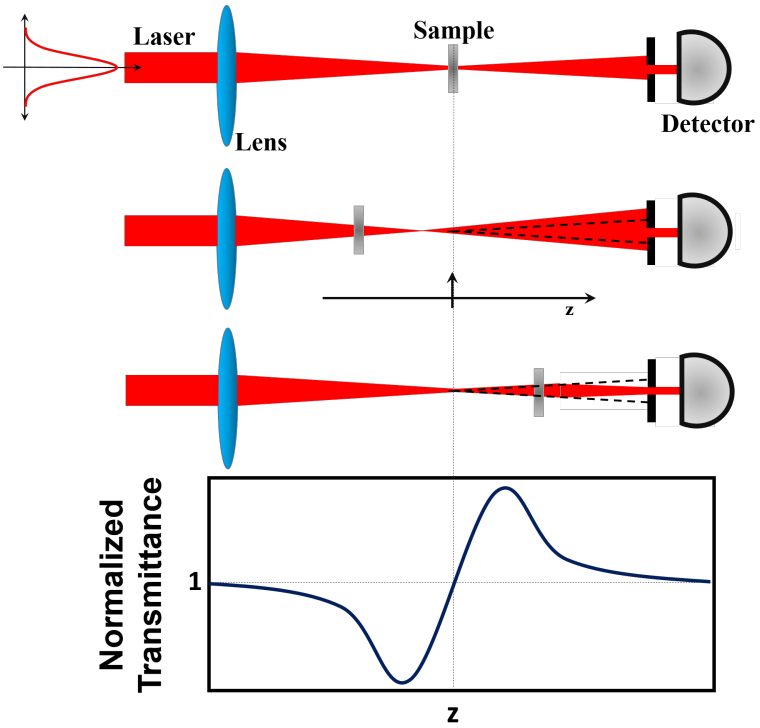

Figure 56 – Illustrative scheme of the experiment proposed by Sheik-Bahae to measure nonlinear refractive index and nonlinear absorption.

Source: By the author.

The beam focusing produces an intensity distribution in the direction Z, whose maximum is located at the focal region. To eliminate the linear effects, the power transmitted by the sample in a given position Z is divided by the power transmitted when the sample is far from the focus, where nonlinear effects are not present. This yields the normalized transmittance:

$$T_N(z) = \frac{P(z)}{P(z \to \infty)}. \tag{8.19}$$

When the sample is far from the focal region there are no nonlinear effects, therefore, $T_N = 1$. Considering that the material exhibits positive non-linearity ($n_2 > 0$), when it is in the pre-focal region ($z < 0$) it behaves like a positive lens, as shown in the Figure 55, this causes the beam to be focused before the position $z = 0$, decreasing the normalized

transmittance ($T_N < 1$). At the focal plane ($z = 0$), the sample acts as a thin lens, so it does not change the transmittance. In the region $z > 0$ the self-focusing effect decreases the divergence of the beam, thus increasing the normalized transmittance. If the non-linearity is negative ($n_2 < 0$), precisely the opposite happens. Figure 55 shows an illustration of these effects.

Considering that the pulsed laser has a Gaussian intensity profile, it is found that the nonlinear refractive index is related to the nonlinear phase acquired by the beam when it passes through the sample (115)

$$\Delta\phi = \frac{2\pi\, n_2\, I_0\, L}{\sqrt{2\lambda}}\,, \tag{8.20}$$

where λ is the wavelength, I_0 is the intensity of the beam in the focus, and L is the thickness of the sample. The phase $\Delta\phi$ is measured through the normalized transmittance curve, since

$$\Delta T_{P-V} = 0.406\,\Delta\phi_0 \tag{8.21}$$

where ΔT_{pv} is the difference between the maximum normalized transmittance (peak) and the minimum (valley). All these equations are expressed in the International System (SI) of units. From the last two equations, we can determine the nonlinear refractive index, expressed as:

$$n_2 = \frac{\sqrt{2}\,\Delta T_{pv}\lambda}{0.812\,\pi\, I_0\, L} \tag{8.22}$$

For measuring the real part of the nonlinear refractive index n_2, the Z-scan setup is used in its closed-aperture form. In this form, since the nonlinear material reacts like a weak z-dependent lens, the far-field aperture makes it possible to detect the small beam distortions in the original beam. To measure the imaginary part of the nonlinear refractive index, or the nonlinear absorption coefficient, the Z-scan setup is used in its open-aperture form. In open-aperture measurements, the far-field aperture is removed, and the detector measures the total signal. By measuring the total signal, the small beam distortions become insignificant, and the z-dependent signal variation is due to the nonlinear absorption entirely. Typical Z-scan transmittance curves are shown in Figure 57.

8.5 Results and discussions

In this study, we used a commercially available sample produced by CVD (chemical vapor deposition), corresponding to Element Six's highest purity diamond (type IIa, $2 \times 2 \times 0.5\,\mathrm{mm}^3$), whose nitrogen impurities are below 5 ppb (usually < 1 ppb) and the concentration of nitrogen vacancies are lower than 0.03 ppb. Crystallographic orientation is 100% single sector [100] and polishing. The diamond crystal lattice presents inversion symmetry, due to its cubic structure, and second-order nonlinearities are absent. Therefore,

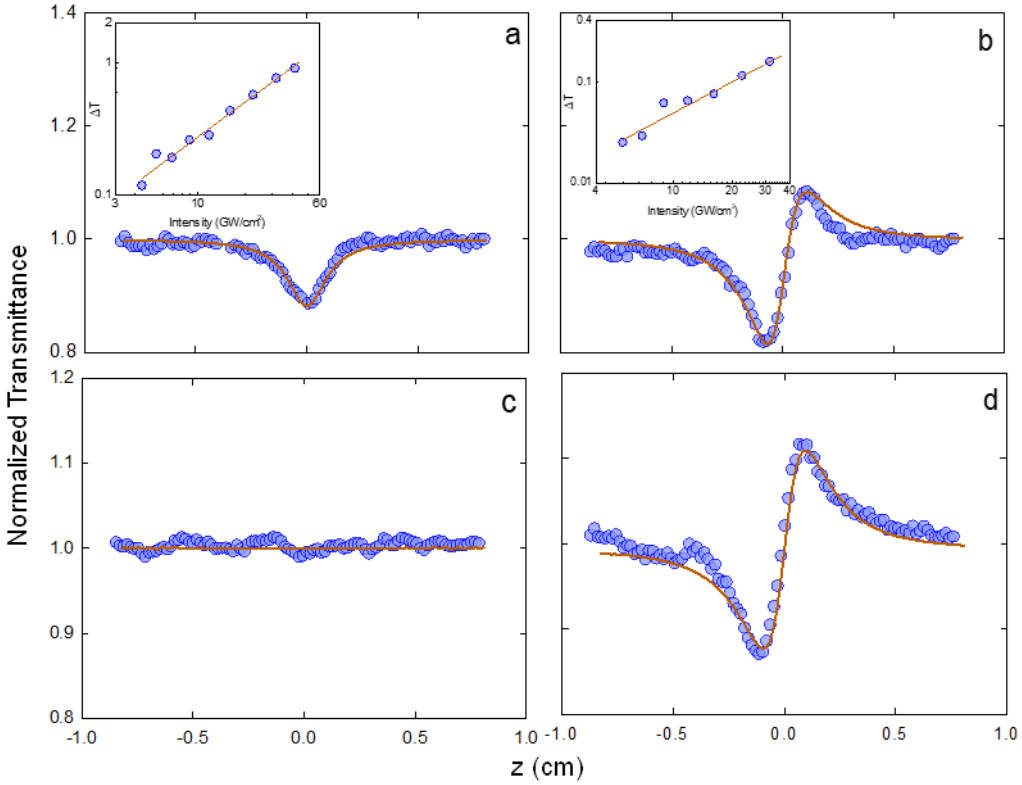

Figure 57 – Open and closed Z-scan signatures at 3.54 eV (350 nm) (a and b, respectively) and 2.21 eV (560 nm)(c and d, respectively). The inset in (a) and (b) displays the linear dependence on the transmittance change (ΔT) with the intensity at 3.54 eV (350 nm), whose slopes are approximately 1 in the log-log plot.

Source: ALMEIDA; ONCEBAY (22)

third-order processes are the lowest order ones, being the most relevant for diamond photonics.

Open and closed aperture Z−scan measurements were performed to study the nonlinear absorption and the nonlinear refraction, respectively. Femtosecond laser pulses from a Ti:sapphire chirped-pulse amplified system (150 fs, 775 nm and 1 kHz) were used to pump an optical parametric amplifier (OPA), which provides tunable 120 fs pulses from 0.62 to 2.7 eV (2000 − 460 nm). In Figure 57 we show Z−scan transmittance curves for two different excitation energy, first row with 3.54 eV (Figure 57 (a) and (b)) and second row with 2.21 eV (Figure 57 (c) and (d)) when the aperture is open and closed respectively. The decrease in normalized transmittance observed in the nonlinear absorption curve (open aperture), shown in Figure 57 (a), indicates a two-photon absorption (2PA) process. Two-photon absorption was only observed for excitation energy $\geq 3.18\,\text{eV}\,(\lambda \leq 390)$. For photon energies in which 2PA is significant, the refractive (closed aperture) Z-scan signature is asymmetric, with a valley greater than the peak, as displayed in Figure 57

(b). For excitation energies lower than 3.18 eV ($\lambda > 390$ nm), the refractive Z-scan curves become symmetrical, as illustrated in Figure 57 (d) representing an excitation at 2.21 eV (560 nm), indicating that the two-photon absorption process is not present anymore. This is confirmed by the lack of absorptive signature in Figure 57 (c). It is interesting to point out that the valley-peak configuration exhibited by the nonlinear refraction curves, see Figure 57 (b) and (d), are characteristic of positive n_2 values. The solid lines in Figure 57 are the best fit, obtained according to reference (106, 115), from which the nonlinear refractive index and nonlinear absorption coefficient can be obtained. The insets in Figure 57 (a) and (b) show the linear behavior of the transmittance change (ΔT) as a function of the light intensity at 3.54 eV (350 nm), as expected for third-order nonlinearities.

From Z-scan curves similar to the ones displayed in Figure 57, obtained at different excitation energies, the dispersion of β and n_2 can be obtained for the full spectral range, as seen in Figure 58. In this figure (closed circles) displays the experimental 2PA coefficient (β) spectrum of diamond. It is worth noting that 2PA was detected from 3.18 - 4.77 eV (390-260 nm), region where the photon energy $\hbar\omega$ is smaller than the band gap ($E_g = 5.54\,\text{eV}$) and higher than $E_g/2$.

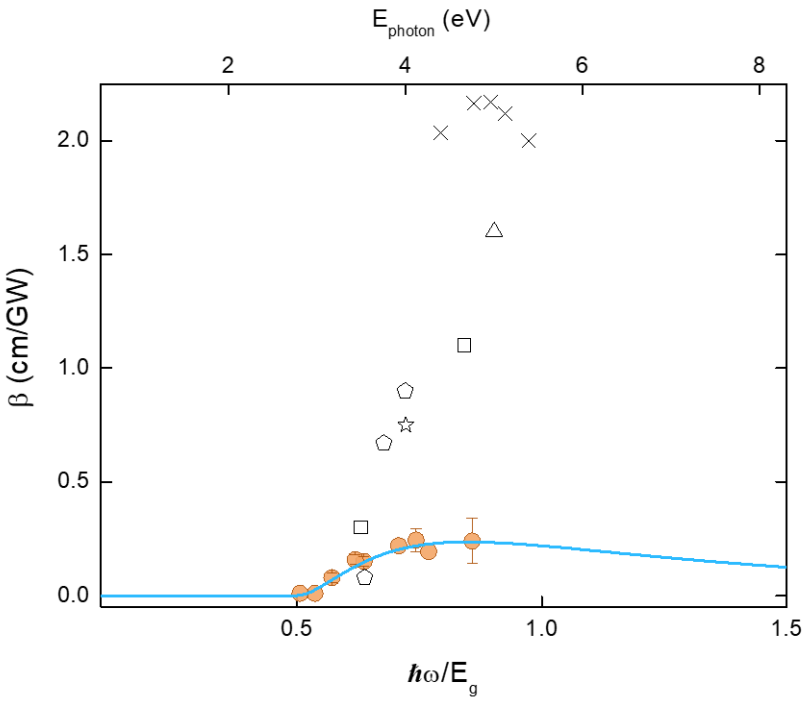

Figure 58 – Dispersion of the two-photon absorption coefficient (β) of diamond. Solid circles correspond to the experimental data obtained in this work and continuous line is the theoretical fit obtained from equation (8.16). Literature data are plotted as crosses (116), up-triangles (117), squares (106), pentagons (107) and star (118).

Source: ALMEIDA; ONCEBAY (22)

The model given by equation (8.16) can be applied as a universal expression for in-

direct semiconductors, that enables predicting the 2PA coefficient in a wide spectral range. The solid line in Figure 58 represents the fit obtained using $K_0 = 62.86 \times 10^{-9}\mathrm{m\,eV^3/W}$, $K_1 = 5.71 \times 10^{-9}\mathrm{m\,eV^3/W}$ and K_2 fixed as zero, once it has been shown that forbidden-forbidden transition can be neglected. (111) As can be seen, there is a good agreement between experimental data and model, indicating that 2PA is, in fact, the major contribution to the observed nonlinear absorption.

It is interesting to compare the experimental results presented in Figure 58 with the ones reported in literature (106, 107, 116–118), (open symbols and crosses) for better visualization. As it can be seen, the previously reported data for 2PA coefficients, obtained using different techniques, varies significantly, from values in the same order of magnitude up to one order higher than the values determined herein (0.07 to 0.23 cm/GW). Such wide difference may arise from a combination of the temporal regime of laser pulses (eventually leading to contributions from thermal effects) and the number of free carriers in diamond. Besides, of according to equation (8.16), 2PA coefficient scales with the inverse of the third power of the band gap energy (E_{ig}^{-3}), therefore for materials with large band gap energy, as diamond, it is expected that 2PA be low when compared to other indirect semiconductors, as Si and Ge. (111) Thus, the large values reported in the literature for 2PA in diamond might be related to other nonlinear optical processes rather than pure two-photon absorption.

From the closed-aperture Z-scan measurements, we obtain the value of n_2 and equation 3 we obtain the best fit. As can be seen, there is a good agreement between the experimental data (closed circles) and the model (solid line), see Figure 59. The open circle in Figure 59, at the right side of the graph, corresponds to the measurement performed at 4.77 eV ($\hbar\omega/E_{ig} = 0.86$; $\lambda = 260$ nm), in which the Z-scan trace exhibits only nonlinear absorption feature; therefore the n2 value was considered zero at this spectral position. Additional literature data (106–110) are also displayed in Figure 59 (open symbols).

No negative value of n_2 were observed in our measurements, even for $\hbar\omega/E_{ig} > 0.7$, supporting the hypothesis that the most significant contribution to the nonlinear index of refraction dispersion comes from the 2PA term. It is worth noting, however, that in reference (106) it was observed a negative nonlinear refraction at 3.49 eV (355 nm) employing picosecond laser pulses, while here a clear positive n_2 is observed at 3.54 eV (350 nm), as showed in Figure 59. At the picosecond regime excited state contributions may affect the determination of a pure electronic Kerr response, as opposed to femtosecond laser pulses, thus explaining the discrepancy. Besides, values of $1.3 \times 10^{-19}\,\mathrm{m^2/W}$ and $8.2 \times 10^{-20}\,\mathrm{m^2/W}$ has been reported for the visible and telecom regions, respectively. (20)

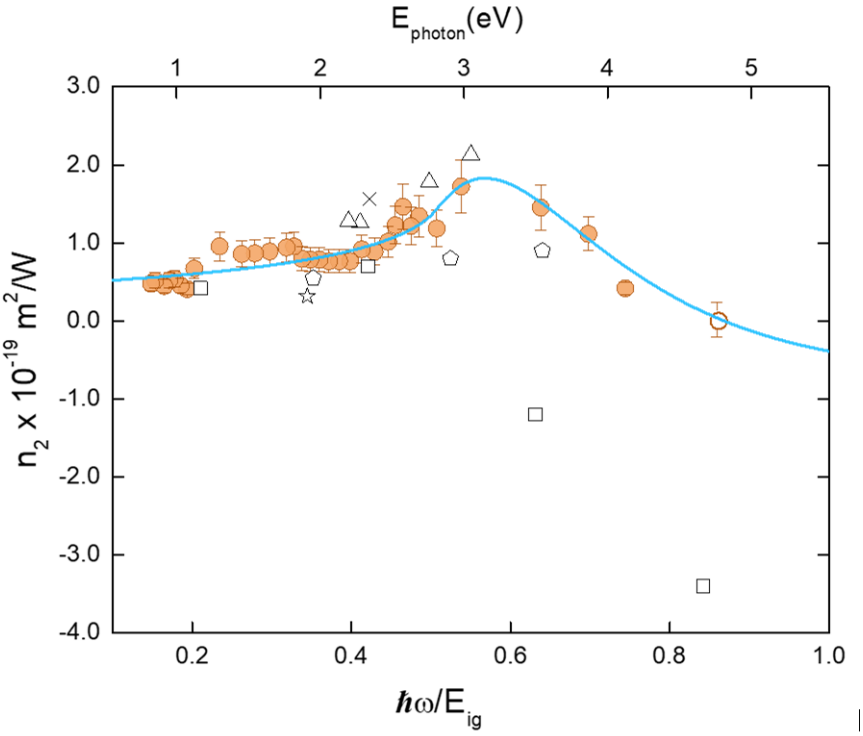

Figure 59 – Experimental (solid circles) and theoretical (solid line) dispersion of the diamond nonlinear refractive index. Squares (106), pentagons (107), star (108), cross (109) and triangles (110) correspond to the values find in the cited references. The values in (110) were increased by a factor of 4 to follow the calculation and definition of n_2 used herein.

Source: ALMEIDA; ONCEBAY (22)

9 CONCLUSION AND PERSPECTIVES

Some of the main conclusions of this work can be summarized as follows.

- The ability to map the magnetic vector fields with high sensitivity and spatial resolution, at room temperature, can provide additional information in a variety of areas previously not accessible with other magnetic detection technologies. In particular, a not-so-sophisticated camera and a relatively simple setup can be used to study magnetometry by imaging the photoluminescence of NV centers (either ensembles or single defects). The understanding of the parameters that affect the sensitivity of detection helps to establish better conditions to optimize the detection of magnetic fields. In our experiments, we obtain a sensitivity of $\eta = 6$ μT μm $\mathrm{Hz}^{-1/2}$. This value is particularly due to the contrast and the linewidth that we obtain, measuring contrasts in the range of 0.3% to 0.6% per pixel. These values are lower than those found in the literature (about 1%). (15, 63, 68) This is largely due to the limited power of the laser, $\sim$ 20 mW reaching the objective. Higher powers are needed to excite larger areas of the diamond surface, to have sufficient illumination to reduce shot-noise. Other sources that contribute to the contrast reduction are due to the fact that we collect the fluorescence of 4 sets of NV corresponding to the four possible orientations of the NV center. The contribution to the background of the NV^0 and the interaction of the NV center with the neighboring atoms also contribute to the reduction of the contrast. The simplest way to solve these difficulties was to carry out more measurements of the ODMR spectrum and to do a binning of pixels in the image, at the cost of losing some spatial resolution, while gaining in signal-to-noise.

  An important detail in our measurements of magnetometry is that the wire was made on the surface of a glass cover slides and not in the diamond. This was chosen to investigate a configuration providing more flexibility concerning changes of samples, but it also brings more uncertainty about the distance between the layer of NV and the wire because the diamond sample is not entirely flat. Our study shows that one can still gain information about the distance, from our analysis, in a relatively self-consistent way, but in the analysis of the magnetic field produced by a current of 15 mA (see Figure 28), we find that the distance between the layer of NV and the wire is around $\sim 12\,\mu$m. This partially justifies the reason why we had difficulties detecting magnetic fields produced by currents lower than 3 mA. For samples deposited on the diamond surface ($\sim$10 nm above the NV layer), we expect, at least, one order of magnitude improvement in the magnetic field sensitivity.

- We investigated several experimental methods to control the spin of the NV center, and performed measurements of the spin coherence properties of our sample, using a CCD camera as a detector. For that, we developed a protocol that allows for in-situ measurements of spin coherence properties, even when imaging extended areas at once. Provided that proper processing and illumination conditions are used, this method provide some advantages compared to usual PMT and APD point-scanning measurements, depending on the goal of the study to be realized. In principle, most of the pulse sequences used in NMR and EPR can be mapped into ESR measurement using the protocol presented in this thesis.

  Of the experiments carried out to extract relevant spin coherence properties for our sample, see Figure 43 and Figure 41, the times T_1 and T_2 are 1.78 ms and 2.17 μs respectively. We have also obtained information on hyperfine interaction with the ^{15}N, and observed ESEEM effect, both using a two-pulse and three-pulse sequences. Using a camera as a detector brings as an advantage the ability to analyze an extended area with micrometric resolution. This capacity is critical for the development of new technologies that allow studies in diverse areas such as biology, geology, medicine, and chemistry. Also, the sensitivity of magnetic field detection can, in principle, be improved by applying known dynamical decoupling techniques, from nuclear magnetic resonance, such as the Carr-Purcell-Meiboom-Gill (CPMG) sequence (58), and others currently studied in our laboratory.

- The goal of our studies with femtosecond laser was to establish conditions to produce NV centers with high-precision on a diamond surface, while causing the least possible damage to the surface. For that, we conducted three studies. First, we determined the damage threshold of the diamond surface. Second, we established the best position of the laser focus with respect to the surface. In a third experiment, we investigated the effect of the irradiation time on the sample, which, as we observed, can lead to substantial deformation of the sample surface, changing its ODMR properties.

  Initially, we used Raman spectroscopy to analyze ablated lines (grooves) on the diamond surface, searching for NV signatures. This study showed that the interaction of the laser with the sample does create several defects (see Figure 52 and table 2) within this set of defects we found NV centers. It also showed that fabrication of NV centers by femtosecond lasers is a stochastic process, confirming other results in the literature (105), and does not guarantee deterministic production these point-defects at a given location. It is still currently a challenge to understand and control all the parameters involved in this process. Therefore, further studies in this subject are necessary, to fully benefit from the potential of this fabrication process.

  Studies with fluorescence spectroscopy and ODMR confirmed the production of NV centers and provided useful information about each production site. Our experiments

showed that, under the conditions used here to create NV centers with minimum damage, it was necessary an energy $\sim 2.48\,\mu$J, with the focus of the laser positioned around 15 μm above the surface of the diamond, and an illumination time of approximately 2 s. It should be noted that these parameters depend on the characteristics of the laser used, among other things.

- Although diamond is an attractive material due to its thermal, mechanical and optical properties, research related to nonlinear properties were still limited.(20, 106) In this work we investigated the behavior of the nonlinear index of refraction (n_2) of the diamond (type IIa) in a wide spectral region, going from the infrared (1500 nm) to the ultraviolet (260 nm). Using simple Z-scan measurements (at several wavelengths) we obtained the third order nonlinear properties of diamond, mapping of the behavior of n_2 that in this wide spectral region, as shown in Figure 59. We also explored a theoretical model for this type of semiconductor, showing that our experimental data agree with this model developed in the references. (111, 113)

The studies explored in this thesis, allowed us to learn new techniques that were implemented in our laboratory with the purpose of exploring the properties of the ensemble of NV centers. The same basic infrastructure and techniques can be extended to explore single NV centers as well, an effort currently underway in our laboratory. All these efforts will allow us to continue with future experiments in magnetometry, trying to improve the sensitivity of magnetic field detection to study magnetic properties of advanced materials, such as semiconducting polymers and two-dimensional materials (like graphene), as well as start exploring new possibilities of studies in fundamental principles of quantum mechanics and new applications of quantum technologies. (8–11)

The implantation of NV centers with femtosecond lasers appears as a new alternative to produce NV centers in specific places. Many applications that use these NV centers depend on their coherence time. For this reason, we intend to systematically investigate the relationship between the laser irradiation intensity and the coherence time, using some of the techniques studied in this thesis.

REFERENCES

1 BREEDING, C. M.; SHIGLEY, J. E. The "type" classification system of diamonds and its importance in gemology. **Gems and Gemology**, v. 45, n. 2, p. 96 – 111, 2009.

2 MILDREN, R.; RABEAU, J. **Optical engineering of diamond**. Weinheim: John Wiley and Sons, 2013.

3 TALBOT-PONSONBY, D. F.; NEWTON, M. E.; BAKER, J. M. Electron paramagnetic resonance imaging of the distribution of the single substitutional nitrogen impurity through polycrystalline diamond samples grown by chemical vapor deposition. **Journal of Applied Physics**, v. 82, n. 3, p. 1201–1204, 1997.

4 MAZE, J. R. et al. Properties of nitrogen-vacancy centers in diamond: the group theoretic approach. **New Journal of Physics**, v. 13, n. 2, p. 025025, 2011.

5 ACOSTA, V. M. et al. Optical properties of the nitrogen-vacancy singlet levels in diamond. **Physical Review B**, v. 82, n. 20, p. 201202, 2010.

6 JELEZKO, F.; WRACHTRUP, J. Single defect centres in diamond: a review. **Physica Status Solidi A**, v. 203, n. 13, p. 3207–3225.

7 WRACHTRUP, J.; JELEZKO, F. Processing quantum information in diamond. **Journal of Physics**, v. 18, n. 21, p. S807, 2006.

8 GAEBEL, T. et al. Room-temperature coherent coupling of single spins in diamond. **Nature Physics**, v. 2, n. 408, 2016. doi: 10.1038/nphys318.

9 SHI, F. et al. Quantum logic readout and cooling of a single dark electron spin. **Physical Review B**, v. 87, n. 19, p. 195414, 2013. doi: 10.1103/PhysRevB.87.195414.

10 BERNIEN, H. et al. Heralded entanglement between solid-state qubits separated by three metres. **Nature**, v. 497, n. 86, 2013. doi: 10.1038/nature12016.

11 JELEZKO, F. et al. Observation of coherent oscillation of a single nuclear spin and realization of a two-qubit conditional quantum gate. **Physical Review Letters**, v. 93, n. 13, p. 130501, 2004. doi: 10.1103/PhysRevLett.93.130501.

12 STEINERT, S. et al. High sensitivity magnetic imaging using an array of spins in diamond. **Review of Scientific Instruments**, v. 81, n. 4, p. 043705, 2010.

13 SIMPSON, D. A. et al. Magneto-optical imaging of thin magnetic films using spins in diamond. **Scientific Reports**, v. 6, n. 22797, 2016.

14 MACLAURIN, D. et al. Nanoscale magnetometry through quantum control of nitrogen–vacancy centres in rotationally diffusing nanodiamonds. **New Journal of Physics**, v. 15, n. 1, p. 013041, 2013.

15 TETIENNE, J.-P. et al. Quantum imaging of current flow in graphene. **Science Advances**, v. 3, n. 4, 2017.

16 MAZE, J. R. et al. Nanoscale magnetic sensing with an individual electronic spin in diamond. **Nature**, v. 455, n. 644, 2008. doi: 10.1038/nature07279.

17 HAUSMANN, B. J. et al. Fabrication of diamond nanowires for quantum information processing applications. **Diamond and Related Materials**, v. 19, n. 5, p. 621 – 629, 2010. doi: 10.1016/j.diamond.2010.01.011.

18 HAUSMANN, B. J. M. et al. Integrated high-quality factor optical resonators in diamond. **Nano Letters**, v. 13, n. 1898, 2013. doi: 10.1021/nl3037454.

19 FARAON, A. et al. Quantum photonic devices in single-crystal diamond. **New Journal of Physics**, v. 15, n. 2, p. 025010, 2013. doi: 10.1088/1367-2630/15/2/025010.

20 HAUSMANN, B. J. M. et al. Diamond nonlinear photonics. **Nature Photonics**, v. 8, 2014. doi: 10.1038/nphoton.2014.72.

21 LIU, Y. et al. Fabrication of nitrogen vacancy color centers by femtosecond pulse laser illumination. **Optics Express**, v. 21, n. 10, p. 12843–12848, 2013.

22 ALMEIDA, J. M. P. et al. Nonlinear optical spectrum of diamond at femtosecond regime. **Scientific Reports**, v. 7, n. 14320, 2017.

23 GALI, A.; FYTA, M.; KAXIRAS, E. Ab initio supercell calculations on nitrogen-vacancy center in diamond: Electronic structure and hyperfine tensors. **Physical Review B**, v. 77, n. 15, p. 155206, 2008.

24 GALI, A. et al. Theory of spin-conserving excitation of the nv center in diamond. **Physical Review Letters**, v. 103, n. 18, p. 186404, 2009.

25 DELANEY, P.; GREER, J. C.; LARSSON, J. A. Spin-polarization mechanisms of the nitrogen-vacancy center in diamond. **Nano Letters**, v. 10, n. 2, p. 610–614, 2010.

26 HOSSAIN, F. M. et al. Ab initio electronic and optical properties of the nv center in diamond. **Physical Review Letters**, v. 101, n. 22, p. 226403, 2008.

27 LOUBSER, J. H. N.; WYK, J. A. van. Electron spin resonance in the study of diamond. **Reports on Progress in Physics**, v. 41, n. 8, p. 1201, 1978.

28 DAVIES, G.; HAMER, M. F.; PRICE, W. C. Optical studies of the 1.945 ev vibronic band in diamond. **Proceedings of the Royal Society of London A**, v. 348, n. 1653, p. 285–298, 1976. doi: 10.1098/rspa.1976.0039.

29 MANSON, N. B.; HARRISON, J. P.; SELLARS, M. J. Nitrogen-vacancy center in diamond: Model of the electronic structure and associated dynamics. **Physical Review B**, v. 74, n. 10, p. 104303, 2006.

30 DOHERTY, M. W. et al. The nitrogen-vacancy colour centre in diamond. **Physics Reports**, v. 528, n. 1, p. 1 – 45, 2013.

31 ACOSTA, V. M. **Optical magnetometry with nitrogen-vacancy centers in diamond**. 2011. 118 p. Ph.D. Thesis. (Science) — University of California, Berkeley, California, 2011.

32 BALASUBRAMANIAN, G. et al. Nitrogen-vacancy color center in diamond—emerging nanoscale applications in bioimaging and biosensing. **Current Opinion in Chemical Biology**, v. 20, n. 1, p. 69 – 77, 2014.

33 GEISELMANN, M. **All optical manipulation of a single nitrogen vacancy center in nanodiamond**. 2014. 123 p. Ph.D. Thesis. (Science) — Universitat Politécnica DE Catalunya, Barcelona, 2014.

34 KEHAYIAS, P. et al. Infrared absorption band and vibronic structure of the nitrogen-vacancy center in diamond. **Physical Review B**, v. 88, n. 16, p. 165202, 2013.

35 ROGERS, L. J. et al. Infrared emission of the nv centre in diamond: Zeeman and uniaxial stress studies. **New Journal of Physics**, v. 10, n. 10, p. 103024, 2008.

36 MA, Y.; ROHLFING, M.; GALI, A. Excited states of the negatively charged nitrogen-vacancy color center in diamond. **Physical Review B**, v. 81, n. 4, p. 041204, 2010. doi: 10.1103/PhysRevB.81.041204.

37 ACOSTA, V. M. et al. Broadband magnetometry by infrared-absorption detection of nitrogen-vacancy ensembles in diamond. **Applied Physics Letters**, v. 97, n. 17, p. 174104, 2010.

38 ROBLEDO, L. et al. Spin dynamics in the optical cycle of single nitrogen-vacancy centres in diamond. **New Journal of Physics**, v. 13, n. 2, p. 025013, 2011.

39 FELTON, S. et al. Hyperfine interaction in the ground state of the negatively charged nitrogen vacancy center in diamond. **Physical Review B**, v. 79, n. 7, p. 075203, 2009.

40 SLICHTER, C. **Principles of Magnetic Resonance**. Berlin: Springer, 1996. (Springer).

41 ABRAGAM, P.; ABRAGAM, A. **The Principles of Nuclear Magnetism**. Oxford: Clarendon Press, 1961. (Comparative Pathobiology - Studies in the Postmodern Theory of Education).

42 SCHWEIGER, A.; JESCHKE, G. **Principles of Pulse Electron Paramagnetic Resonance**. Oxford: Oxford University Press, 2001.

43 JUNK, M. J. N. **Assessing the Functional Structure of Molecular Transporters by EPR Spectroscopy**. Berlin, Heidelberg: Springer Berlin Heidelberg, 2012. 7–52 p.

44 RABEAU, J. R. et al. Implantation of labelled single nitrogen vacancy centers in diamond using n15. **Applied Physics Letters**, v. 88, n. 2, p. 023113, 2006.

45 RONDIN, L. et al. Magnetometry with nitrogen-vacancy defects in diamond. **Reports on Progress in Physics**, v. 77, n. 5, p. 056503, 2014.

46 ACOSTA, V.; HEMMER, P. Nitrogen-vacancy centers: physics and applications. **MRS Bulletin**, v. 38, n. 2, p. 127–130, 2013. doi: 10.1557/mrs.2013.18.

47 HOROWITZ, V. R. et al. Electron spin resonance of nitrogen-vacancy centers in optically trapped nanodiamonds. **Proceedings of the National Academy of Sciences**, v. 109, n. 34, p. 13493–13497, 2012. doi: 10.1073/pnas.1211311109.

48 AMAN, H.; PLAKHOTNIK, T. Accuracy in the measurement of magnetic fields using nitrogen-vacancy centers in nanodiamonds. **Journal of the Optical Society of America B**, v. 33, n. 3, p. B19–B27, 2016. doi: 10.1364/JOSAB.33.000B19.

49 HONG, S. et al. Nanoscale magnetometry with nv centers in diamond. **MRS Bulletin**, v. 38, n. 2, p. 155–161, 2013.

50 APPEL, P. et al. Fabrication of all diamond scanning probes for nanoscale magnetometry. **Review of Scientific Instruments**, v. 87, n. 6, p. 063703, 2016.

51 NOWODZINSKI, A. et al. Nitrogen-vacancy centers in diamond for current imaging at the redistributive layer level of integrated circuits. **Microelectronics Reliability**, v. 55, n. 9, p. 1549 – 1553, 2015.

52 DAVIS, H. C. et al. Mapping the microscale origins of magnetic resonance image contrast with subcellular diamond magnetometry. **Nature Communications**, v. 9, n. 131, 2018.

53 ACOSTA, V. M. et al. Temperature dependence of the nitrogen-vacancy magnetic resonance in diamond. **Physical Review Letters**, v. 104, n. 7, p. 070801, 2010.

54 CHEN, X.-D. et al. Temperature dependent energy level shifts of nitrogen-vacancy centers in diamond. **Applied Physics Letters**, v. 99, n. 16, p. 161903, 2011.

55 TETIENNE, J.-P. et al. Magnetic-field-dependent photodynamics of single nv defects in diamond: an application to qualitative all-optical magnetic imaging. **New Journal of Physics**, v. 14, n. 10, p. 103033, 2012.

56 PHAM, L. M. **Magnetic Field Sensing with Nitrogen-Vacancy Color Centers in Diamond**. 2013. 136 p. Ph.D. Thesis. (Science) — Harvard University, Cambridge, Massachusetts, 2013.

57 BUDKER, D.; ROMALIS, M. Optical magnetometry. **Nature Physics**, v. 3, p. 227–234, 2007. doi: 10.1038/nphys566.

58 TAYLOR, J. M. et al. High-sensitivity diamond magnetometer with nanoscale resolution. **Nature Physics**, v. 4, p. 810–816, 2008. doi: 10.1038/nphys1075.

59 DRÉAU, A. et al. Avoiding power broadening in optically detected magnetic resonance of single nv defects for enhanced dc magnetic field sensitivity. **Physical Review B**, v. 84, n. 19, p. 195204, 2011.

60 LESIK, M. **Engineering of NV color centers in diamond for their applications in quantum information and magnetometry**. 2015. Ph.D. Thesis. (Science) — École normale supérieure de Cachan - ENS Cachan, 2015.

61 HAQUE, A.; SUMAIAYA, S. An overview on the formation and processing of nitrogen-vacancy photonic centers in diamond by ion implantation. **Journal of Manufacturing and Material Processing**, v. 1, n. 1, p. 6, 2017.

62 PEZZAGNA, S. et al. An overview on the formation and processing of nitrogen-vacancy photonic centers in diamond by ion implantation. **New Journal of Physics**, v. 12, n. 6, p. 065017, 2010.

63 CHIPAUX, M. et al. Magnetic imaging with an ensemble of nitrogen-vacancy centers in diamond. **European Physical Journal D**, v. 69, n. 7, p. 166, 2015.

64 JENSEN, K. et al. Light narrowing of magnetic resonances in ensembles of nitrogen-vacancy centers in diamond. **Physical Review B**, v. 87, n. 1, p. 014115, 2013.

65 APPELT, S. et al. Light narrowing of rubidium magnetic-resonance lines in high-pressure optical-pumping cells. **Physical Review A**, v. 59, n. 3, p. 2078–2084, 1999.

66 BHASKAR, N. D. et al. Light narrowing of magnetic resonance lines in dense, optically pumped alkali-metal vapor. **Physical Review A**, v. 23, n. 6, p. 3048–3064, 1981.

67 MORÉ, J. J. The levenberg-marquardt algorithm: Implementation and theory. In: WATSON, G. A. (Ed.). **Numerical analysis**. Berlin: Springer, 1978. p. 105–116.

68 TETIENNE, J.-P. et al. Apparent delocalization of the current density in metallic wires observed with diamond nitrogen-vacancy magnetometry. **Physical Review B**, v. 99, n. 1, p. 014436, 2019. doi: 10.1103/PhysRevB.99.014436.

69 ROTH, B. J.; SEPULVEDA, N. G.; WIKSWO, J. P. Using a magnetometer to image a two-dimensional current distribution. **Journal of Applied Physics**, v. 65, n. 1, p. 361–372, 1989.

70 GULKA, M. et al. Pulsed photoelectric coherent manipulation and detection of n-v center spins in diamond. **Physical Review Applied**, v. 7, n. 4, p. 044032, 2017.

71 HALL, L. T. et al. Sensing of fluctuating nanoscale magnetic fields using nitrogen-vacancy centers in diamond. **Physical Review Letters**, v. 103, n. 22, p. 220802, 2009.

72 RAMSEY, N. F. A molecular beam resonance method with separated oscillating fields. **Physical Review**, v. 78, n. 6, p. 695–699, 1950.

73 WOOD, A. A. et al. T_2-limited sensing of static magnetic fields via fast rotation of quantum spins. **Physical Review B**, v. 98, n. 17, p. 174114, 2018.

74 ASTASHKIN, A. V.; RAITSIMRING, A. M. Electron spin echo envelope modulation theory for high electron spin systems in weak crystal field. **Journal of Chemical Physics**, v. 117, n. 13, p. 6121–6132, 2002.

75 MIMS, W. B. Amplitudes of superhyperfine frequencies displayed in the electron-spin-echo envelope. **Physical Review B**, v. 6, n. 9, p. 3543–3545, 1972.

76 OHNO, K. et al. Engineering shallow spins in diamond with nitrogen delta-doping. **Applied Physics Letters**, v. 101, n. 8, p. 082413, 2012.

77 ROWAN, L. G.; HAHN, E. L.; MIMS, W. B. Electron-spin-echo envelope modulation. **Physical Review**, v. 137, n. 1A, p. A61–A71, 1965.

78 ELTON, D. C. Stretched exponential relaxation. 2018. Available from: https:<//arxiv.org/pdf/1808.00881.pdf>. Accessible at: 30 Oct. 2018.

79 JENSEN, K.; KEHAYIAS, P.; BUDKER, D. Magnetometry with nitrogen-vacancy centers in diamond. In: GROSZ, A.; HAJI-SHEIKH, M. J.; MUKHOPADHYAY, S. C. (Ed.). **High Sensitivity Magnetometers**. Switzerland: Springer, 2017. p. 553–576. (Smart sensors, measurement and instrumentation, v.19).

80 MAURER, P. C. et al. Far-field optical imaging and manipulation of individual spins with nanoscale resolution. **Nature Physics**, v. 6, p. 912–918, 2010. doi: 10.1038/nphys1774.

81 JAMIESON, D. N. et al. Controlled shallow single-ion implantation in silicon using an active substrate for sub-20-kev ions. **Applied Physics Letters**, v. 86, n. 20, p. 202101, 2005. doi: 10.1063/1.1925320.

82 SCHWARTZ, J. et al. Local formation of nitrogen-vacancy centers in diamond by swift heavy ions. **Journal of Applied Physics**, v. 116, n. 21, p. 214107, 2014.

83 ORWA, J. O. et al. Engineering of nitrogen-vacancy color centers in high purity diamond by ion implantation and annealing. **Journal of Applied Physics**, v. 109, n. 8, p. 083530, 2011.

84 SCHWARTZ, J. et al. Effects of low-energy electron irradiation on formation of nitrogen–vacancy centers in single-crystal diamond. **New Journal of Physics**, v. 14, n. 4, p. 043024, 2012.

85 PIMENOV, S. M. et al. Picosecond-laser bulk modification induced enhancement of nitrogen-vacancy luminescence in diamond. **Journal of the Optical Society of America B**, v. 33, n. 3, p. B49–B55, 2016.

86 CHEN, Y.-C. et al. Laser writing of coherent colour centres in diamond. **Nature Photonics**, v. 11, p. 77–80, 2016. doi: 10.1038/srep46722.

87 KONONENKO, V. V. et al. Nitrogen-vacancy defects in diamond produced by femtosecond laser nanoablation technique. **Applied Physics Letters**, v. 111, n. 8, p. 081101, 2017.

88 PIMENOV, S. M. et al. Picosecond-laser-induced structural modifications in the bulk of single-crystal diamond. **Applied Physics A**, v. 105, n. 3, p. 673–677, 2011.

89 ALMEIDA, J. M. P. **Nanoparticles in oxide and chalcogenide glasses: optical nonlinearities and waveguide fabrication by femtosecond laser pulses**. 2015. 113 p. Ph.D. Thesis. (Science) — Escola de Engenharia de São Carlos, Universidade de São Paulo, São Carlos, 2015.

90 CHAN, J. et al. Modification of the fused silica glass network associated with waveguide fabrication using femtosecond laser pulses. **Applied Physics A**, v. 76, n. 3, p. 367–372, 2003.

91 CHAN, J. W. et al. Waveguide fabrication in phosphate glasses using femtosecond laser pulses. **Applied Physics Letters**, v. 82, n. 15, p. 2371–2373, 2003.

92 LIU, J. M. Simple technique for measurements of pulsed gaussian-beam spot sizes. **Optics Letters**, v. 7, n. 5, p. 196–198, 1982.

93 GATTASS, R. R.; MAZUR, E. Femtosecond laser micromachining in transparent materials. **Nature Photonics**, v. 2, p. 219 – 225, 2008.

94 SCHAFFER, C.; GARCÍA, J.; MAZUR, E. Bulk heating of transparent materials using a high-repetition-rate femtosecond laser. **Applied Physics A**, v. 76, n. 3, p. 351–354, 2003.

95 IAKOUBOVSKII, K.; ADRIAENSSENS, G. Optical detection of defect centers in cvd diamond. **Diamond and Related Materials**, v. 9, n. 7, p. 1349 – 1356, 2000.

96 VLASOV, I. I. et al. Bulk and surface-enhanced raman spectroscopy of nitrogen-doped ultrananocrystalline diamond films. **Physica Status Solidi A**, v. 203, n. 12, p. 3028–3035, 2006.

97 WANG, P.-N. et al. Raman spectroscopy on the $\beta - c_3n_4$ structure formed by low-energy nitrogen ion implantation into a diamond surface. **Physical Review B**, v. 59, n. 20, p. 13347–13349, 1999.

98 AHARONOVICH, I.; GREENTREE, A. D.; PRAWER, S. Diamond photonics. **Nature Photonics**, v. 5, n. 7, p. 397–405, 2011. doi: 10.1038/nphoton.2011.54.

99 SIPAHIGIL, A. et al. An integrated diamond nanophotonics platform for quantum-optical networks. **Science**, v. 354, n. 6314, p. 847–850, 2016.

100 ABE, N. et al. Dynamically unpolarized single-photon source in diamond with intrinsic randomness. **Scientific Reports**, v. 7, n. 46722, 2017.

101 PALYANOV, Y. N. et al. Germanium: a new catalyst for diamond synthesis and a new optically active impurity in diamond. **Scientific Reports**, v. 5, n. 14789, 2015.

102 GRANADOS, E.; SPENCE, D. J.; MILDREN, R. P. Deep ultraviolet diamond raman laser. **Optics Express**, v. 19, n. 11, p. 10857–10863, 2011.

103 MURTAGH, M. et al. Efficient diamond raman laser generating 65 fs pulses. **Optics Express**, v. 23, n. 12, p. 15504–15513, 2015.

104 CHEN, Y.-C. et al. Laser writing of coherent colour centres in diamond. **Nature Photonics**, v. 11, p. 77–80, 2016.

105 SOTILLO, B. et al. Diamond photonics platform enabled by femtosecond laser writing. **Scientific Reports**, v. 6, 2016. doi: 10.1038/srep35566.

106 BAHAE, M. S. et al. Optical nonlinearities in diamond. **Proceedings of SPIE**, v. 2428, p. 2428 – 2433, 1995.

107 KOZÁK, M. et al. Two- and three-photon absorption in chemical vapor deposition diamond. **Journal of the Optical Society of America B Optical Physics**, v. 29, p. 1141, 2012.

108 ZHAO, J. et al. Measurement of third-order nonlinear optical susceptibility of synthetic diamonds. **Chinese Optics Letters**, v. 8, n. 7, p. 685–688, 2010.

109 LEVENSON, M. D.; FLYTZANIS, C.; BLOEMBERGEN, N. Interference of resonant and nonresonant three-wave mixing in diamond. **Physical Review B**, v. 6, n. 10, p. 3962–3965, 1972.

110 LEVENSON, M. D.; BLOEMBERGEN, N. Dispersion of the nonlinear optical susceptibility tensor in centrosymmetric media. **Physical Review B**, v. 10, n. 10, p. 4447–4463, 1974.

111 GARCIA, H.; KALYANARAMAN, R. Phonon-assisted two-photon absorption in the presence of a dc-field: the nonlinear franz–keldysh effect in indirect gap semiconductors. **Journal of Physics B: Atomic, Molecular and Optical Physics**, v. 39, n. 12, p. 2737–2746, 2006.

112 DINU, M. Dispersion of phonon-assisted nonresonant third-order nonlinearities. **IEEE Journal of Quantum Electronics**, v. 39, n. 11, p. 1498–1503, 2003.

113 HON, N. K.; SOREF, R.; JALALI, B. The third-order nonlinear optical coefficients of si, ge, and si_{1-x} ge_x in the midwave and longwave infrared. **Journal of Applied Physics**, v. 110, n. 1, p. 011301, 2011.

114 BAHAE, M. S. et al. Dispersion of bound electron nonlinear refraction in solids. **IEEE Journal of Quantum Electronics**, v. 27, n. 6, p. 1296–1309, 1991.

115 BAHAE, M. S.; SAID, A. A.; HAGAN, D. J. Nonlinear refraction and optical limiting in thick media. **Optical Engineering**, v. 30, n. 8, p. 1228 – 1991, 1991.

116 GAGARSKII, S.; PRIKHOD'KO, K. Measuring the parameters of femtosecond pulses in a wide spectral range on the basis of the multiphoton-absorption effect in a natural diamond crystal. **Journal Optical Technology**, v. 75, n. 3, p. 139–143, 2008.

117 PREUSS, S.; STUKE, M. Subpicosecond ultraviolet laser ablation of diamond: Nonlinear properties at 248 nm and time-resolved characterization of ablation dynamics. **Applied Physics Letters**, v. 67, n. 3, p. 338–340, 1995.

118 DADAP, J. I. et al. Two-photon absorption in diamond and its application to ultraviolet femtosecond pulse-width measurement. **Optics Letters**, v. 16, n. 7, p. 499–501, 1991.

Appendix

APPENDIX A – ELECTRON SPIN ECHO ENVELOPE MODULATION (ESEEM)

The principles of many pulse EPR experiments can be explained by considering a system consisting of one electron spin $S = 1/2$ coupled to one nuclear spin $I = 1/2$ in a constant magnetic field B_0, resulting in an interaction given by

$$H_0 = \omega_E \, S_z + \omega_N \, I_z + \vec{S}.\overline{A}.\vec{I} \tag{A.1}$$

where ω_E e ω_N are the Larmor frequency of the electron and nuclei respectively.

Due to the axial symmetry of the NV center, the principal coordinate systems of the hyperfine interaction tensor is given in the diagonal form

$$\overline{A} = \begin{bmatrix} A_{xx} & 0 & 0 \\ 0 & A_{yy} & 0 \\ 0 & 0 & A_{zz} \end{bmatrix} \tag{A.2}$$

Thus the Hamiltonian can be written as

$$H_0 = \omega_E \, S_z + \omega_N \, I_z + A_{xx} S_x I_x + A_{yy} S_y I_y + A_{zz} S_z I_z \tag{A.3}$$

Transforming the Hamiltonian with the operator $e^{-i\eta I_z}$, where $\eta = \arctan\left(A_{xx}/A_{yy}\right)$, it can be written as

$$H_0 = \omega_E \, S_z + \omega_N \, I_z + B S_z I_x + A S_z I_z \tag{A.4}$$

where $A = A_{zz}$ and $B = \sqrt{A_{xx}^2 + A_{yy}^2}$. Since H_0 is diagonal with respect to S_z, we may write the Hamiltonian as

$$H_0 = \; m_S \, \omega_E + \left(m_S \, A - \omega_N\right) I_z + m_S \, B \, I_x, \tag{A.5}$$

with $m_S = \pm 1/2$.

Performing an unitary rotation about the I_y axis, $R(\phi) = e^{-i \, \phi \, I_y}$, we obtain

$$H = e^{i \, \phi \, I_y} \, H_0 \, e^{-i \, \phi \, I_y}$$

$$H = m_S \, \omega_E + K \, I_z \tag{A.6}$$

where

$$K = \left(\left(m_S \, A - \omega_N\right)^2 + B^2 \, m_S^2\right)^{1/2},$$

and

$$\tan\left(\phi\right) = \frac{B \, m_S}{m_S \, A - \omega_N}.$$

The eigenvalues of H are

$$E_{m_I}(m_S) = \omega_E\, m_S + K\, m_I \tag{A.7}$$

and the eigenvectors are

$$|E_+(+)\rangle = \cos\frac{\phi^+}{2}\,|++\rangle + \mathrm{sen}\frac{\phi^+}{2}\,|+-\rangle$$

$$|E_-(+)\rangle = \cos\frac{\phi^+}{2}\,|+-\rangle - \mathrm{sen}\frac{\phi^+}{2}\,|++\rangle$$

$$|E_+(-)\rangle = \cos\frac{\phi^-}{2}\,|-+\rangle + \mathrm{sen}\frac{\phi^-}{2}\,|--\rangle$$

$$|E_-(-)\rangle = \cos\frac{\phi^-}{2}\,|--\rangle - \mathrm{sen}\frac{\phi^-}{2}\,|-+\rangle$$

where the eigenstates are denoted by $|E_{m_I}(m_S)\rangle$ and $+$, $-$ correspond to m_I, m_S values of $+1/2$ and $-1/2$.

The explicit expressions for the spin echo envelope are conveniently obtained from the density matrix formalism.

$$\frac{d\rho}{dt} = i\,[\rho, H_0] \tag{A.8}$$

To obtain the echo signal, the equation (A.8) must be integrated to give the final density matrix $\rho(t_f)$, corresponding to the time of appearance of the echo, in terms of the initial density $\rho(0) = \rho_0$. If the Hamiltonian ($H = H_0$) is time-independent, we can solve the equation (A.8)

$$\rho(t) = e^{-iH_0t}\rho(0)e^{iH_0t} = U(t)\rho_0U^\dagger(t) \tag{A.9}$$

The quantity $U(t) = e^{-iH_0t}$ is called the propagator. The evolution of the system during the pulses with any RF (or MW) field turned on is associated with the Hamiltonian

$$H_1(t) = 2\vec{\mu}.\vec{B_1}(t) = 2\,\omega_1 S_x \cos(\Omega t) \tag{A.10}$$

The analysis of the effect of RF pulses is best conducted by using the concept of the rotating frame. The transformation of the density operator from the laboratory to the rotating frame (which rotates around the z-axis with frequency Ω) is

$$\rho^{rot} = e^{-i\Omega t S_z}\,\rho^{lab}\,e^{i\Omega t S_z} \tag{A.11}$$

A simplification by a transformation to the electron rotating frame, so

$$H_r = H_0 - \Omega\, S_z, \tag{A.12}$$

which eliminates the electron Larmor frequency term in H_0 given by the equation (A.4). The effect of a RF pulse can be obtained by transforming the complete Hamiltonian $H(t) = H_0 + H_1(t)$ from the laboratory to the rotating frame

$$H_{eff} = H_0 - \Omega\, S_z + \omega_1\, S_x \tag{A.13}$$

This describes a RF pulse applied along the x-direction of the rotating-frame, the transformation has removed the time dependence from the RF Hamiltonian. If $\Omega \simeq \omega_E$; $\omega_1 \gg \omega_N, A, B$; and $\omega_E \gg \omega_N, A, B$, then the effective Hamiltonian is approximated by

$$H_{eff} \simeq \omega_1 S_x, \tag{A.14}$$

Considering thus a strong RF pulse with duration t_p applied along the x-direction, the evolution operator in this case is given by

$$U = e^{iH_{eff}t_p} = e^{i\omega_1 t_p S_x}. \tag{A.15}$$

If we define the rotation operator $R_x(\theta_p) = e^{i\theta_p S_x}$, which produces a nutation of an angle $\theta_p = \omega_1 t_p$ around the x-axis (according to the right-hand rule) of the rotating frame, so the density operator is therefore

$$\rho(t_p) = R_x(\theta_p)\, \rho_0\, R_x^{\dagger}(\theta_p). \tag{A.16}$$

Depending upon whether the microwave pulses are off or on, respectively, during a given time segment, we can write the final density matrix after two or three pulses as

$$\rho(t) = R_{seq}\, \rho_0\, R_{seq}^{\dagger}, \tag{A.17}$$

where

$$R_{2p} = e^{i\, S_x\, \pi/2}\, e^{i\, H_r\, \tau}\, e^{i\, S_x\, \pi}\, e^{i\, H_r\, \tau} \tag{A.18}$$

$$R_{3p} = e^{i\, S_x\, \pi/2}\, e^{i\, H_r\, \tau}\, e^{i\, S_x\, \pi/2}\, e^{i\, H_r\, T}\, e^{i\, S_x\, \pi/2}\, e^{i\, H_r\, \tau} \tag{A.19}$$

The observed electron echo signal is given by

$$V = \frac{\mathrm{Tr}\,(\rho_{seq}\, S_y)}{\mathrm{Tr}\,(\rho_0\, S_y)}. \tag{A.20}$$

Therefore, the echo signal at $t = 2\tau$ and $t = 2\tau + T$ for two and three pulses

$$V_{2p}(\tau) = 1 - 2\, k\, \mathrm{sen}^2\left(\frac{K^+\tau}{2}\right)\, \mathrm{sen}^2\left(\frac{K^-\tau}{2}\right) \tag{A.21}$$

$$V_{3p}(\tau, T) = 1 - k\left[\mathrm{sen}^2(K^+\tau/2)\,\mathrm{sen}^2(K^-(\tau+T)/2) + \mathrm{sen}^2(K^-\tau/2)\,\mathrm{sen}^2(K^+(\tau+T)/2)\right] \tag{A.22}$$

with

$$k = \left[\frac{\omega_N\, B}{K^+\, K^-}\right]^2 \tag{A.23}$$

and K^+, K^- are the frequency of the nuclear transitions.